Polymer-Grafted and Agarose-Encapsulated Adsorbents for Protein and Bioparticle Purification

A dissertation presented to the faculty of the

School of Engineering and Applied Science

University of Virginia

In partial fulfillment of the requirements for

the degree of Doctor of Philosophy of Chemical Engineering

by

Preston Fuks

December 2021

APPROVAL SHEET

This

Dissertation

is submitted in partial fulfillment of the requirements
for the degree of

Doctor of Philosophy

Author: Preston Fuks

This Dissertation has been read and approved by the examing committee:

Advisor: Giorgio Carta

Advisor:

Committee Member: Roseanne Ford

Committee Member: Rachel Letteri

Committee Member: Chris Highley

Committee Member: Stacey Criswell

Committee Member:

Committee Member:

Accepted for the School of Engineering and Applied Science:

Jennifer L. West, School of Engineering and Applied Science

December 2021

Abstract

Understanding the interplay between the stationary phase architecture and the mechanism of protein adsorption and transport is vital for the optimal design of chromatographic processes. This work studies the properties of stationary phases obtained by modifying a base matrix by grafting dextran polymers or by the incorporation in agarose gels.

Anion exchangers with low graft content (Nuvia HR Q and Nuvia HP Q) and high graft content (Nuvia Q) are considered. The accessible pore volume decreases with increasing polymer-graft content. Conversely, the binding capacity for bovine serum albumin (BSA) and thyroglobulin (Tg) increases with polymer-graft content. Dynamic binding capacities significantly increase at moderate NaCl concentrations for all polymer-grafted adsorbents. Breakthrough of mixtures of BSA and Tg demonstrates a higher selectivity for resins with intermediate graft density as well as a reversal in the order of breakthrough with the addition of NaCl. Pore diffusion best describes the adsorption kinetics of BSA and Tg on ungrafted resins while single file diffusion best describes two-component adsorption for highly grafted resins indicating that counter diffusion of displaced species hinders transport.

Novel composite-particles, obtained by encapsulating ceramic hydroxyapatite type-I particles (CHT), in inert agarose-beads were prepared via an emulsion method. The composite beads combine two chromatographic principles: separation by molecular size and separation by selective adsorption occurring within the encapsulated CHT particles. Adsorption capacities of BSA and RNA are lower on a bead volume basis relative to unencapsulated CHT; however, on a CHT volume basis, adsorption is similar to unencapsulated CHT suggesting that the agarose does not inhibit adsorption. Confocal laser scanning microscopy images show that large proteins such as Tg and IgM, and 30 nm and 50 nm nanoparticles are largely excluded from encapsulated CHT particles. Two-component breakthrough of mixtures containing 30 nm nanoparticles and either BSA or RNA demonstrate that the applicability of these novel materials to the flow-through purification of large proteins and bioparticles.

Acknowledgements

First and foremost, I would like to thank my advisor, Giorgio Carta. Without your guidance, willingness to help, and immense knowledge, this work would not have been possible.

I would also like to thank the members of my committee: Prof. Roseanne Ford, Prof. Rachel Letteri, Prof. Chris Highley, and Prof. Stacey Criswell for their valuable input.

I would also like to thank all the past, current, and visiting members of the Carta lab: Shaojie, Mimi, Jing, Arch, Jason, Yiran, Lucas, Joey, Patricia, Calef, and Xue. We have had valuable discussions and collaborations over my time here at UVa.

To my fellow friends in Charlottesville, thank you for making my time as enjoyable and wonderful as I could have hoped. Melissa, James, Rhea, and Max, thanks for putting up with me while we sheltered-in-place in our home. Thank you to Rabbi Shlomo Mayer and Rebbetzan Channa Mayer for making the UVa Chabad house my home away from home.

To Vickie, Teresa, Jennifer, Ricky, Ryan, Jen, and April thank you for your help with everything. Without all of you I would never have been able to graduate.

To all my previous teachers who taught me so much all along the way. With special thanks to Randy Appell, Christopher Bambino, and Prof. Justin Opatkiewicz for instilling in me a love of all things science.

Finally, I would like to thank my family, especially my father Leon, grandmar Sue, uncle Alan, and aunt Shevi for their love and continuous support. To my siblings, Tami, EJ, and Frances for always believing in me.

Dedicated to the loving memory of my mother Bonnye Fuks, aunt Deborah Kravits, and friend Monica Pirez Amhrein who are no longer with us.

Table of Contents

List of Figures

List of Tables

List of Acronyms and Symbols

Acronyms

AEX anion exchange

AgCHT agarose-encapsulated ceramic hydroxyapatite

BSA bovine serum albumin

BTP bis-tris propane

CEX cation exchange

CHT ceramic hydroxyapatite

CLSM confocal laser scanning microscopy

CV column volumes

DBC dynamic binding capacity

DEPC diethyl pyrocarbonate

DLS dynamic light scattering

EBC equilibrium binding capacity

EI empirical interpolation

FDA Food and Drug Administration

HAP hydroxyapatite

HETP height equivalent theoretical plate

HIC hydrophobic interaction chromatography

IEX ion exchange

iSEC inverse size exclusion chromatography

LGE linear gradient elution

PDI polydispersity index

SEC size exclusion chromatography

SMA steric mass action

TEM transmission electron microscopy

Tg thyroglobulin

VLP virus-like particle

WAPE weighted absolute percentage errors

Symbols

c protein concentration in the particle pores, mg/mL

C fluid phase concentration, mg/mL

C^* equilibrium fluid phase concentration, mg/mL

C_0 initial fluid phase, mg/mL

C_F feed protein concentration, mg/mL

$\overline{D}_s$ Maxwell-Stefan diffusivity, cm^2/s

D_0 free solution diffusivity, cm^2/s

D_e effective pore diffusivity in the pore diffusion model or linear driving force approximation, cm^2/s

D_L axial dispersion coefficient, cm^2/s

D_s adsorbed phase diffusivity in the solid diffusion model, cm^2/s

q adsorbed protein concentration, mg/mL

$\hat{q}$ protein concentration in the adsorbent particles including held in the pore liquid, mg/mL

q^* equilibrium adsorbed protein concentration, mg/mL

q_0 concentration of charged functional groups, mmol/mL

q_m binding capacity, mg/mL

CV_{sh} column volumes where a theoretical breakthrough would occur

d_p particle diameter, cm

h reduced HETP, = HETP/d_p

J mass transfer flux, mg/cm^2 s

K_c distribution coefficient

K_L Langmuir binding affinity constant, mL/mg

L column length, cm

M_r dextran probe molecular weight, Da

R gas constant, J/mol K

r_p particle radius, cm

$R_{pore,M}$ radius of the large pores in a bimodal pore distribution shown, nm

$R_{pore,m}$ radius of the small pores in a bimodal pore distribution, nm

RT residence time, = L/u, s

T absolute temperature, K

t time, s

t_{cycle} cycle time for a chromatographic separation, s

u superficial velocity, cm/s

V solution volume, L

v' reduced velocity, $= vd_p/D_0$

V_c column Volume

V_M volume of stationary phase, L

V_R volume of retention, mL

V_{CHT} volume of CHT beads, mL

x column axial coordinate, cm

z protein effective charge in the SMA model and Extended Langmuir model

Greek Symbols

χ mass fraction, g CHT/g particle

ϵ	extraparticle column void fraction
ϵ_p	intraparticle void fraction
$\epsilon_{p,M}$	intraparticle porosity of the small pores in a bimodal pore distribution
$\epsilon_{p,m}$	intraparticle porosity of the small pores in a bimodal pore distribution
Γ	thermodynamic Factor
ϕ	CHT content, mL CHT/mL particle
ρ	particle density, g/mL
σ	steric hindrance parameter in the SMA model
θ	surface coverage
ζ	discount factor
μ	chemical potential, J/mol

Chapter 1 Introduction

1.1 Motivation

Bioseparation processes are critical steps in the manufacturing of high purity proteins and other biotherapeutics. Following the introduction of the first U.S. Food and Drug Administration (FDA) approved monoclonal antibody (mAb) treatment in 1986 [1], mAbs have become the most successful biotherapeutics. Approvals of mAb-based therapeutics have seen rapid growth, accounting for 65% of all biologic sales, totaling $123 billion as of 2017 [2][3]. Despite mAb-based therapies holding a large market share, alternative therapies utilizing virus-like particles (VLPs) and nucleic acids are on the rise. Nucleic acid-based products include gene therapies, antisense oligonucleotides (ASOs), siRNAs, modified RNA molecules, as well as DNA and RNA vaccines.

Concerns about novel infectious diseases have increased dramatically in recent years [4]. Recent noteworthy novel infectious viruses in the past two decades include SARS (2002), H1N1 (swine flu, 2009), MERS (2012), Ebola (2014), Zika (2015), and of course, the one that has had the largest global impact, SARS-CoV-2 (Covid-19, 2019). Thus, biologics to combat these infectious diseases are critical as the frequency of global outbreaks increases [5]. The vaccine market is expected to grow to $67 billion in 2022 driven by global Covid-19 vaccine sales [6].

Increase in development and production of mAbs and VLPs has been propelled by advances in molecular biology over the last four decades. Cell culture titers increased from less than 0.5 g/L to more than 2.5 g/L for commercially manufactured mAb therapeutics [7][8]. Increasing cell culture efficiency is causing strain on downstream processes [9][10]. Chromatography plays a key role in the process-scale purification of therapeutic proteins [11][12] by leveraging differences in charge (ion exchange chromatography), size (size exclusion chromatography), and/or hydrophobicity (hydrophobic interaction chromatography) between the target product and impurities. Alternatively, they rely on a very specific interaction between a surface-bound ligand and the target molecule (affinity

chromatography). Purification of mAbs is dominated by an orthogonal "platform" approach containing a protein-A affinity-based capture step followed by one or more polishing steps utilizing a combination of cation exchange, anion exchange, and hydrophobic interaction chromatography [13]. Figure 1.1 illustrates the platform approach to the purification of mAbs and a general VLP purification scheme. This approach is made possible by the constant Fc domain which is conserved across many mAbs and which binds selectively to protein A resins [14]. Although Protein A capture often results in extremely high purity, additional purification steps are usually required to remove aggregates, undesirable variants, leached protein A, nucleic acids, adventitious viruses and other contaminants [15]. In contrast, VLP downstream processing does not have a platform approach because of the enormous diversity among VLPs.

Challenges arise during the purification of VLPs and viruses molecules due to their size, charge, and hydrophobicity [18][19]. VLPs and viruses are structurally diverse, generally ranging from 25 nm for Adeno-associated viruses to several hundred nanometers for herpesviruses [20]. The presence or absence of a viral envelope consisting of a lipid membrane containing glycoproteins further increases their diversity. The viral capsid can form many structures, most commonly, icosahedral structures and helical structures. However, other architectures exist that do not conform to either of these geometries [20]. Mammalian RNA and DNA are linear molecules comprised of nucleotides forming single strands (RNA) or double strands (DNA). Structural diversity stems from plasmid DNA predominantly found in bacteria in which double stranded DNA assumes a circular form. Additional complexity is due to the wide variability in sequence length of RNA and DNA. Sequence length can be as short as 18 base pairs for small non-coding RNA molecules and can exceed 100 kilobase pairs for plasmid DNA. Ultimately, the purification of viruses, VLPs, and nucleic acids require product and impurity considerations.

Improving the binding capacity, selectivity, adsorption kinetics, and mechanical strength of the

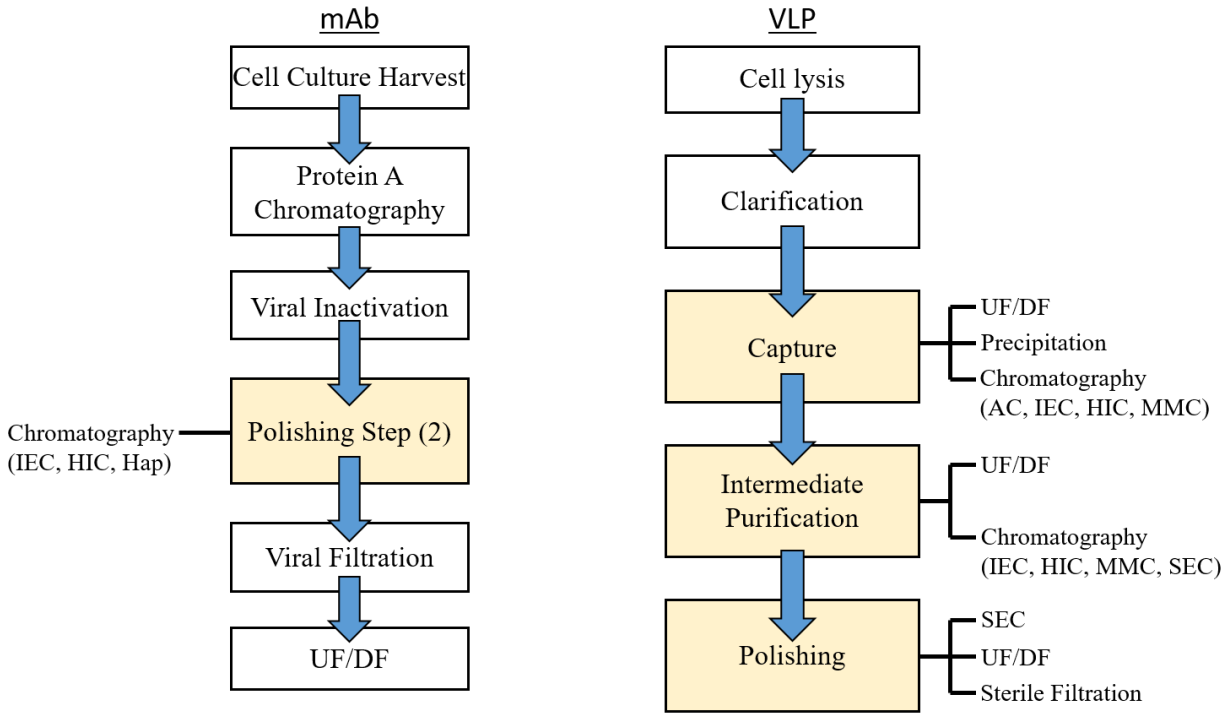

Figure 1.1: Monoclonal antibody purification platform adapted from [16](left) and an example of a VLP purification scheme adapted from [17] (right). Shaded steps indicate processes of interest in this work.

following stationary phases is essential to meet increasing industrial demands for more productive processes [11][21][22]. Traditional stationary phases contain ligands bound to the surface of an open-pore base matrix. Natural carbohydrate polymers, synthetic polymers, and/or inorganic materials are commonly used as the base matrix. Generally, carbohydrate polymer-based stationary phases such as agarose or dextran provide high binding capacity, are easy to functionalize, and exhibit limited non-specific interactions. However, the productivity of these materials is impeded by low mechanical stability and slow transport rates. In contrast, stationary phases based on synthetic polymers have a high rigidity and larger pore size resulting in high transport rates, but also in low surface areas and, consequently, low binding capacities. Inorganic-based stationary phases are less common than the aforementioned materials, are primarily constituted of silica, glass, and/or hydroxyapatite, and often require further chemical modification for practical applications [23].

Recently, several promising modifications to the functionalized macroporous matrices have been investigated. Polymers grafted to the open-pore architecture act as "surface extenders" and have been shown to increase the high binding capacity without compromising the mechanical strength of the base material [24]. An extreme modification to open-pore base architectures is the addition of a restricted-access matrix encapsulating conventional porous media; thus, adsorptive and size exclusion mechanisms are combined to form "lid" beads capable of preventing surface adsorption of large molecules [25].

Parallel to the development of more productive stationary phases are equally important developments in methods for modeling chromatographic separations. The ability to predict chromatographic behavior of proteins is an extremely desired skill in the pharmaceutical industry in order to guide process development and establish a robust set of operating conditions. Currently, the optimization of chromatographic separation is primarily based on experimental work. The FDA permits model-based approaches when designing downstream processing of biotherapeutics [26]. Therefore, integration

of mechanistic models into current and novel separation processes can increase overall efficiency and decrease the time to market.

1.2 Background

1.2.1 Polymer-grafted anion exchanges

Ion exchange chromatography (IEX) leverages differences in charge between target product and impurities in order to achieve separation. A common use of IEX is the separation of monomers from dimers and higher order aggregates since their differences in size and, consequently, charge result in different binding affinities [27]. Similarly, IEX can separate native proteins and unfolded proteins since shape and effective binding charge are linked [28]. IEX has demonstrated effectiveness in separating native proteins from charge variants [29] and from a variety of protein-conjugates [30][31]. Additional advantages of IEX adsorbents include their relatively low cost, are compatibility with a range of buffer conditions, the large number of commercially available stationary phases, and the ability to preserve biological activity of the product [28]. Consequently, IEX is among the most extensively utilized purification operations in biopharmaceutical manufacturing [32].

Polymer-grafted adsorbents are potentially advantageous for large scale protein purification [33][34]. Traditional, base matrices are comprised of macroporous spherical beads functionalized with ligands chemically linked to the support surface; therefore, proteins bind by surface interactions with the ligands within the pores. More recently, ion exchange resins have been developed with the ionic groups attached to linear polymer chains that are grafted onto the support surface. These polymer chains or "tentacles" provide increased access to the ligands thereby increasing the binding capacity [35]. The effects of tentacle length [36], tentacle density [37], and tentacle charge [38] have been investigated for some molecules, and have been found to influence both protein adsorption kinetics

and equilibrium binding capacity.

Investigations have demonstrated that both protein equilibrium binding capacity and mass transfer rates can be enhanced by including polymer-grafts. High binding capacity is attributed to multi-layer binding occurring throughout the three-dimensional network formed by the polymer-grafts [39]. Conversely, the mechanism responsible for enhanced mass transfer is attributed to solid phase or surface diffusion [40]. Transport within the graft-phase is driven by the adsorbed phase concentration gradient which, when the binding capacity is high, greatly exceeds the pore-phase concentration gradient [41]. In this case, the kinetic enhancement will depend on ionic strength, buffer pH, graft characteristics such as length and charge density, and protein characteristics [42].

The separation of very large biomolecules such as IgM (MW $\sim$ 950,000 Da), viruses, and virus-like particles, is challenging due to their small diffusivities in conventional chromatographic adsorbents based on macroporous beads. To achieve high dynamic binding capacities (DBC) and effective separations, low flow rates are necessary which, in turn, decreases productivity [43]. Approaches alternative to conventional beads where convective transport rather than diffusion is dominant have been proposed for the purification of large biomolecules including monoliths [44][45], perfusion chromatography [46], and adsorptive membranes [47]. However, these convection-enhanced adsorbents have limitations. For example monoliths are prone to fouling and clogging [48]; perfusion beads contain pore diameters insufficiently large for very large biomolecules to fully saturate the particles [46], and membrane adsorbers tend to have poor resolution resulting from poor flow properties as well as low binding capacity [49].

Ion exchange chromatography utilizing polymer-grafted adsorbents featuring high binding capacities and fast adsorption kinetics can overcome the difficulties in the purification of large biomolecules. Although many researchers have reported the effects of various polymer-graft characteristics on

increased binding capacity and enhanced transport, few authors have studied the effect on the adsorption of mixtures of proteins with large differences in size [50][51][52]. Moreover, the previous work in this area has dealt primarily with cation exchange (CEX) resins.

1.2.2 Agarose encapsulated adsorbents

Hydroxyapatite (HAP) is a inorganic crystalline material with the bulk formula $Ca_5(PO_4)_3OH$ that has found commercial success since first applied by Tiselius in 1956 to purify biomolecules [53]. HAP is nano-crystalline with dual-mode interaction properties. The crystal surface exhibits both negatively-charged phosphate groups referred to as P-sites and positively-charged calcium ions referred to as C-sites; thus, HAP is capable of binding with both basic and acidic proteins as well as nucleic acids [54]. Interactions of basic proteins with P-sites are modulated through non-binding salts, such as NaCl, that screen electrostatics. Conversely, interactions of acidic proteins and nucleic acids with C-sites are modulated by displacing salts, such as phosphate, that bind to the nanocrystal surface [55]. This dual-mode nature makes hydroxyapatite attractive for a wide range of separations [56]. For process applications, ceramic hydroxyapatite particles (CHT), produced by spray-drying hydroxyapatite nanocrystals followed by sintering at high temperature, are normally used. The CHT particles consist of a conglomerate of nanocrystals defining a rigid macroporous structure with pore radius in the 30-50 nm range. Typical particle sizes are in the 40-80 μm range. Similar to other chromatographic adsorbents, adsorbates diffuse in the macropores and bind to the nanocrystal surfaces.

Example of demonstrated process applications of CHT are the purification of anti-Japanese encephalitis virus monoclonal antibodies (mAbs) [57] the purification of VLPs [58], the purification of virus [59], and the isolation of plasmid DNA [60]. Despite the widespread use of CHT for biomolecule purification, studies providing a mechanistic description of protein adsorption equilibrium and

kinetics have only recently been published.

Wang et al. [61] has provided the most extensive study to date of protein adsorption equilibrium and kinetics focusing on the separation of mAb monomer-dimer mixtures. These authors concluded [61][62][63] that mAb monomer-dimer interactions with the HAP surface conform to a cation exchange mechanism. Although mAb monomer-dimer interactions were thoroughly investigated, similar investigations on the adsorption of acidic proteins on CHT remains incomplete.

Chromatographic purification in a flow-through mode, where impurities adsorb onto the column while the desired bio-particles pass through, is commonly practiced [64]. Although large bioparticles, because of their size, are typically excluded from the pores of most stationary phases binding on the outer surface of the chromatographic particles can still occur. While the external surface is small compared to the intraparticle surface, if the concentration of the bio-particle is small, even a small amount of surface binding can impair performance by reducing yield. Additionally, such bio-particle binding can occlude the underlying pores limiting or preventing impurities from accessing the particle interior. Thus, preventing surface binding is generally desirable for flow-through purification. Core-shell particles, where an inert shell surrounds an adsorbing core have been developed for this purpose. Currently, two such core-shell adsorbents are commercially available from Cytiva (Marlborough, MA, USA): Capto Core 700 and Capto Core 400. These resins consist of agarose-based beads whose core is functionalized with an octylamine ligand while leaving a thin inert layer at the bead outer surface [65]. Various studies have demonstrated the use of Capto Core 700 for the purification of viruses [66] and VLPs [67][68]. Due to the multimodal nature of the octylamine ligand, these resins possess significant salt tolerance and bind a variety of proteins over a wide range of salt concentrations [69][70]. However, the high binding affinity of the ligand typically requires harsh procedures to remove the bound species.

1.3 Research objectives

The objective of this work is to understand the chromatographic performance of recently developed and novel stationary phases. The first class of adsorbents examined here is based on a rigid macroporous hydrophilic matrix synthesized with hydrophilic monomers and then modified with charged polymer-grafts. Three anion exchangers with different degrees of polymer grafting and pore sizes are investigated. UNOSphere Diol Q, a macroporous adsorbent, serves as the control sample for three polymer-grafted resins. Nuvia Q has long polymeric grafts that occupy most of the pore volume. Nuvia HR Q and Nuvia HP Q have shorter polymer-grafts that leave much of the pore volume open. The base matrix of Nuvia HP Q has pores larger than that of Nuvia HR Q. Bovine serum albumin (BSA) and thyroglobulin (Tg) are used as model acidic proteins. They are negatively charged at physiological pH and bind to AEX resins. The principal aims of this work are to:

1. Characterize the physical properties of these resins.

2. Determine the effects of relative protein size and polymer-graft length on the adsorption equilibrium and kinetics.

3. Investigate how the effects examined in aim 2 translate to the column behavior of single and two-component mixtures of BSA and Tg.

4. Develop a mechanistic model to describe two-component protein adsorption in UNOSphere Diol Q and in Nuvia Q.

The second class of adsorbents examined here comprises CHT and novel composite beads obtained by encapsulating CHT particles in an inert agarose matrix. This encapsulation results in a composite material with two modes of separation: molecular size, resulting from the tunable agarose structure,

and adsorption occurring within the encapsulated CHT particles. The combination of size exclusion and adsorption mechanisms results in an adsorbent ideally suited for flow-through separations of large proteins and bio-particles such as virus, virus-like particles, and large vaccine molecules. Importantly, the agarose prevents surface binding of these bio-particles while permitting the binding of smaller impurities. The principal aims of this work can be divided into two parts. The first part involves understanding the equilibrium adsorption and kinetics of model protein impurities on the base CHT particles. The first set of aims are:

1. Investigate the effects of sodium chloride and sodium phosphate concentrations on the adsorption of acidic proteins.

2. Examine the competitive adsorption of acidic proteins on CHT and describe the results with a suitable multicomponent isotherm model.

3. Examine the effects of competitive adsorption of acidic proteins on multicomponent column behavior with a focus on frontal analysis-based separations and overloaded linear gradient elution-based separations.

The second part involves understanding the effect of preparation parameters, the physical characteristics, and the adsorption behavior of composite agarose-encapsulated CHT particles relative to unencapsulated CHT. The of aims of this part of the work are:

1. Develop and optimize an approach to prepare agarose-encapsulated CHT.

2. Understand how the emulsification conditions affect the resulting composite particles.

3. Characterize the physical structure of these composite beads with an emphasis on CHT content and pore size.

4. Quantify static and dynamic binding capacities to confirm that the AgCHT particles are suitable for the flow-through purification of large biomolecules.

Chapter 2 Polymer-grafted anion exchangers

2.1 Introduction

Polymeric extenders such as dextran grafted to adsorbent surfaces have the potential to enhance binding capacity and uptake kinetics compared to those of non-grafted macroporous adsorbents. Enhanced binding capacity and adsorption kinetics are vital to increase the performance of chromatographic adsorbents. However, these enhanced properties are coupled with increased complexity in transport relative to macroporous adsorbents.

A precursor to the polymer-grafted chromatographic adsorbents studied in this work are gel-in-a-shell adsorbents or particles in which nearly the whole pore space is occupied by a cross-linked gel structure [33]. Several authors investigated one class of such adsorbents known as HyperD. HyperD is comprised of a highly porous polystyrene-coated silica base-matrix whose pores are filled with a functionalized polyacrylamide gel. The polyacrylamide gel provides ion-exchange sites for protein adsorption while the rigid matrix provides structural strength. Fernandez et al. [71][72] investigated the equilibrium adsorption kinetics of BSA, ovalbumin, and α-lactulbumin on Q-HyperD, a quaternary ammonium ion functionalized version of HyperD. These authors observed a protein binding capacity on the order of 200 mg/mL. The uptake kinetics was quantified via batch kinetic measurements and shallow bed chromatography at various mobile phase velocities. The authors concluded that intraparticle mass transfer in these materials is controlled by a solid diffusion mechanism driven by the bound protein concentration gradient. Q-HyperD maintained high dynamic binding capacity even at elevated flow-rates. Weaver and Carta. [73] and Lewus et al. [74] investigated equilibrium adsorption and kinetics of lysozyme on S-HyperD, a CEX version of HyperD. The lysozyme binding capacity was found to be high at low ionic strengths and decreased with increasing ionic strength. These authors found that intraparticle mass transfer is also controlled by solid diffusion [73][74]. Weaver and Carta [73] observed that the lysozyme binding capacity

was 1.5 greater for S-HyperD than for POROS 50 HS, a macroporous adsorbent used as the control. Additionally, Lewus et al. [74] examined lysozyme desorption kinetics. These authors observed that lysozyme adsorption is reversible in this material over a range of 100 mM to 1000 mM NaCl with concentrations above 300 mM NaCl dominated being by intraparticle mass transfer [74].

A critical review of the work done on polymer-grafted chromatographic adsorbents follows. Several authors have investigated the adsorption of cationic proteins on cation exchange resins with and without polymer-grafts. Stone et al. [75], compared the adsorption capacity and adsorption kinetics of lysozyme on agarose beads grafted with either 10 kDa or 40 kDa dextran and functionalized with sulfopropyl groups with those of the corresponding ungrafted beads. They observed that while the adsorption capacity increased only slightly, the adsorption rates increased dramatically with grafting resulting in effective diffusivities that were 4-10 times larger than the protein solution diffusivity. Bowes and Lenhoff [76] characterized the adsorption capacity and adsorption kinetics of lysozyme and lactoferrin on dextran-grafted variants of the commercially available Capto S resin which is also based on cross-linked agarose beads. For lysozyme, an increase in charge density increased the binding capacity and slowed the kinetics. In contrast, for lactoferrin, which is much larger, an increased dextran content led to increased exclusion leading to lower capacity. These authors concluded that there exists a size-dependent trade-off between adsorption kinetics and equilibrium binding capacity for polymer-grafted resins. Yu et al. [39] synthesized dextran-modified agarose adsorbents with varying dextran content and constant ligand density and observed that the equilibrium binding capacity of γ-globulin increased with increasing dextran content. These authors attributed this increase to multi-layer binding.

Almodovar et al. [22] compared the adsorption of a mAb and of lysozyme on the CEX macroporous adsorbent UNOSphere S and on the polymer-grafted adsorbent Nuvia S, and observed a 2-3 fold increase in binding capacity for Nuvia S compared to UNOSphere S. Batch kinetic measurements

were used to quantify the adsorption kinetics in conjunction with confocal microscopy to observe the bound protein profiles within the resin particles during transient adsorption. These authors concluded that adsorption is faster in the polymer-grafted adsorbent with transport dominated by a solid diffusion mechanism. Almodovar et al. [77] also investigated the effects of solution counter-ions on equilibrium adsorption and kinetics including Ca^{2+}, arginine (Arg^{+}), Na^{+}, and tetra-n-butylammonium hydroxide ($TBAH^{+}$). The authors found that the counter-ion affected the protein binding affinity as well as the adsorption kinetics with faster rates obtained with counter-ions that had greater affinity for the resin. Conversely, the counter-ions had no impact on adsorption kinetics for the non-grafted adsorbent. The enhanced kinetics appeared to be a result of weakened protein binding to the polymer-grafts. Together these results suggest that the driving force for diffusional transport in these polymer-grafted adsorbents is best expressed in terms of the chemical potential gradient.

Tao et al. [78][79] investigated the equilibrium adsorption and kinetics of the deamidated charge variants of a mAb on UNOSphere S and Capto S. The latter is polymer-grafted while the former is an ungrafted macroporous resin. These authors observed that competitive adsorption of the charge variants was best described by the SMA model with binding capacity on Capto S greatly exceeding those of UNOSphere S at low ionic strengths. The adsorption kinetics on UNOSphere S was found to be controlled by pore diffusion with a pore diffusion model accurately predicting one-component adsorption as well as the adsorption of two- and three-component mixtures. Similarly to the results of Almodovar et al. [22], adsorption rates on Capto S were much faster than those observed for UNOSphere S; however, only a solid diffusion model could describe single and two-component adsorption in the polymer. This model failed to adequately predict adsorption kinetics when a more deamidated variant pre-adsorbed on Capto S was displaced by a less deamidated one. In this case, the kinetics of the displacement process was much slower than predicted indicating that

the pre-adsorbed mAb variant severely hindered transport of the incoming more strongly bound variant. These authors investigated this phenomenon of hindered transport by observing transient mAb uptake by confocal microscopy [29]. The microscopic studies corroborated the batch kinetics measurements indicating that adsorption in Capto S follows a solid diffusion mechanism.

Li et al. [80] studied the transient and equilibrium adsorption of lysozyme on several alginate-polymer grafted CEX resins with varying degrees of alginate graft density. These authors observed that the binding capacity increased with increasing graft density and therefore, with charge. These authors also observed fast kinetics on these materials that was explained in terms of a "chain delivery" transport mechanism. According to this mechanism, transport is associated with fluctuations of the grafted polymers with the protein being passed along from one polymer chain to another. Wang et al. [81] studied the effects of glycidyl methacrylate chain length at various grafting densities on the binding capacity and adsorption kinetics of bovine serum albumin (BSA) and concluded that for each of the investigated chain lengths, there exists an optimal grafting density to maximize these characteristics. These authors also noted that at these optimal density-length pairs, equilibrium adsorption was at a maximum.

As discussed above, many researchers have reported the empirical effects of various polymer-graft characteristics on single-component adsorption. Few authors, have however, studied the mechanism of transport in these resins for protein mixtures. The Maxwell-Stefan theory has been used to describe multicomponent adsorption of small molecules in microporous adsorbents. For example, VanDenBroeke et al. [82] used the Maxwell-Stefan theory to describe micropore diffusion in carbon molecule sieves. These authors related the chemical potential to coupled fluxes with equilibrium described by the Langmuir isotherm model and demonstrated that adsorption kinetics could be predicted for mixtures under a wide range of conditions. More recently, the Maxwell-Stefan theory has been used to describe protein transport in chromatographic adsorbents. For

example, Lewus et al. [50] utilized the Maxwell-Stefan theory to describe single and two-component adsorption of lysozyme and cytochrome C on S-HyperD using the steric mass action model to describe equilibrium. Sun et al. [83] also used expressions based on the Maxwell-Stefan theory assuming that equilibrium is described by the Langmuir isotherm to describe the adsorption of BSA and γ-globulin on a weak anion exchanger. Tao et al. [52] modeled the adsorption kinetics of deamidated mAb variants on a polymer-grafted CEX adsorbent. These authors concluded that adsorption occurs as a result of coupled transport with equilibrium described by the SMA model. The Maxwell-Stefan flux expressions predicted the slow rates observed during displacement of one variant by the other resulting from counter diffusion. Yang [84] utilized Maxwell-Stefan diffusion expressions to describe the adsorption of mixtures of BSA and bovine hemoglobin on SP Sepharose FF, a strong cation exchanger based on agarose, assuming that equilibrium is described by the multicomponent Langmuir isotherm model. The author concluded that more accurate equilibrium adsorption models are necessary to describe multi-protein adsorption kinetics.

The work described in this chapter focuses on characterizing the structure of polymer-grafted AEX resins and on understanding its effects on protein adsorption equilibrium and kinetics. Knowledge of pore structure is important for a better mechanistic understanding of the chromatographic behavior and for improved adsorbent screening during process development. Transmission electron microscopy is used to visualize the pore structure. Inverse size exclusion chromatography (iSEC) is used to quantify the effective pore size as a function of solution composition.

The effects of protein size on equilibrium adsorption and kinetics are characterized. Macroscopic measurements are made to determine using batch equilibrium and kinetics. Confocal laser scanning microscopy is used to visualize the intraparticle bound protein concentration profiles during transient adsorption of BSA and Tg both separately and in a mixture. Single component and two-component breakthrough curves are obtained for BSA and Tg at various NaCl concentrations. Two-component

breakthrough quantified the effects of solution compositions on the separation of large and small proteins on polymer-grafted adsorbents. Finally, mechanistic models are developed to describe transport in macroporous and polymer-grafted adsorbents. These models are adapted to two-component column behavior to understand thee underlying transport mechanism in polymer-grafted adsorbents.

2.2 Materials and methods

2.2.1 Materials

The proteins used in this work are BSA and bovine Tg, both obtained from MilliporeSigma (St. Louis, MO, USA). Table 2.1 shows some of their properties. Chemicals used to prepare buffers were purchased from MilliporeSigma. The primary buffering species used is bis-tris propane (BTP). The BSA sample contained 10-20% aggregate species that were removed by gradient elution chromatography in 20 mM BTP-HCl at pH 7.0 using a 0-500 mM NaCl gradient over 30 CV on an 8 mL Source 15Q column (Cytiva, Marlborough, MA, USA) followed by buffer exchange with a Hi Prep 26/10 desalting column (Cytiva). Tg contains 15% dimeric species because of its very high cost, purification was deemed impractical. Thus, Tg was used as received.

Table 2.1: Relevant biophysical properties of BSA and Tg.

Protein	Molecular Weight (kDa)	D_0 from DLS (10^{-7} cm^2/s)	r_H (nm)	pI
BSA	66.4	6.0 ± 0.2	3.4 ± 0.1	4.7
Tg	660	2.2 ± 0.1	8.7 ± 0.2	4.5

Four AEX chromatography resins, UNOsphere Diol Q, Nuvia HR Q, Nuvia Q, and Nuvia HP Q, supplied by Bio-Rad laboratories were used in this work. All of these resins are based on polymers made with acrylamido and vinyl co-monomers and are variants of the previously described UNOsphere and Nuvia resins [85]. Backbone porosity and pore radius were obtained via mercury porosimetry

for the dry beads. Nuvia HR Q, Nuvia Q, and Nuvia HP Q all contain polymers grafted onto the resin backbone and functionalized with quaternary ammonium ions. The structural properties of the four AEX resins are listed in Table 2.2. The polymer content and polymer length are supplied by the manufacturer. The apparent pore size of the hydrated particles was determined by inverse size-exclusion chromatography (iSEC) using dextran probes. The dextran probes used for this purpose ranged in molecular weights from 4 to 2000 kDa.

Table 2.2: Relevant structural properties of the four AEX resins investigated in this work.

	Particle Diameter (µm)	Backbone porosity*	Backbone pore radius (nm)*	Polymer graft content (mol mass/weight %)*	Charge density (mmol/L column)
UNOsphere Diol Q	68 ± 10	0.25	20	none	71
Nuvia HR Q	50 ± 6	0.29	26	40 kDa/7%	110
Nuvia Q	75 ± 12	0.29	26	150 kDa/15%	140
Nuvia HP Q	50 ± 6	0.32	30	40 kDa/7%	91

*Provided by the manufacturer

2.2.2 Methods

The iSEC experiments were conducted with 10 µL pulse injections of samples containing 5 mg dextran/mL in 20 mM BTP-HCl at pH 7.0 containing either with 0 mM, 150 mM NaCl or 1000 mM NaCl, performed on a Waters e2695 HPLC system (Milford, MA) with a Waters 2414 refractive index detector. A distribution coefficient, K_c, was calculated from the retention volume, V_R, of each probe according to:

$$K_c = \frac{V_R/V_c - \epsilon}{1 - \epsilon} \tag{2.1}$$

where, V_c is the volume of the column and ϵ is the extra particle porosity. The later was obtained from pressure drop measurements via the Carman-Kozeny equation [31]. To determine the apparent

pore size, the experimental K_c-values from eq. 2.1 were fitted with the following expression for a bimodal pore size distribution [86]:

$$K_c = \epsilon_{p,m}\left(1 - \frac{r_m}{r_{pore,m}}\right) + \epsilon_{p,M}\left(1 - \frac{r_m}{r_{pore,M}}\right) \tag{2.2}$$

where r_m is the radius of the probe and $\epsilon_{p,m}$ and $\epsilon_{p,M}$ are the intraparticle porosities associated the small and large pores of radius $r_{pore,m}$, and $r_{pore,M}$, respectively. A constraint on eq. 2.2 is that $\epsilon_{p,m}$ and $\epsilon_{p,M}$ must sum to the total porosity, obtained via glucose injections. The radius of each dextran probe was estimated from the following correlation [86]:

$$r_m = 0.0271 M_r^{0.498} \tag{2.3}$$

where M_r is the molecular weight of the dextran probe in Da.

The resin structures were observed by transmission electron microscopy (TEM) with a JOEL 100CX instrument (JOEL LTD., Tokyo, Japan). The samples used for the observations were prepared as follows. A resin slurry was washed in a water-ethanol gradient from 0 to 100% (w/v) anhydrous ethanol in 20% increments. After the 100% ethanol wash was completed, the slurry was washed with 50% LR White embedding agent and 50% ethanol followed by a 100% LR white saturation and cured for 24 hours at 45 °C. Subsequently, the resins were microtomed into 80 nm sections and stained with uranyl acetate and lead citrate.

Equilibrium adsorption capacities were obtained by mixing known quantities of each adsorbent with 1.5 mL solutions of either BSA or Tg at initial concentrations ranging from 0.5 to 4.5 mg/mL in BTP-HCl buffer at pH 7.0 containing either 0 mM or 50 mM NaCl. Measurements of the supernatant concentration were taken after 24 hours of gentle agitation. The initial and final supernatant

concentration were measured with a UV spectrophotometer (Nanodrop 2000c ThermoFisher Scientific, Waltham MA, USA). The amount of adsorbed protein was determined via mass balance. Two-component equilibrium adsorption data were collected under the same conditions as for the single component case. However, for two-component adsorption in addition to UV measurements total protein concentration, samples of the supernatant were also analyzed by UPLC using a BEH-SEC Waters UPLC column with an Acquity UPLC system to determine the concentration of each individual component.

The adsorption kinetics was investigated in a batch adsorption system as described by Ubiera et al. [87]. This system comprised of a 20 mL magnetically agitated vessel and a peristaltic pump used to continuously recirculate the supernatant solution through a UV detector. For two-component experiments, 100 µL samples of the solution were periodically withdrawn with a syringe and dispensed into a 96 well plate for UPLC analysis as previously described for the equilibrium adsorption measurements. For sequential batch adsorption experiments measurements, the resin was pre-exposed to BSA for 2 h followed by the addition of Tg. The total change in solution volume after all the samples were withdrawn was less than 2.5%.

The protein adsorption kinetics was also investigated by confocal laser scanning microscopy (CLSM) which permitted visualization of the bound protein concentration profiles within the particles as described by Zhu et al. [31]. For this purpose, Rhodamine Red-X and Rhodamine Green-X fluorescent dyes obtained from Invitrogen Corporation (Carlsbad, CA, USA) were conjugated to Tg and BSA, respectively, by reaction with primary amine residues. The conjugation reactions were conducted for 40 min for Tg and for 1 hour for BSA at room temperature in the dark with a 1:3 dye to protein molar ratio in 500 mM sodium carbonate at pH 8.5. The unconjugated dye was then separated from the protein with an Econo-10 DG desalting columns (Bio-Rad Laboratories, Hercules, CA, USA). The final molar ratios of labeled to unlabeled protein were 0.15 and 0.25

for Tg and BSA, respectively. All CLSM experiments were performed by diluting the conjugated protein with unconjugated protein to obtain a final ratio of 1:40 labeled protein to unlabeled protein. The images were taken with a Zeiss LSM 510 microscope using a Plan Apochromat 63x/1.4 NA oil objective (Carl Zeiss MicroImaging LLC, Thornwood, NY, USA).

Resin samples were placed in protein solutions in 15 mL falcon tubes rotated end-over-end and at various time-intervals small samples ($\leq$ 150 µL) were withdrawn and sieved in micro-centrifuge tubes using a Minispin bench-top centrifuge (Eppendorf, Hamburg, Germany) operated at 13,400 rpm for 30-45 sec. The particles recovered were resuspended in a buffered solution containing 50% (w/w) sucrose which matches the refractive index of the resins [22] [31].

One-component breakthrough curves, used to determine the dynamic binding capacity, were obtained for pure feeds of BSA and Tg for each resin using 0.5 cm diameter Tricorn columns (Cytiva, Marlborough, MA, USA) with packed bed heights between 2.3 and 6 cm. An AKTA^{TM} Pure 25 system (Cytiva, Marlborough, MA, USA) with UV detection at 280 nm. For the breakthrough experiments the load flow rate was varied between 0.2 and 1 mL/min mL/min corresponding to a residence time of 2 min with a protein feed concentration of 1.00 $\pm$ 0.05 mg/mL. The dynamic binding capacity (DBC) was determined from the breakthrough curves for each resin as the amount of protein loaded per unit column volume at the time when the outlet protein concentration reached 10% of the feed value. Similarly, the equilibrium binding capacity (EBC) was determined at the time when the outlet protein concentration closely approached the feed value. In some cases when adsorption was extremely slow, the outlet protein concentration did not reach the feed value. In this case, the presented EBC values represent lower-bound estimates.

Two-component breakthrough curves for mixtures of BSA and Tg were obtained using the same packed columns as those used for the single-component breakthrough experiments. In addition to

monitoring the UV signal, fractions were also taken every 1 CV and analyzed by UPLC-SEC to determine the concentration of each protein.

2.3 Structural characterization

The pore size was investigated by iSEC as described in Section 2.2.2. The resulting distribution coefficients are shown in Fig. 2.1 along with the lines calculated with eq. 2.2. In order to decrease the number of fitted parameters, $r_{pore,M}$ was set equal to 100 nm. The regressed values can be found in Table 2.3. As seen in Fig. 2.1a, salt has no effect on K_c for UNOsphere Diol Q. However, K_c increases significantly with increasing salt concentration for the polymer-grafted adsorbents indicating that the polymer-grafts change conformation in the presence of salt. Nuvia Q (Fig.2.1c) has the greatest degree of exclusion of the dextran probes, which is consistent with its higher degree of polymer-grafting.

Table 2.3: Regressed values of ϵ_m, ϵ_M, and $r_{pore,m}$ based on eq. 2.2 with $r_{pore,M} = 100$ nm.

	0 mM NaCl			50 mM NaCl			100 mM NaCl		
	ϵ_m	ϵ_M	$r_{pore,m}$	ϵ_m	ϵ_M	$r_{pore,m}$	ϵ_m	ϵ_M	$r_{pore,m}$
UNOSphere Diol Q	0.33	0.47	17.0	0.35	0.46	17.0	0.36	0.44	17.0
Nuvia HR Q	0.61	0.17	13.0	0.55	0.245	12.0	0.46	0.29	12.0
Nuvia Q	0.71	0.01	4.9	0.68	0.03	5.2	0.66	0.07	5.8
Nuvia HP Q	0.56	0.20	11.0	0.47	0.29	11.0	0.41	0.35	11.0

Figure 2.2 shows the TEM images obtained with and without incubation in BSA. The light gray areas in the images correspond to the LR White embedding resin whereas the darker areas correspond to the denser metal-stained backbone and bound protein. All of the resins appear to have a micro-granular structure. However, despite an increase in graft content, without bound protein, the polymer-grafts cannot be distinguished from the embedding resin. This is consistent with previous results

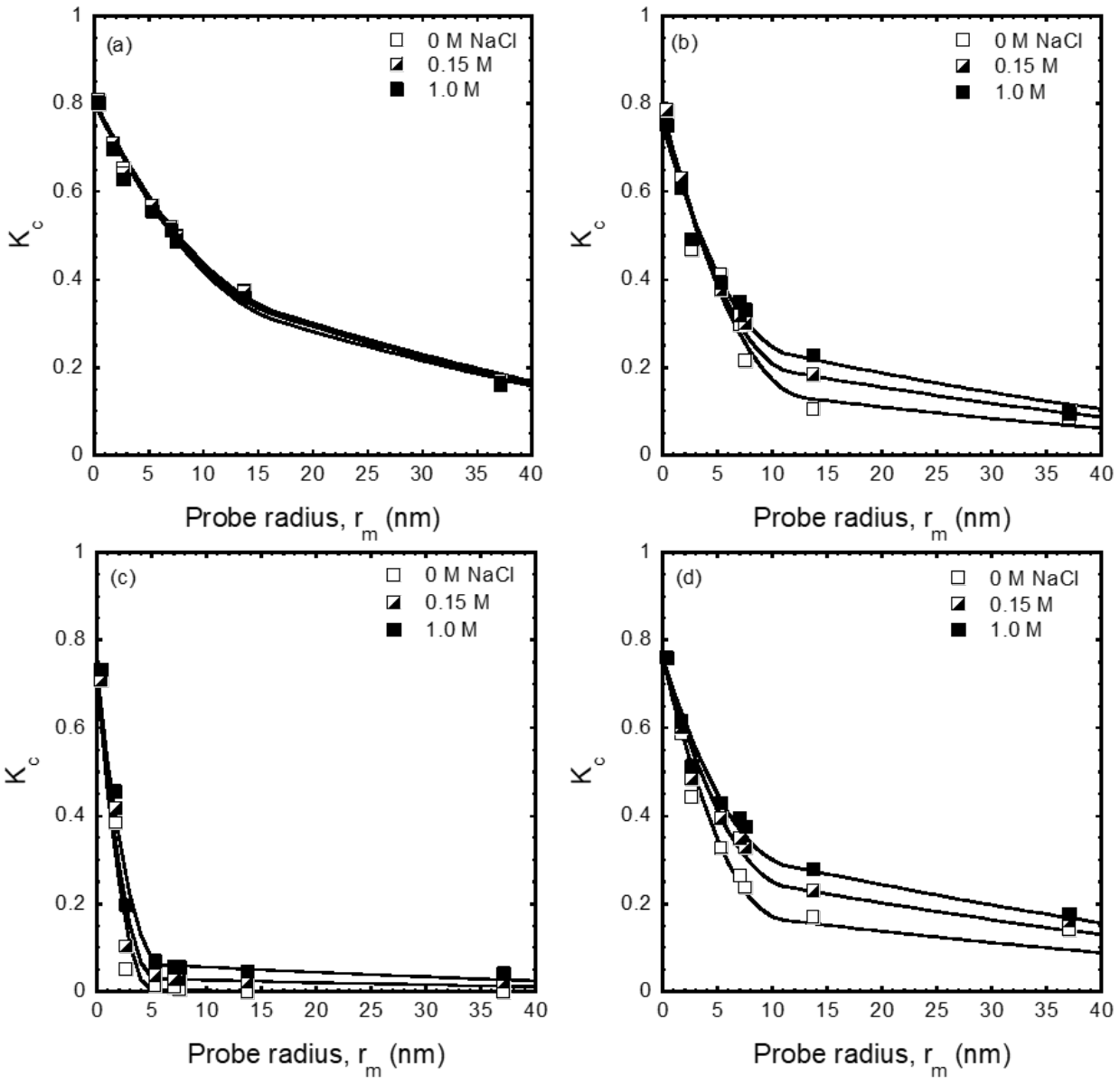

Figure 2.1: Distribution coefficients as a function of probe radius of glucose and dextrans ranging from 4 kDa to 2000 kDa on (a) UNOSphere Diol Q, (b) Nuvia HR Q, (c) Nuvia Q, and (d) Nuvia HP . Buffer: 20 mM BTP-HCl at pH 7.0 containing different NaCl concentrations as shown in the legend. The lines are based on eq. 2.2.

and is due to the low graft density [31]. In the presence of bound protein, the dark stained areas extend from the surface of the micro-granules into the pore space with increasing visibly dark areas corresponding to increases in polymer-graft content and length.

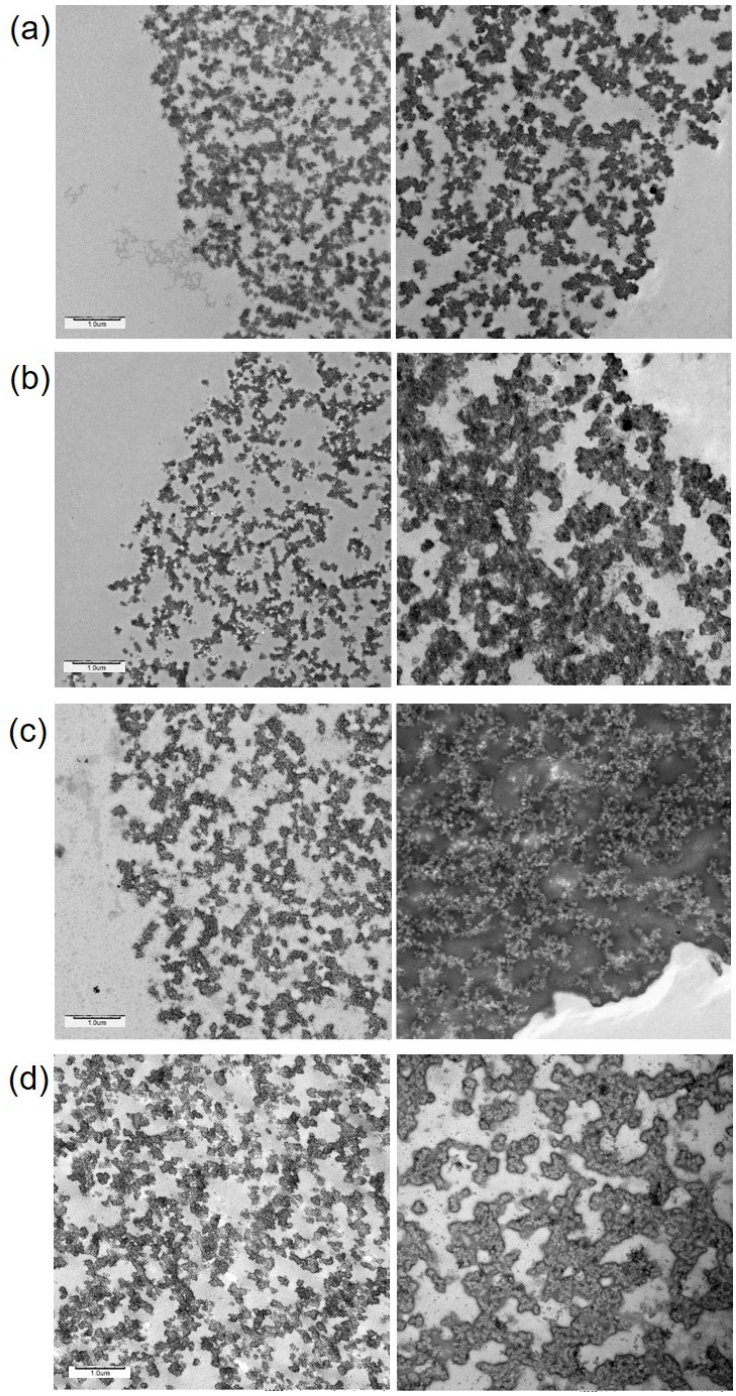

Figure 2.2: TEM Images of (a) UNOsphere Diol Q, (b) Nuvia HP Q and (c) Nuvia Q. Left column images are for clean resin samples. Right column images are for resin samples incubated in 1 mg/mL BSA for 24 h. Buffer: 20 mM BTP-HCl at pH 7.0.

2.4 Adsorption behavior

2.4.1 Single-component adsorption

Initial experiments focused on determining the equilibrium adsorption capacities of BSA and Tg on each of the resins at 0 mM and 50 mM NaCl. The results are shown in Fig. 2.3 along with lines based on the Langmuir isotherm according to the following equation:

$$q = \frac{q_m K_L C}{1 + K_L C} \tag{2.4}$$

where q is the adsorbed concentration, K_L is the adsorption constant, and C is the solution phase concentration. q_m and K_L were regressed to the data. It is important to note that for Tg adsorption without added NaCl, equilibrium was likely not reached even at 24 hours. For BSA, the binding capacity substantially increases with greater polymer content. The binding capacity decreases with increasing salt concentration. This is typical for protein binding on IEX chromatographic adsorbents and is in qualitative agreement with mass action models [88][89]. The binding capacity for BSA adsorption on Nuvia HR Q and Nuvia HP Q are similar. This suggests that the differences in pore size and porosity between the two resins has a negligible effect on BSA adsorption equilibrium. In the case of Tg without the addition of salt, the trends with regards to the grafted polymer content are less obvious. A clear trend is seen, however, when 50 mM of NaCl is added. In this case, all three polymer-grafted resins, showed a substantial binding capacity increase with increasing polymer-graft content. This suggests that protein size plays a significant role in the adsorption of proteins on polymer-grafted adsorbents. Typically increasing NaCl concentrations should decrease the binding capacity in IEX resins.

Tg adsorption on the four AEX resins was further investigated by CLSM. The CLSM images are

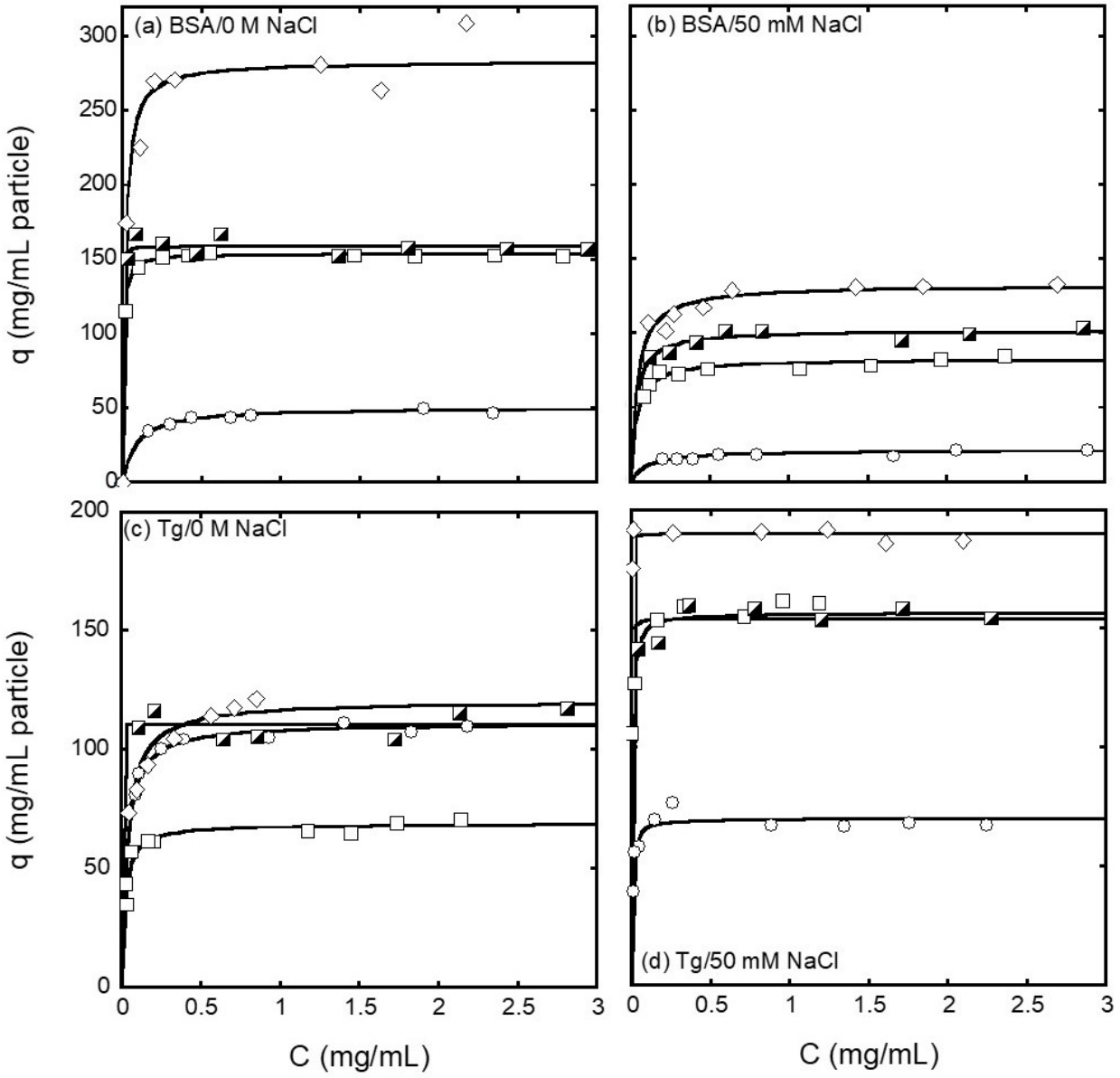

Figure 2.3: Adsorption measurements of Tg or BSA on UNOsphere Diol Q, Nuvia HR Q, Nuvia Q, and Nuvia HP Q. Saturation time: 24 hours. Lines based on the Langmuir adsorption isotherm, eq.2.4. (○) UNOsphere Diol Q (□) Nuvia HR Q (◪) Nuvia HP Q (◇) Nuvia Q.

shown in Figs. 2.4 and 2.5. Without the addition of NaCl (Fig. 2.4), by 2 h there is little fluorescence in the center of the Nuvia HR Q and Nuvia HP Q particles indicating little adsorption. On the other hand, with the inclusion of 50 mM NaCl, we can observe that Tg has diffused into the center of the polymer-grafted adsorbents within 40 min. Comparing Tg adsorption in particles with (Fig. 2.5) and without (Fig. 2.4) 50 mM NaCl added to the buffer, it is evident that Tg diffuses into the particles more quickly with the inclusion of 50 mM NaCl. The intraparticle diffusion profiles differ qualitatively between the polymer-grafted resins and UNOsphere Diol Q suggesting that mass transfer is governed by different mechanisms. In the case of UNOSphere Diol Q, a sharp protein front is observed indicative of a pore diffusion mechanism whereas in Fig. 2.5b, 2.5c, and 2.5d we observe smooth profiles consistent with a solid diffusion mechanism.

The following model was used to describe the batch uptake data:

$$\epsilon_p \frac{\partial c_i}{\partial t} + \frac{\partial q_i}{\partial t} = \frac{D_{e,i}}{r^2} \frac{\partial}{\partial r} \left(r^2 \frac{\partial c_i}{\partial r} \right) \tag{2.5a}$$

$$\left. \frac{\partial c_i}{\partial r} \right|_{r=0} = 0 \tag{2.5b}$$

$$\left. c_i \right|_{r=r_p} = C_i \tag{2.5c}$$

$$\frac{dC_i}{dt} = -\frac{3V_M}{r_p V} D_{e,i} \left. \frac{\partial c_i}{\partial r} \right|_{r=r_p} \tag{2.6a}$$

$$C_i = \left. C_{0,i} \right|_{t=0} \tag{2.6b}$$

where c_i is the pore liquid concentration, q_i is the adsorbed phase concentration, C_i is the external solution concentration, V_M is the resin volume, and V is the volume of the solution. D_e, i is an apparent effective diffusivity obtained by regressing the model to the data. Assuming that the

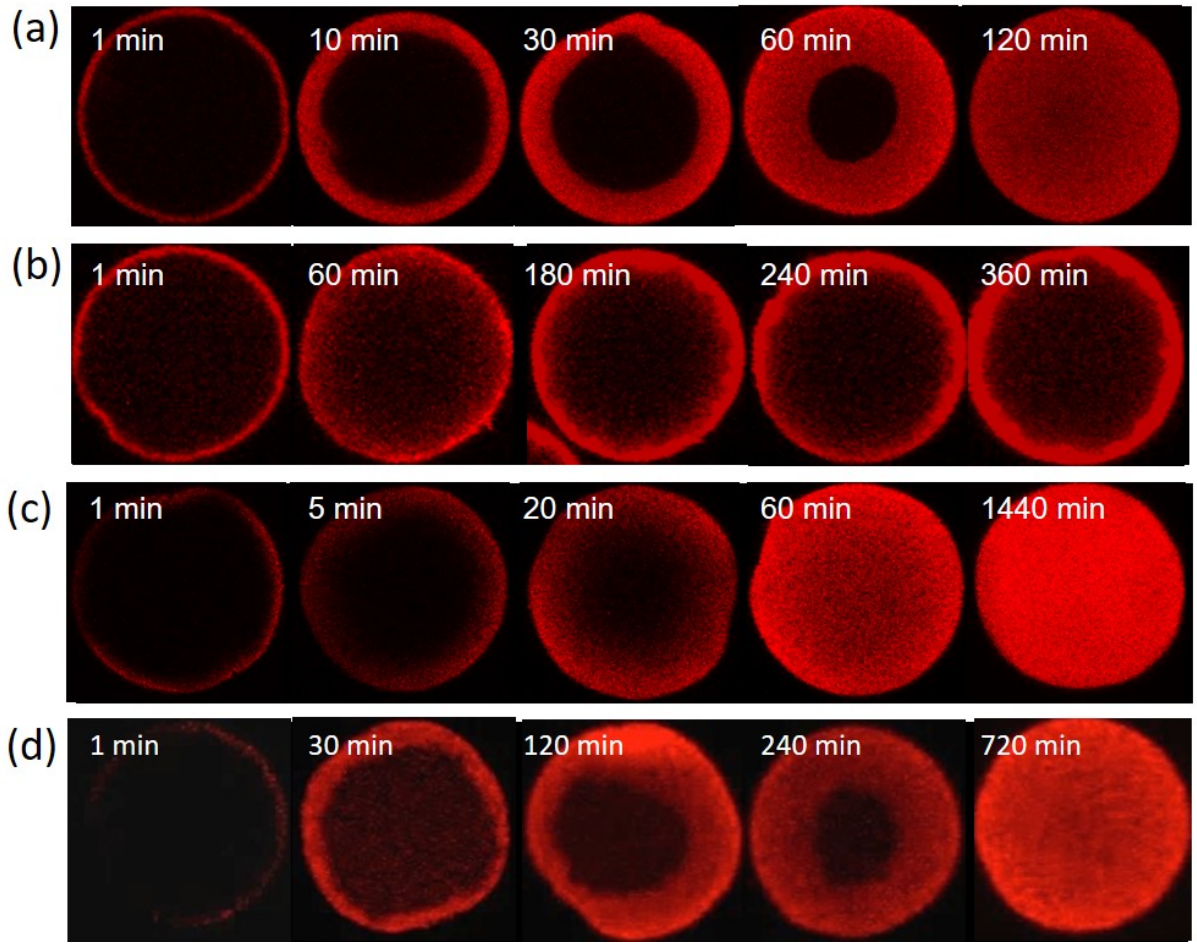

Figure 2.4: Adsorption of Tg on (a) UNOsphere Diol Q, (b) Nuvia HR Q, (c) Nuvia HP Q, and (d) Nuvia Q. No added NaCl. 20 mM BTP-HCl at pH 7.0. containing no NaCl

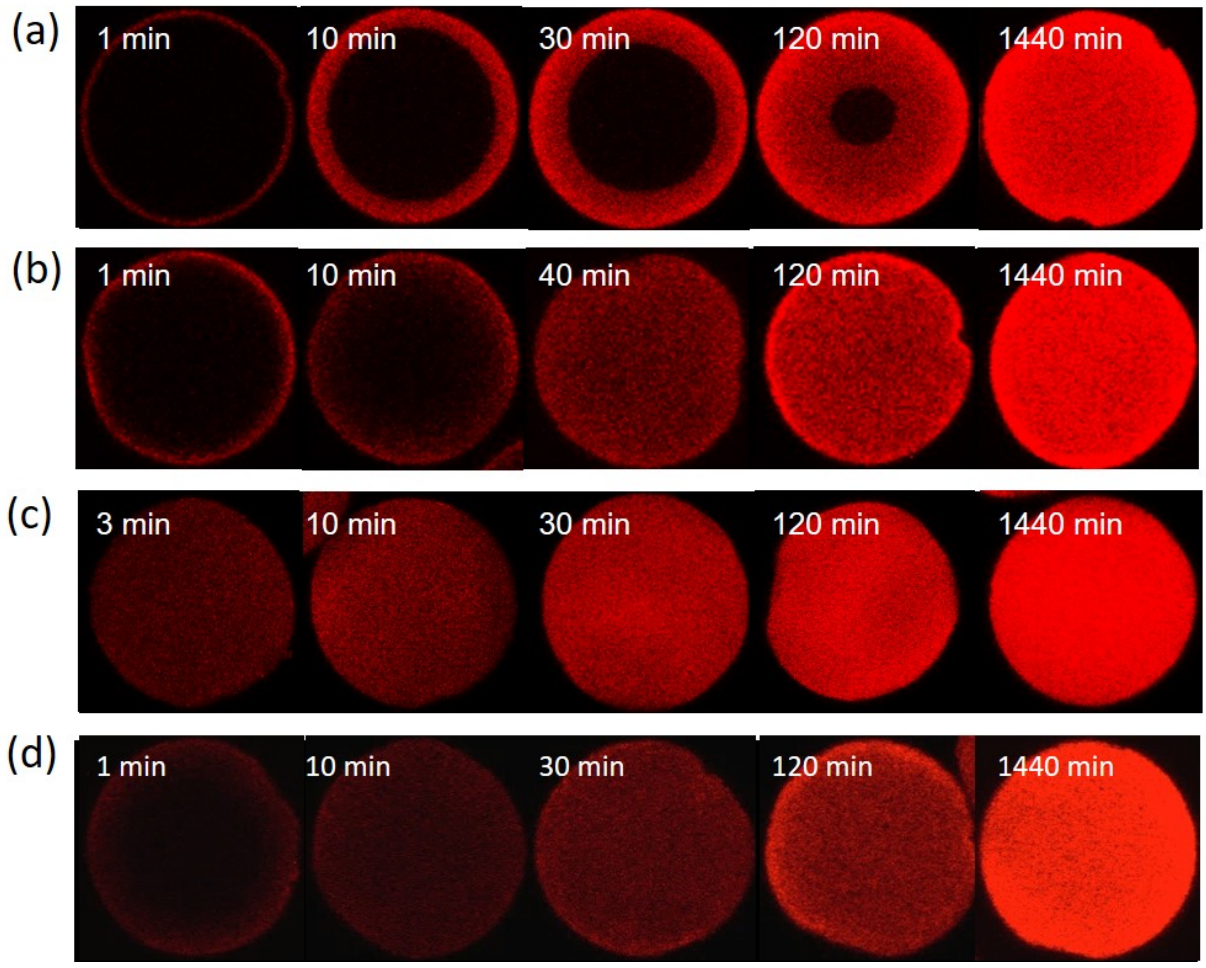

Figure 2.5: Adsorption of Tg on (a) UNOsphere Diol Q, (b) Nuvia HR Q, (c) Nuvia HP Q, and (d) Nuvia Q.Buffer: 20 mM BTP-HCl at pH 7.0 containing 50 mM NaCl

adsorption isotherm is rectangular, and that pore diffusion is indeed dominant, eqs.2.5-2.6 yield the following solution (omitting the i subscript) [28][75][90][91] are:

$$\begin{gathered}\frac{C_0}{q_m}\frac{D_e t}{r_p^2} = \left(1 - \frac{1}{Bi}\right) I_2 - I_1 \\ I_1 = \frac{1}{6\lambda\Lambda}\ln\left[\frac{\lambda^3+\eta^3}{\lambda^3+1}\left(\frac{\lambda+1}{\lambda+\eta}\right)\right] + \frac{1}{\lambda\Lambda\sqrt{3}}\left[tan^{-1}\left(\frac{2\eta-\lambda}{\lambda\sqrt{3}}\right) - tan^{-1}\left(\frac{2-\lambda}{\lambda\sqrt{3}}\right)\right] \\ I_2 = \frac{1}{3\Lambda}\ln\left(\frac{\lambda^3+\eta^3}{\lambda^3+1}\right) \\ \eta = (1-F)^{1/3} \\ \lambda = \left(\frac{1}{\Lambda} - 1\right)^{1/3} \\ \Lambda = \frac{V_M q_m}{V C_0}\end{gathered} \tag{2.7}$$

Where $F = \overline{q}/q_m$ is the fractional approach to saturation and $Bi = \frac{k_f r_p}{D_e}$, is the Biot number. In most practical cases, $Bi > 10$ indicating that the external resistance is negligible. These equations were used to fit the Nuvia uptake curves since their particle size distribution (PSD) is narrow. Conversely, eqs. A16-A18 in Stone and Carta [36] which account explicitly for particle size distribution, were used to fit the UNOSphere Diol Q data since this resin has a relatively broad PSD.

Figure 2.6 shows the batch adsorption data along with lines calculated from the model. For BSA on all four AEX resins equilibrium is quickly reached in under 15 min. For Tg, however, much longer times are required to approach equilibrium. For UNOsphere Diol Q, equilibrium is approached in 80 min; however, for the polymer-grafted AEX resins equilibrium is not approached even at 2 h. This suggests that proteins substantially smaller than the pore size undergo enhanced transport under strong binding conditions (low conductivity, high protein charge). In contrast, Tg experienced diffusional hindrance under strong binding conditions (0 mM NaCl) and enhanced diffusional mobility

under conditions when binding was slightly weakened (50 mM NaCl). The larger average pore size of Nuvia HP Q compared to that of Nuvia HR Q alleviates some of the steric effects that slowed Tg transport. Whereas Tg adsorption on Nuvia HR Q primarily occurred on the particle surface which decreased the apparent equilibrium binding capacity, considerable penetration of Tg is seen with Nuvia HP Q.

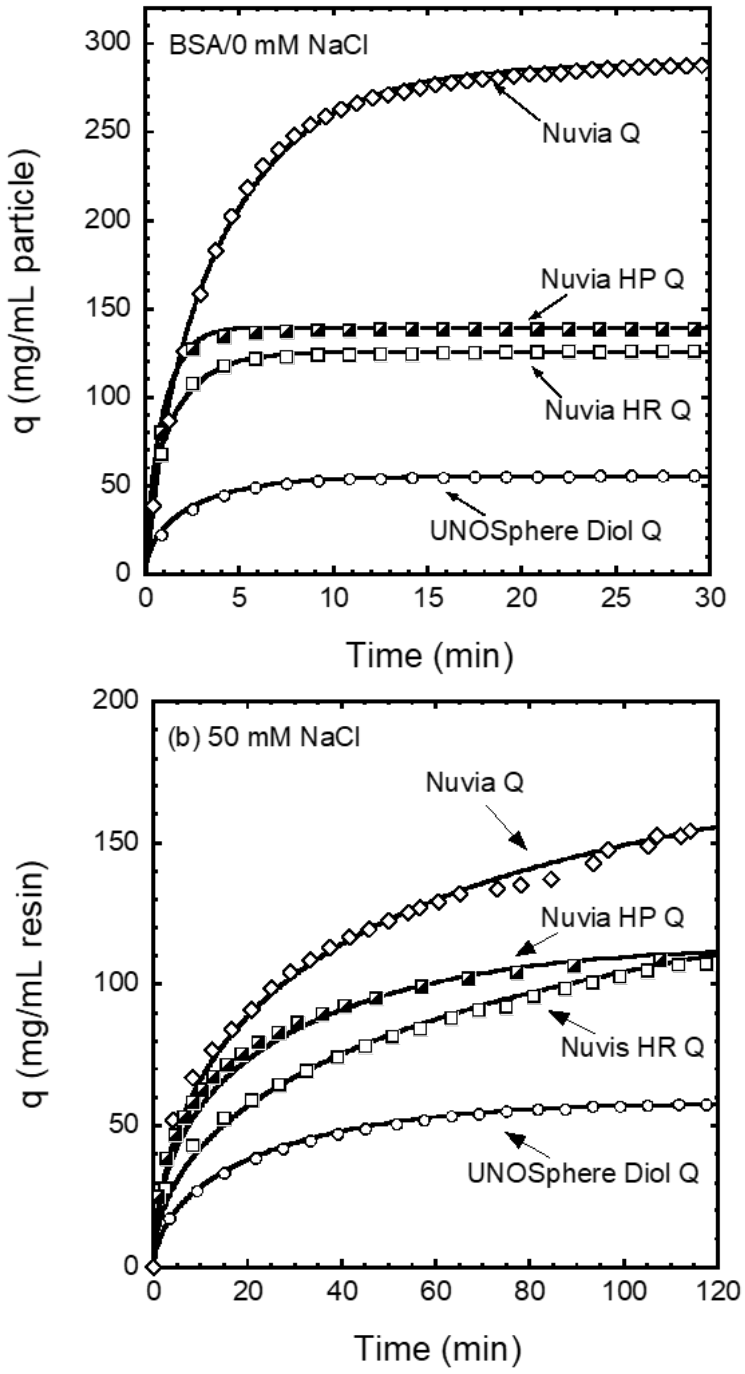

Figure 2.6: Batch adsorption kinetics of (a) BSA with no added salt and (b) Tg with 50 mM added NaCl on the four AEX resins. Buffer: 20 mM BTP-HCl at pH 7.0. (○) UNOsphere Diol Q (□) Nuvia HR Q (◪) Nuvia HP Q (◇) Nuvia Q.

As is well known [28], pore and solid diffusion models predict nearly indistinguishable batch uptake curves. Thus, transport mechanisms cannot be discerned simply by comparing batch uptake data with models. Better mechanism discrimination is possible, however, by examining the intraparticle concentration profiles obtained from CLSM. Pore diffusion with a rectangular isotherm is characterized by sharp intraparticle bound concentration profiles. Conversely, solid diffusion is characterized by smooth intraparticle concentration profiles. It has been reported that in polymer-grafted adsorbents surface of solid-phase diffusion is the dominant transport mechanism [29]. Since surface diffusion and pore diffusion are based on different driving forces the surface or solid-phase diffusivity, D_s and apparent effective pore diffusivity, $D_{e,app}$, are related to each other by the following equation [92]:

$$D_s \sim D_{e,app}\frac{C}{q_m} \tag{2.8}$$

Table 2.4 summarizes the values of $D_{e,app}/D_0$ determined by fitting the batch uptake data with eqs. 2.5 and 2.8. As seen from this table, BSA exhibits enhanced transport ($D_{e,app}/D_0 > 1$) for all three polymer-grafted resins. Tg adsorption in both Nuvia Q and Nuvia HP Q shows $D_{e,app}/D_0$ values greater than that observed for UNOSphere Diol Q indicating that a solid diffusion mechanism enhances transport relative to pore diffusion. On the other hand, $D_{e,app}/D_0$ for Nuvia HR Q relative to UNOSphere Diol Q suggests that the low grafting content and smaller pore size (compared to Nuvia HP Q) may result in Tg occluding the pores hindering transport. The corresponding D_s values for Tg from eq. 2.8 using data from Table 2.4 are 5.6×10^{-11}, 2.7×10^{-10}, and 2.8×10^{-10} cm^2/s for Nuvia HR Q, Nuvia Q, and Nuvia HP Q, respectively.

Table 2.4: Summary of the apparent effective diffusivities that describe BSA and Tg adsorption kinetics on UNOsphere Diol Q, Nuvia HR Q, Nuvia Q, and Nuvia HP Q. D_0 is the free solution diffusivity.

		UNOsphere Diol Q	Nuvia HR Q	Nuvia Q	Nuvia HP Q
	NaCl (mM)	$D_{e,app}/D_0$	$D_{e,app}/D_0$	$D_{e,app}/D_0$	$D_{e,app}/D_0$
BSA	0	0.35	1.2	2.3	2.5
Tg	50	0.09	0.05	0.23	0.14

2.4.2 Two-component adsorption

Understanding the interactions between the polymer-grafts and multiple proteins is crucial for many practical applications. As shown in Section 2.4.1, for single protein adsorption, equilibrium conforms to the Langmuir adsorption isotherm with pore and surface diffusion models suitably describing uptake kinetics for the ungrafted and grafted resins, respectively. Polymer-grafts increase the complexity of the associated transport phenomena and this complexity is compounded when for adsorption of proteins differing in size and molecular weight [93].

In the case of reversible adsorption, a larger, more strongly bound species can, in principle, displace a smaller more weakly bound one. Despite this process being thermodynamically favorable, its occurrence in porous particles requires that the strongly bound species can access the chromatographic surface. Small pores and slow adsorption kinetics can thus hinder displacement in these materials. Figure 2.7 shows the results of two-component adsorption measurements for Tg-BSA mixtures on each resin for both coadsorption and sequential adsorption in comparison with the results obtained for the adsorption of Tg alone. The following observations about Tg adsorption kinetics can be made.

For the ungrafted macroporous adsorbent (UNOSphere Diol Q, Fig. 2.7a) single component adsorption of Tg nearly coincides with the two-component coadsorption and sequential adsorption cases suggesting

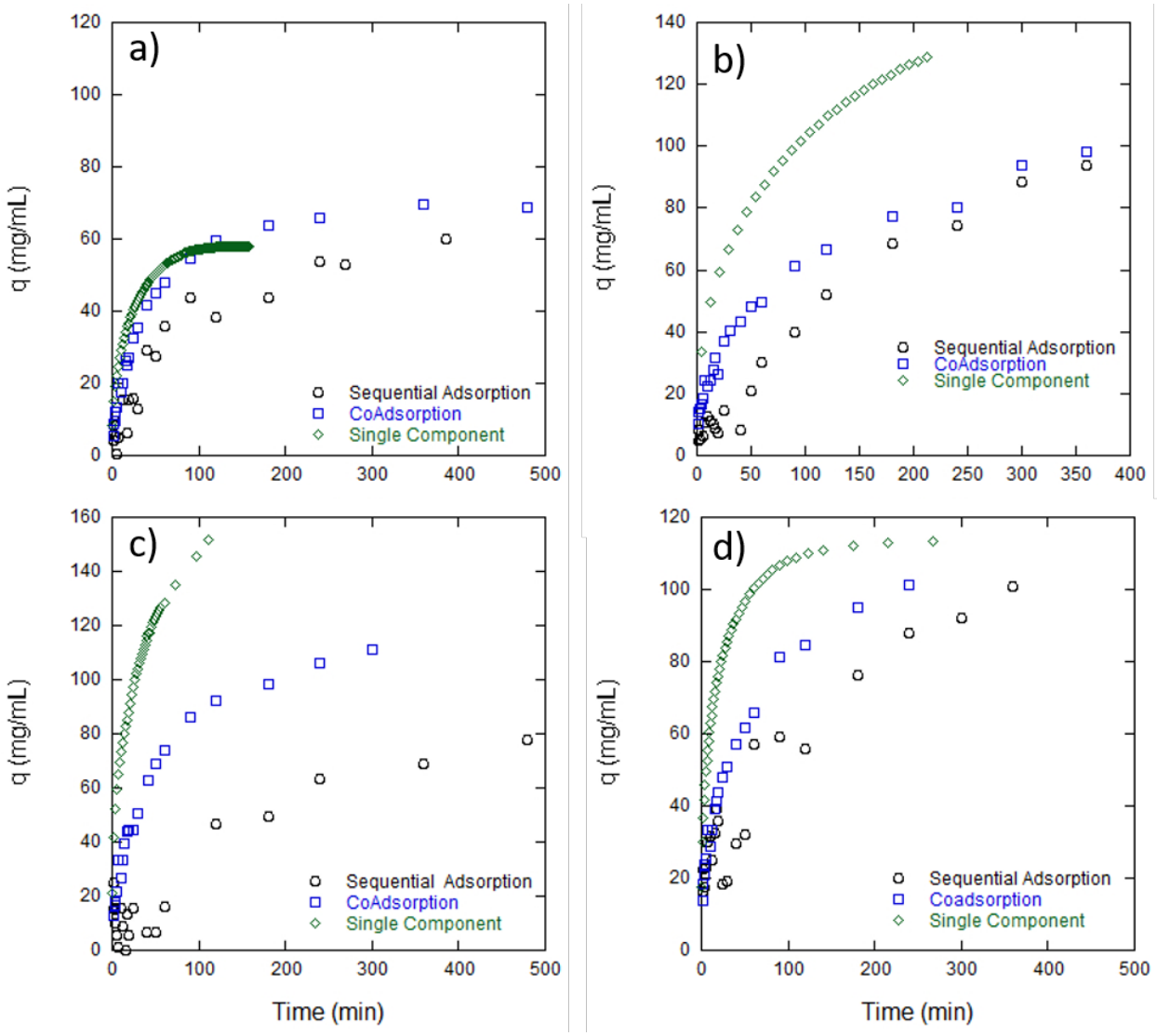

Figure 2.7: Two-component adsorption kinetics for the adsorption of mixtures containing 1 mg/mL Tg and 1 mg/mL BSA (coadsorption) and 1 mg/mL Tg following 2 mg/mL BSA for 2 h in comparison with results obtained for the single component adsorption of 1 mg/mL Tg. On (a) UNOSphere Diol Q, (b) Nuvia HR Q (c) Nuvia Q, and (d) Nuvia HP Q. Buffer: 20 mM BTP-HCl containing 50 mM NaCl pH 7.

that displacement of BSA by Tg occurs with relative ease. Conversely, for the grafted resins, both two-component coadsorption and sequential adsorption occur much slower than single component adsorption. As noted by several authors for other polymer-grafted adsorbents [50][51][52][94], counter-diffusion of the displaced protein occurs slowly limiting the rate at which the displacer protein can bind. This effect is especially pronounced for Nuvia Q (Fig. 2.7c) where essentially the entire pore volume is filled with polymer grafts. For both of the resins with low polymer grafting (Nuvia HR and Nuvia HP Q), the two-component coadsorption and sequential adsorption are slower than for Tg alone, but, the decrease in apparent uptake rates is not as pronounced as for Nuvia Q. The decrease in the rate of Tg uptake due to BSA counter-diffusion is not as significant likely because this hindrance is partially alleviated by parallel diffusion through the pore and polymer-graft phases. The larger pore size of Nuvia HP Q (Fig. 2.7d) compared to that of Nuvia HR Q (Fig. 2.7b) allows for fast pore diffusion to occur decreasing hindrance due to BSA counter diffusion in the polymer-graft phase.

Accurately describing equilibrium is essential to predicting mixture adsorption kinetics. If equilibrium is not well described, the adsorption kinetics cannot be accurately predicted. For protein mixtures, the choice of isotherm model is especially important. The multicomponent Langmuir isotherm is often used to describe two-component equilibrium adsorption and is expressed as [95]:

$$q_i = \frac{q_{m,i} K_{L,i} C_i}{1 + \sum_{j=1}^{N} K_{L,j} C_j} j, i = 1, ...N \tag{2.9}$$

Since thermodynamic consistency requires $q_{m,i} = q_{m,j}$ the multicomponent Langmuir isotherm is only useful in for mixtures of similar species that have the same saturation capacity. The following isotherm developed by Gu et al. [96] has been developed to explicitly account for different saturation capacities. Assuming that Tg displaces BSA this isotherm model can be written as [96]:

$$q_{BSA} = \frac{K_{BSA}C_{BSA}\left[\left(1 + K_{Tg}C_{Tg}\right)q_{m,BSA} - \zeta K_{Tg}C_{Tg}q_{m,Tg}\right]}{1 + K_{BSA}C_{BSA} + K_{Tg}C_{Tg} + (1-\zeta)K_{BSA}C_{BSA}K_{Tg}C_{Tg}} \tag{2.10a}$$

$$q_{Tg} = \frac{K_{Tg}C_{Tg}\left[\left(1 + K_{BSA}C_{BSA}\right)q_{m,Tg} - K_{BSA}C_{BSA}q_{m,BSA}\right]}{1 + K_{BSA}C_{BSA} + K_{Tg}C_{Tg} + (1-\zeta)K_{BSA}C_{BSA}K_{Tg}C_{Tg}} \tag{2.10b}$$

where ζ is a discount factor that accounts for the unequal saturation capacity of BSA and Tg. This isotherm model has been previously used to describe mAb monomer and dimer adsorption on CEX resins as an improvement over the SMA model [97]. Note that for single component adsorption the eq. 2.10 reduces to the Langmuir isotherm. The equilibrium data are is shown in Figs. 2.8 and 2.9 along with surfaces based on eq. 2.10 using parameters regressed by minimizing the weighted absolute percentage errors (WAPE) between data and model. The regressed best-fit parameters are shown in Table 2.6. The WAPE from fitting the two-component equilibrium data for each adsorbent with eqs. 2.9 and 2.10 are shown in Table 2.5. For the polymer-grafted AEX resins, eq. 2.10 describe both single and multicomponent equilibrium adsorption while providing an improved fit over eq. 2.9.

The transient coadsorption of BSA and Tg was observed by CLSM and is shown in Fig. 2.10. As seen in Fig. 2.10a, the intraparticle concentration profiles for UNOsphere Diol Q are characterized by a relatively sharp Tg adsorption front with almost no binding of BSA consistent with pore diffusion. In this case, the adsorption process is complete in less than 2 h. The uniform low-level green signal evident when equilibrium is reached suggests that small pores that are inaccessible

Table 2.5: Comparison of the WAPE for the multicomponent equilibrium adsorption data described by eqs. 2.9 and 2.10 for each of the AEX resins.

	UNOsphere Diol Q		Nuvia HR Q		Nuvia Q		Nuvia HP Q	
	eq. 2.9	eq. 2.10	eq. 2.9	eq. 2.10	eq. 2.9	eq. 2.10	eq. 2.9	eq. 2.10
WAPE	4.6%	6.3%	9.3%	8.9%	7.2%	4.5%	8.1%	6.1%

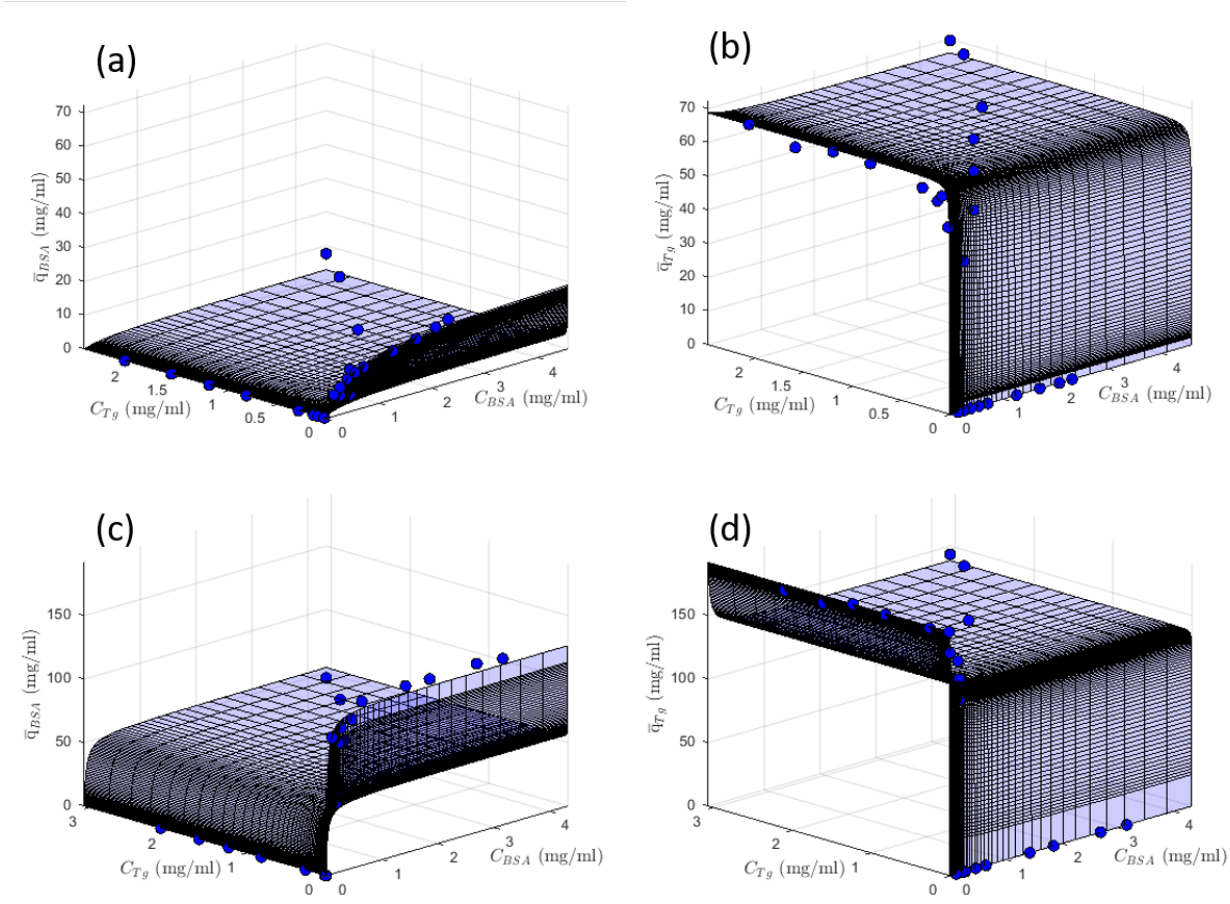

Figure 2.8: Two-component adsorption isotherms on UNOSphere Diol Q (a,b) and Nuvia Q (c,d) for BSA (a,c) and Tg (b,d) in 20 mM BTP-HCl containing 50 mM NaCl at pH 7. The surface lines are calculated from eq. 2.10 using the regressed best-fit parameter shown in Table .

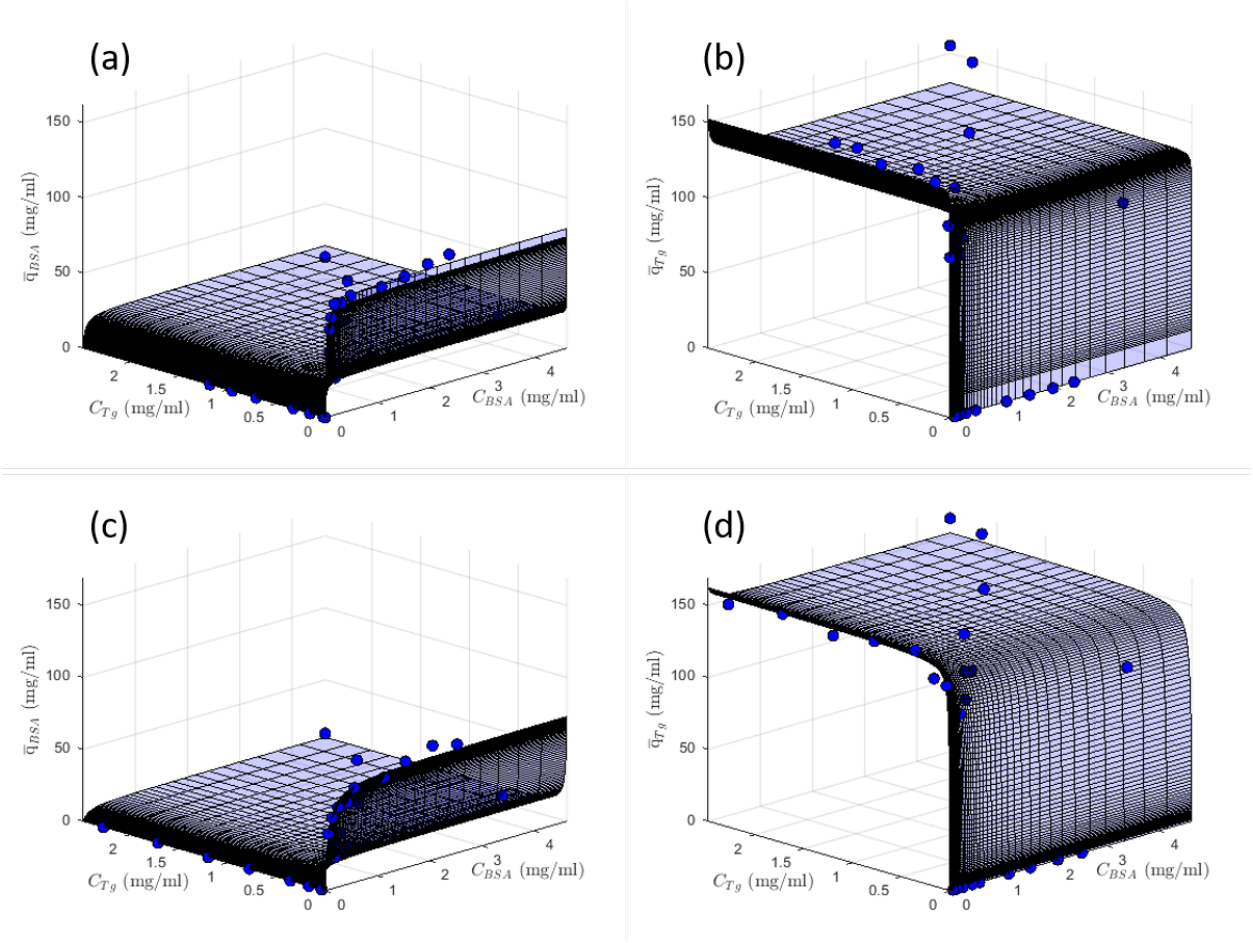

Figure 2.9: Two-component adsorption isotherms on Nuvia HR Q (a,b) and Nuvia HP Q (c,d) for BSA (a,c) and Tg (b,d) in 20 mM BTP-HCl containing 50 mM NaCl at pH 7. The surface lines are calculated from eq. 2.10 using the regressed best-fit parameter shown in Table .

to Tg present as also shown by the bimodal pore distribution. As seen in Fig. 2.10b, 2.10c, and 2.10d, the CLSM images of the polymer-grafted resins show that BSA is adsorbed quickly, in agreement with the single component measurements; however, Tg diffuses rapidly into the center of the particles without causing considerable displacement of BSA. Unlike UNOsphere Diol Q, a fast displacement effect is not observed for the polymer-grafted resins. This demonstrates that both proteins are bound to the polymer-grafts at the observed times, consistent with the batch kinetic measurements shown in Fig. 2.7. Overall, this result is consistent with the results obtained by Almodovar et al. [51] for the adsorption of mAbs on polymer-grafted CEX resins which showed smooth intraparticle concentration profiles.

The results of batch coadsorption experiments are shown in Fig. 2.11. Model lines are based on pore diffusion for UNOSphere Diol Q (eqs. 2.5, 2.6) and on solid diffusion for the polymer-grafted resins. The expressions for solid diffusion are:

$$\frac{\partial q}{\partial t} = \frac{D_s}{r^2}\frac{\partial}{\partial r}\left(r^2\frac{\partial q}{\partial r}\right) \tag{2.11a}$$

$$\left.\frac{\partial q}{\partial r}\right|_{r=0} = 0 \tag{2.11b}$$

$$q\Big|_{r=r_p} = q^*(C) \tag{2.11c}$$

Where $q^*(C)$ is the adsorbed phase concentration in equilibrium with the fluid phase. In order to solve these equations, they were converted to a system of ordinary differential equations by finite differences with 50 radial discretization points. The resulting ODE system was solved using MATLAB function ode15s. As seen in Fig. 2.11, predictions based on these models are in poor agreement with the data for all four resins, but especially for the three grafted resins. In particular, the model does not predict the overshoot of the bound BSA that is observed experimentally at early

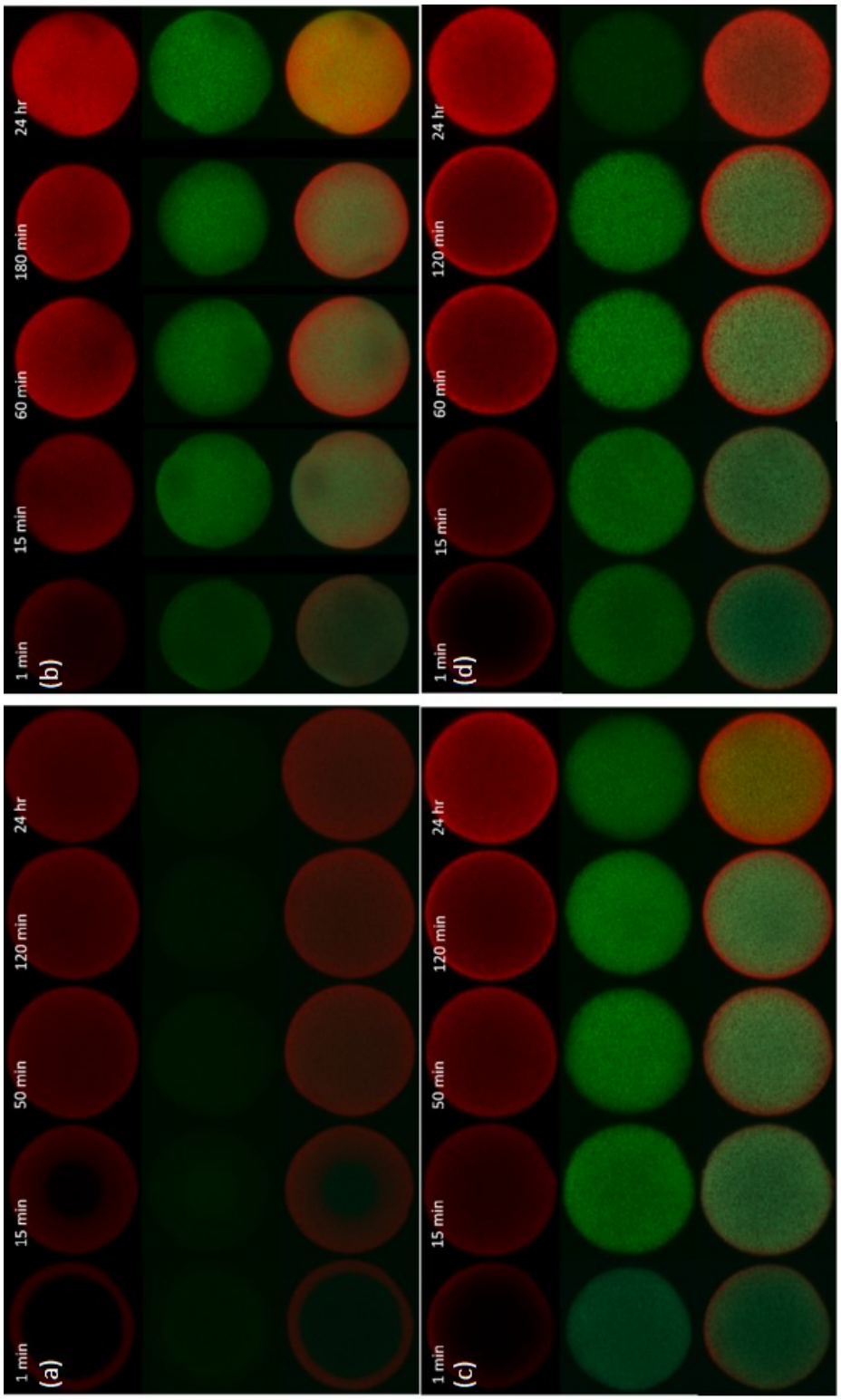

Figure 2.10: Coadsorption of Tg and BSA at 1 mg/mL each on (a) UNOsphere Diol Q $d_p = 68 \pm 2$ µm, (b) Nuvia Q $d_p = 75 \pm 2$ µm, (c) Nuvia HR Q $d_p = 50 \pm 2$ µm, (d) Nuvia HP Q $d_p = 50 \pm 2$ µm. Buffer: 20 mM BTP-HCl at pH 7.0 containing 50 mM NaCl. Top Row: red Channel (Tg) . Middle Row: green channel (BSA). Bottom Row: digital superposition of red and green channels.

times. In order to describe these results, improved models are needed.

In the case of UNOSphere Diol Q, an improved prediction can be obtained by modifying the adsorption isotherm. The iSEC results in Fig. 2.1 and the fact that some BSA remains bound throughout UNOsphere Diol Q when equilibrium is reached suggests that a two-site Langmuir model may provide a better description of equilibrium in this system [98][99][100]. Assuming that competitive binding occurs on one type of site while non-competitive binding of BSA occurs on the other the following result is obtained:

$$q_{BSA} = \frac{K_{BSA,1}C_{BSA}\left[\left(1+K_{Tg}C_{Tg}\right)q_{m,BSA,1} - \zeta K_{Tg}C_{Tg}q_{m,Tg,1}\right]}{1+K_{BSA,1}C_{BSA,1}+K_{Tg}C_{Tg}+(1-\zeta)K_{BSA,1}C_{BSA,1}K_{Tg}C_{Tg}} + \frac{q_{m,BSA,2}K_{BSA,2}C_{BSA}}{1+K_{BSA,2}C_{BSA}} \tag{2.12a}$$

$$q_{Tg} = \frac{K_{Tg}C_{Tg}\left[\left(1+K_{BSA,1}C_{BSA}\right)q_{m,Tg,1} - K_{BSA,1}C_{BSA}q_{m,BSA,1}\right]}{1+K_{BSA,1}C_{BSA,1}+K_{Tg}C_{Tg}+(1-\zeta)K_{BSA,1}C_{BSA,1}K_{Tg}C_{Tg}} \tag{2.12b}$$

Physically, in eq. 2.12a, the first additive term describes binding in the pores that are accessible to both proteins, while the second additive term represents binding in the pores accessible by BSA only. Refitting the equilibrium data to eq. 2.12 results in the parameters summarized in Table 2.6. The corresponding WAPE is 2.1% compared to 6.3% from eq. 2.10. Predictions, based on pore diffusion with equilibrium described by eq. 2.12 using the parameters in Table 2.6 are shown in Fig. 2.12.

Table 2.6.

For the grafted resins, the qualitative differences between the experimental and predicted curves suggest that a different rate model rather than a different isotherm expression is needed. Following prior work on polymer-grafted CEX resins [52] we uses a Maxwell-Stefan description of diffusion. The generalized matrix form of Maxwell-Stefan expression is as follows [82]:

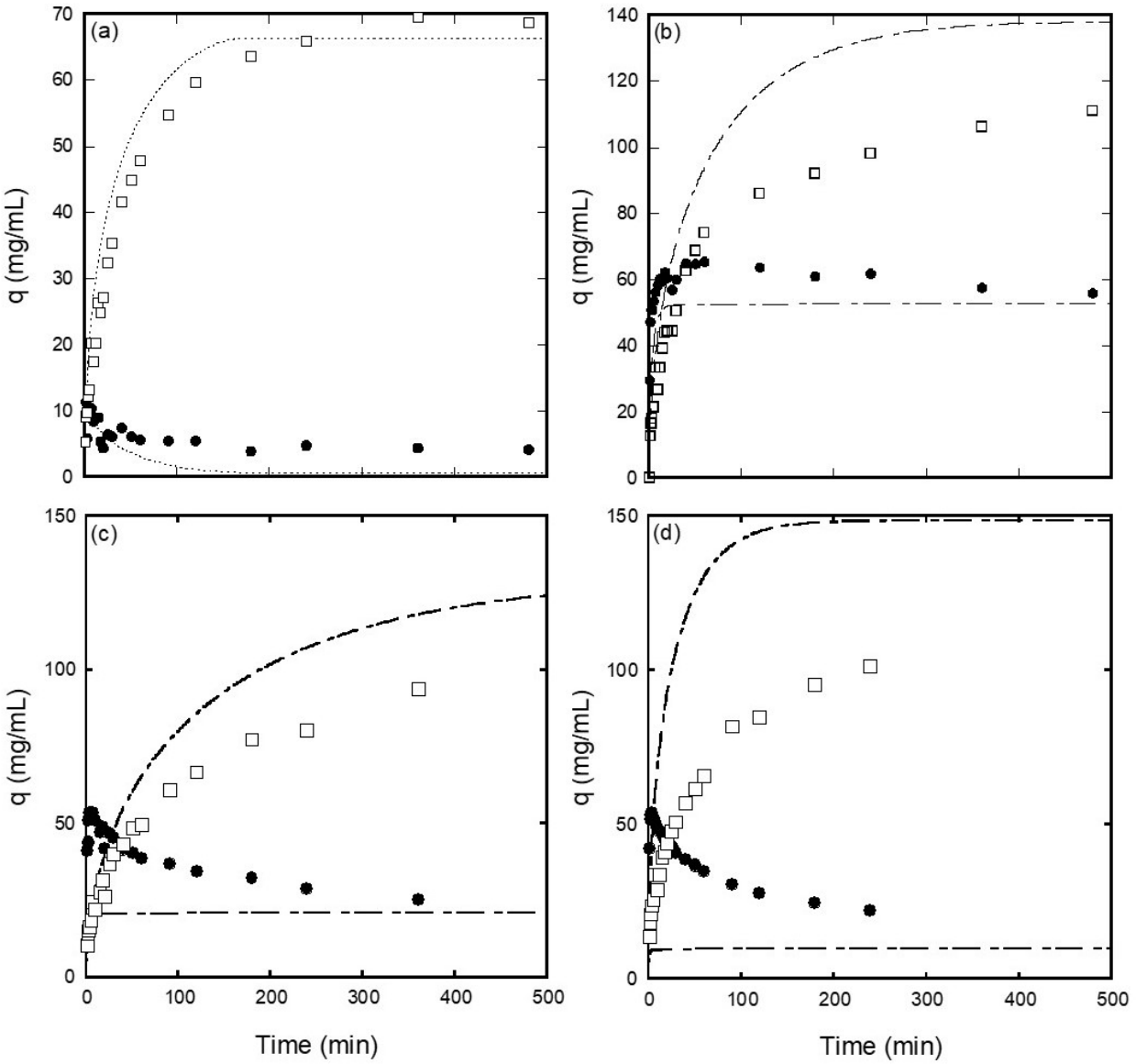

Figure 2.11: Coadsorption of BSA and Tg on (a) UNOsphere Diol Q, (b) Nuvia HR Q, (c) Nuvia Q, and (d) Nuvia HP Q. Lines are based on pore diffusion (eq. 2.5) for UNOsphere Diol Q and solid diffusion (eq. 2.11) for the three Nuvia resins, respectively. Equilibrium is described by the eq. 2.10. In each case C_0 (BSA) = 1 mg/mL and C_0 (Tg) = 1 mg/mL. Buffer: 20 mM BTP-HCl + 50 mM NaCl at pH 7.0. Diffusivities are from Table 2.4. (●) BSA (□) Tg.

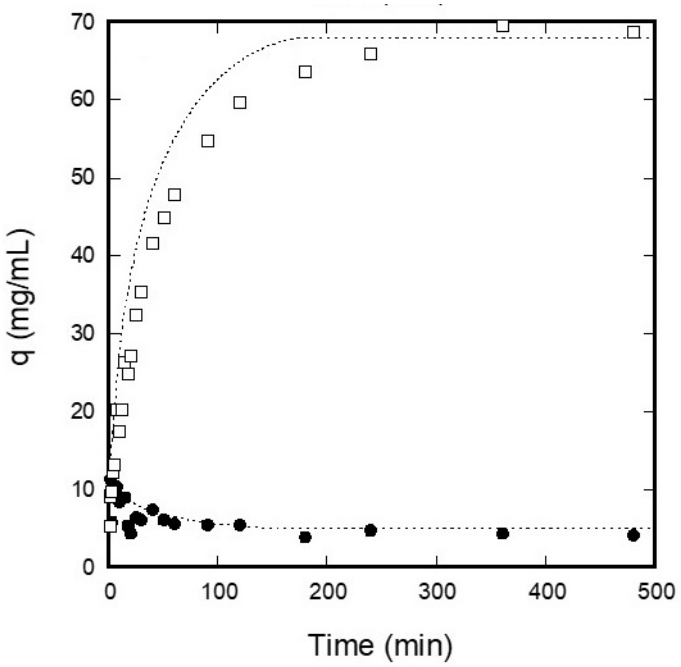

Figure 2.12: Coadsorption of BSA and Tg on UNOsphere Diol Q. Lines are based on pore diffusion, eq. 2.5 - 2.6 with equilibrium described by eq. 2.12. Data are the same as those shown in Fig. 2.11a. Diffusivities are from Table 2.4. (●) BSA (□) Tg.

Table 2.6: Best-fit regressed isotherm parameters fitted to the data in Figs 2.8 and 2.9 according to eqs. 2.12 (Fig. 2.8a-b) and eqs. 2.10 (Figs. 2.8c-d and 2.9).

	BSA				Tg		
	q_m	K	$q_{m,2}$	K_2	q_m	K	θ
UNOSphere Diol Q	19.4	0.88	4.4	42.3	67.2	471.8	0.29
Nuvia HR Q	74.6	17.6			162.4	124.7	0.38
Nuvia Q	123.8	33.2			191.4	4800	0.50
Nuvia HP Q	71.5	19.2			172.8	115.4	0.36

$$\mathbf{J} = -\mathbf{B}^{-1}\boldsymbol{\Gamma}\nabla\mathbf{q} \tag{2.13}$$

Where $\mathbf{B}^{-1}$ is the matrix of Maxwell-Stefan diffusivities and $\boldsymbol{\Gamma}$ is the matrix of thermodynamic factors that express the relationship between the chemical potential driving force and the concentration-based driving force ∇q. The derivation of the thermodynamic factors and Maxwell-Stefan diffusivities can be found in Appendix A. The resulting expressions for the coupled fluxes of two adsorbates with differing saturation capacities is given by [101]:

$$J_A = \frac{D_A\left[\left(\Gamma_{AA} + \theta_A\frac{D_B}{D_{AB}}\left(\Gamma_{AA}+\Gamma_{BA}\right)\right)\nabla q_A + \left(\Gamma_{AB} + \theta_A\frac{D_B}{D_{AB}}\left(\Gamma_{AB}+\Gamma_{BB}\right)\right)\left(\frac{q_{m,A}}{q_{m,B}}\right)\nabla q_B\right]}{\theta_B\frac{D_A}{D_{AB}} + \theta_A\frac{D_B}{D_{AB}} + 1} \tag{2.14a}$$

$$J_A = \frac{D_A\left[\left(\Gamma_{BB} + \theta_B\frac{D_A}{D_{AB}}\left(\Gamma_{BB}+\Gamma_{AB}\right)\right)\nabla q_B + \left(\Gamma_{BA} + \theta_B\frac{D_A}{D_{AB}}\left(\Gamma_{BA}+\Gamma_{AA}\right)\right)\left(\frac{q_{m,B}}{q_{m,A}}\right)\nabla q_A\right]}{\theta_B\frac{D_A}{D_{AB}} + \theta_A\frac{D_B}{D_{AB}} + 1} \tag{2.14b}$$

Where θ is the surface coverage fraction, and D_{AB} is the counter-exchange coefficient which describes the simultaneous counter-exchange of molecules adsorbed at two nearest neighbor sites [102]. The counter-exchange coefficient can be determined from the Vignes correlation [101]:

$$D_{AB}(q_A, q_B) = D_A(0)^{\left(\frac{\theta_A}{\theta_A+\theta_B}\right)} \times D_B(0)^{\left(\frac{\theta_B}{\theta_A+\theta_B}\right)} \tag{2.15}$$

Where $D_i(0)$ is the one-component diffusivity. Assuming that the cross diffusivity, D_{AB}, is infinite, these expressions simplify to:

$$J_A = D_A \left[\Gamma_{AA} \nabla q_A + \Gamma_{AB} \left(\frac{q_{m,A}}{q_{m,B}} \right) \nabla q_B \right] \tag{2.16a}$$

$$J_B = D_B \left[\Gamma_{BB} \nabla q_B + \Gamma_{BA} \left(\frac{q_{m,B}}{q_{m,A}} \right) \nabla q_A \right] \tag{2.16b}$$

which are analogous to those derived by Tao et al. [52]. The diffusion coefficients in the Maxwell-Stefan description are functions of the adsorbed concentration. Assuming that equilibrium is described by eq. 2.10, the adsorbed-concentration dependant diffusivities can be expressed as:

$$D_A \left(q_A, q_B \right) = D_A(0) \left[1 - \left(q_A + \zeta q_B \right) / q_{m,A} \right] \tag{2.17a}$$

$$D_B \left(q_A, q_B \right) = D_B(0) \left[1 - \left(q_A + q_B \right) / q_{m,B} \right] \tag{2.17b}$$

This result is obtained for single file diffusion when one molecule cannot pass another resulting in a highly hindered counter-diffusion process. Figure 2.13 shows model predictions based on solid diffusion (eq. 2.11), the full Maxwell-Stefan (eq. 2.13) expression, single file diffusion (eq. 2.17) for the adsorption of Tg and BSA mixtures. The solid diffusion model poorly describes the transient uptake. The single file diffusion formulation more accurately describes the transient uptake but significantly overpredicts the BSA overshoot. The full Maxwell-Stefan expressions slightly overpredicts the initial BSA overshoot but show better relative agreement at long times.

In the case of Nuvia HR Q and Nuvia HP Q parallel pore and solid diffusion are likely to exist. Figures 2.1 and 2.2 show that the polymer-grafts in these resins do not fill the entire pore volume; therefore, pore diffusion can occur through the open pore space. Both Ma et al.[103] and Lenhoff et al. [104] report parallel pore and solid diffusion models. These models may mechanistically

describe protein adsorption for Nuvia HR and Nuvia Q. To adopt these models, additional batch kinetic measurements such as in Fig. 2.6 at both low and high protein concentrations are required to determine D_e and D_s. At low protein concentrations, solid diffusion is dominant while at high protein concentrations, pore diffusion dominates [104]. Thus, future work should include the additional batch uptake experiments necessary to determine these diffusivities.

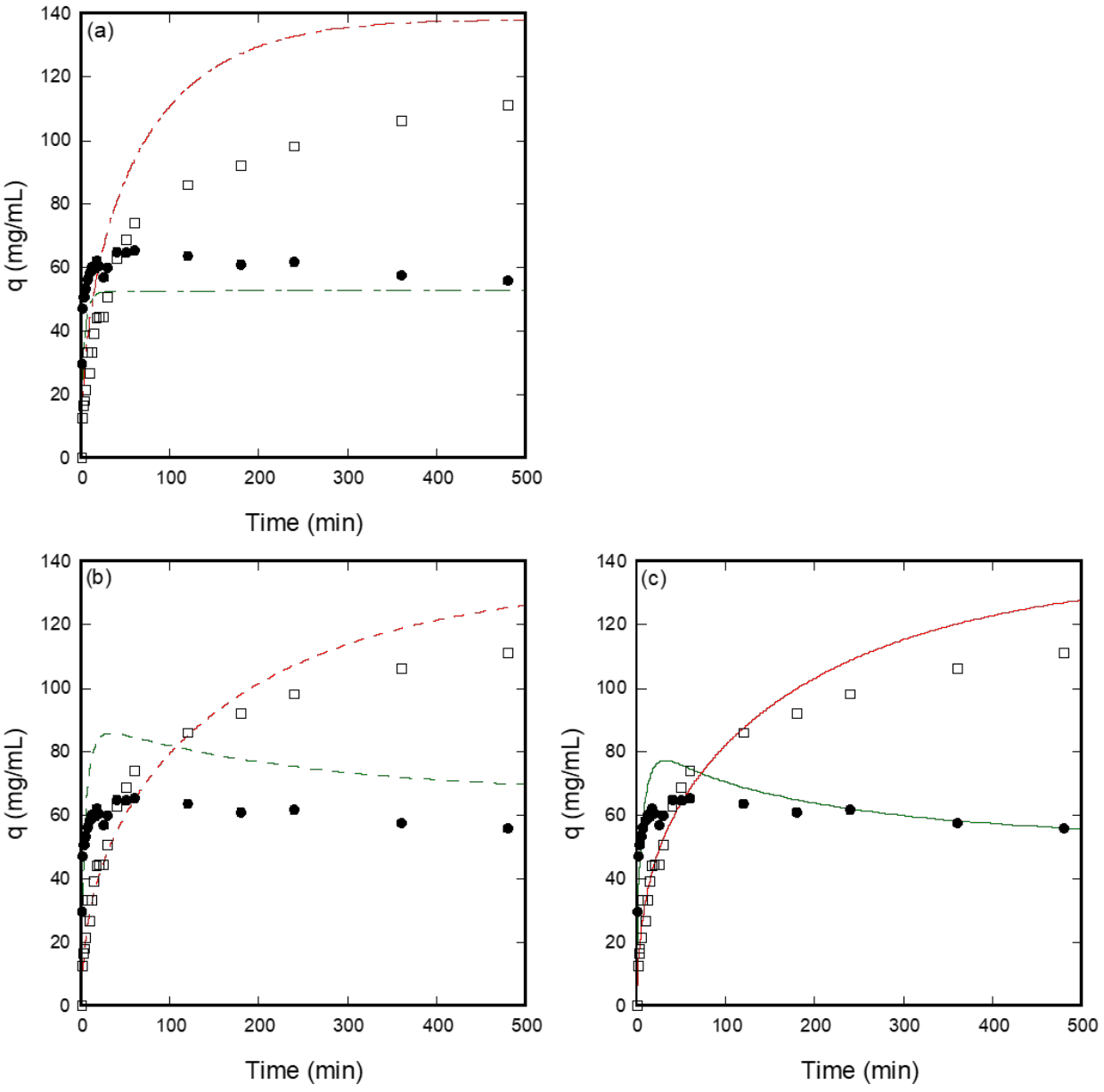

Figure 2.13: Coadsorption of Tg and BSA on Nuvia Q. Equilibrium described by eq.10. Lines are based on: (a) Solid diffusion model. (b) Single file diffusion. (c) Full Maxwell-Stefan model. C_0(Tg) = 1 mg/mL, C_0(BSA) = 1 mg/mL. D_s(BSA) = 4.8x10^{-9} cm^2/s & D_s(Tg) = 2.7x10^{-10} cm^2/s. Buffer: 20 mM BTP-HCl containing 50 mM NaCl at pH 7.0. (●) BSA (□) Tg.

2.5 Column behavior

In practical applications, chromatographic capture of target products or removal of impurities in a flow-through mode are conducted in packed columns. This section considers the dynamics of column adsorption for single and two-component systems.

2.5.1 Single-component column dynamics

Figure 2.14 shows the BSA breakthrough curves obtained for columns packed with each of the four AEX resins considered thus far: UNOSphere Diol Q, Nuvia HR Q, Nuvia Q, and Nuvia HP Q in BTP buffers at pH 7 containing different NaCl concentrations ranging from 0 mM to 100 mM. Sharp S-shaped curves are obtained in each case. Breakthrough occurs earlier with increasing NaCl concentrations as a result of the lower binding capacity observed at higher salt. Equilibrium and dynamic binding capacities abbreviated as EBC and DBC, respectively, calculated from these curves are shown in Table 2.7. In all four cases, at 0 mM and 50 mM NaCl, the EBC values are consistent with the isotherm measurements. Both EBC and DBC are much higher for the grafted resins than for the ungrafted UNOSphere Diol Q

Figure 2.16 shows the Tg breakthrough curves on the four AEX resins. In all four cases, the Tg curves are considerably shallower than those observed for BSA especially without added NaCl where the adsorption becomes very slow. Increasing the NaCl concentration to 50 mM sharpens the breakthrough curves for the grafted resins. As a result, even if the EBC is lower at 50 mM than without added salt, the DBC is greater. Conversely, for the ungrafted UNOSphere Diol Q resin, the DBC remains relatively constant.

As discussed in Section 2.4.1, at low NaCl concentrations, Tg binds strongly limiting mobility

Table 2.7: Summary of the DBC at 10% column breakthrough and DBC/EBC for the pure feed breakthrough of BSA and Tg shown in Figs. 2.14. and 2.16

		UNOSphere Diol Q		Nuvia HR Q		Nuvia Q		Nuvia HP Q	
	NaCl (mM)	DBC	$\frac{DBC}{EBC}$	DBC	$\frac{DBC}{EBC}$	DBC	$\frac{DBC}{EBC}$	DBC	$\frac{DBC}{EBC}$
BSA	0	27	0.84	86	0.92	150	0.93	91	0.94
	50	6	0.69	38	0.88	61	0.89	37	0.91
	100	1	0.60	13	0.83	18	0.73	12	0.92
Tg	0	14	0.23	17	0.40	24	0.23	22	0.40
	50	16	0.44	33	0.53	74	0.65	67	0.71
	100	15	0.43	74	0.85	138	0.82	75	0.84

DBC is in units of mg/mL column.

into the particles. The addition of NaCl to the mobile phase weakens Tg binding in the graft phase, increasing its mobility. This increase in Tg mobility is especially pronounced for Nuvia Q (Fig.2.16b) whose pores are completely filled with polymer-grafts. Alleviating this strong binding results in a higher DBC. Both Nuvia HR Q (Fig.2.16c) and Nuvia HP Q (Fig.2.16d) both high DBCs with no added NaCl likely because, their empty pore space allows for pore diffusion to occur parallel to transport in the graft phase. For Nuvia HR Q and Nuvia Q, early Tg breakthrough is observed for 0 mM NaCl since strongly bound Tg on the surface of these particles greatly increases the diffusional hindrance. However, the addition of NaCl alleviates the hindrance in the graft-phase, leading to a greater DBC. For Nuvia HR Q increasing NaCl from 50 to 100 mM resulted in later and sharper breakthrough. These experiments suggest that low to moderate concentrations of NaCl (0-100 mM) can be either induce rapidly adsorption or severely hinder large protein transport into these polymer-grafted resins.

Figures 2.15 and 2.17 show the breakthrough curves with model predictions for BSA (0 mM NaCl and 50 mM NaCl) and Tg (0 mM NaCl) using the pore diffusion model for UNOSphere Diol Q

Table 2.8: Summary of the EBC, q_m, and ϵ for the one-component breakthrough of BSA and Tg on each of the Nuvia resins shown in Figs. 2.14-2.16. Note that the ϵ varies because the columns were repacked in between breakthrough runs.

		UNOSphere Diol Q			Nuvia HR Q			Nuvia Q			Nuvia HP Q		
	NaCl (mM)	q_m	EBC	ϵ	q_m	EBC	ϵ	q_m	EBC	ϵ	q_m	EBC	ϵ
BSA	0	60	32	0.50	130	94	0.29	290	163	0.44	140	97	0.32
	50	21	9	0.41	75	43	0.45	124	69	0.47	72	41	0.45
Tg	50	60	35	0.40	150	62	0.54	190	112	0.46	150	94	0.42

EBC is in units of mg/mL column.

and the solid diffusion model for Nuvia HR Q, Nuvia Q, and Nuvia HP Q with parameters based on the batch uptake data. Both models assume that the isotherm is rectangular. The external mass transfer coefficient was estimated from the correlation of Wilson and Geankoplis [105]. The relevant expressions for the breakthrough curve are given by Weber and Chakraborti [106] or by eq. 8.80 in Carta and Jungbauer [28] for the pore diffusion model and by Yoshida et al. [107] for the solid diffusion model. The values of q_m, D_e for the pore diffusion model, and D_s for the solid diffusion model used for these calculations were those obtained from the batch uptake curves as described in Section 2.4.1. The only parameter fitted in each case was the column extraparticle porosity, ϵ,which could not be determined accurately from pressure drop data for the short columns used in these experiments. In this case, the values of ϵ were determined by matching the equilibrium binding capacities measured after 24 h of contact with those calculated by material balance from the breakthrough curves. These values are summarized in Table 2.8.

As seen in Fig. 2.15, the respective models show good agreement with the experimental breakthrough curves except in the very early and late portions of the curves. Both of these portions are affected by packing quality as discussed by Roberts and Carta [108]. As seen in Fig. 2.17, while not perfect, the respective models capture the experimental trends observed for Tg adsorption on the four resins with

the largest deviations between predicted and experimental results occurring for long times near the saturation limit. It is probable that hindered diffusion effects and/or the existence of a distribution of pore sizes, which are not described by the simple models used in this work, become dominant in this limit. Interestingly, the agreement between model and experimental result is best for Nuvia Q (Fig. 2.17b). It is probable that the better agreement for this resin stems from the fact that due to the higher grafted polymer content and the near absence of macropores in this material, the solid diffusion model is actually a mechanistically correct description of transport. This is not likely to be the case for the low polymer-grafted resins, which contain a significant amount of large pores, and where protein transport is likely a combination of pore and solid diffusion that is not captured by the model used.

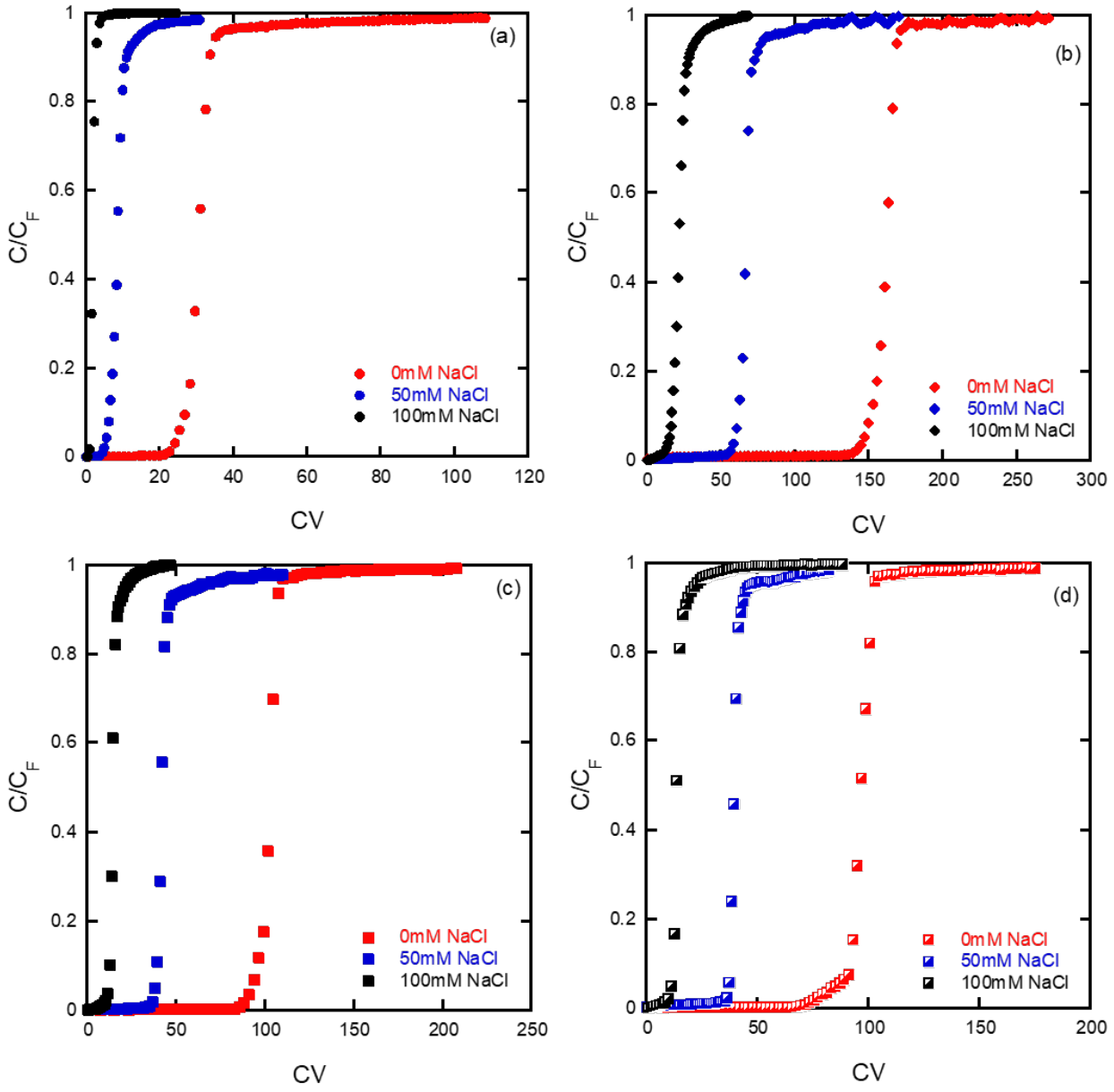

Figure 2.14: Breakthrough of BSA on (a) UNOsphere Diol Q, (b) Nuvia Q, (c) Nuvia HR Q, and (d) Nuvia HP Q. Residence time = 2 min. Buffer: 20 mM BTP-HCl at pH 7.0 with different NaCl concentrations. $C_F = 1$ mg/mL.

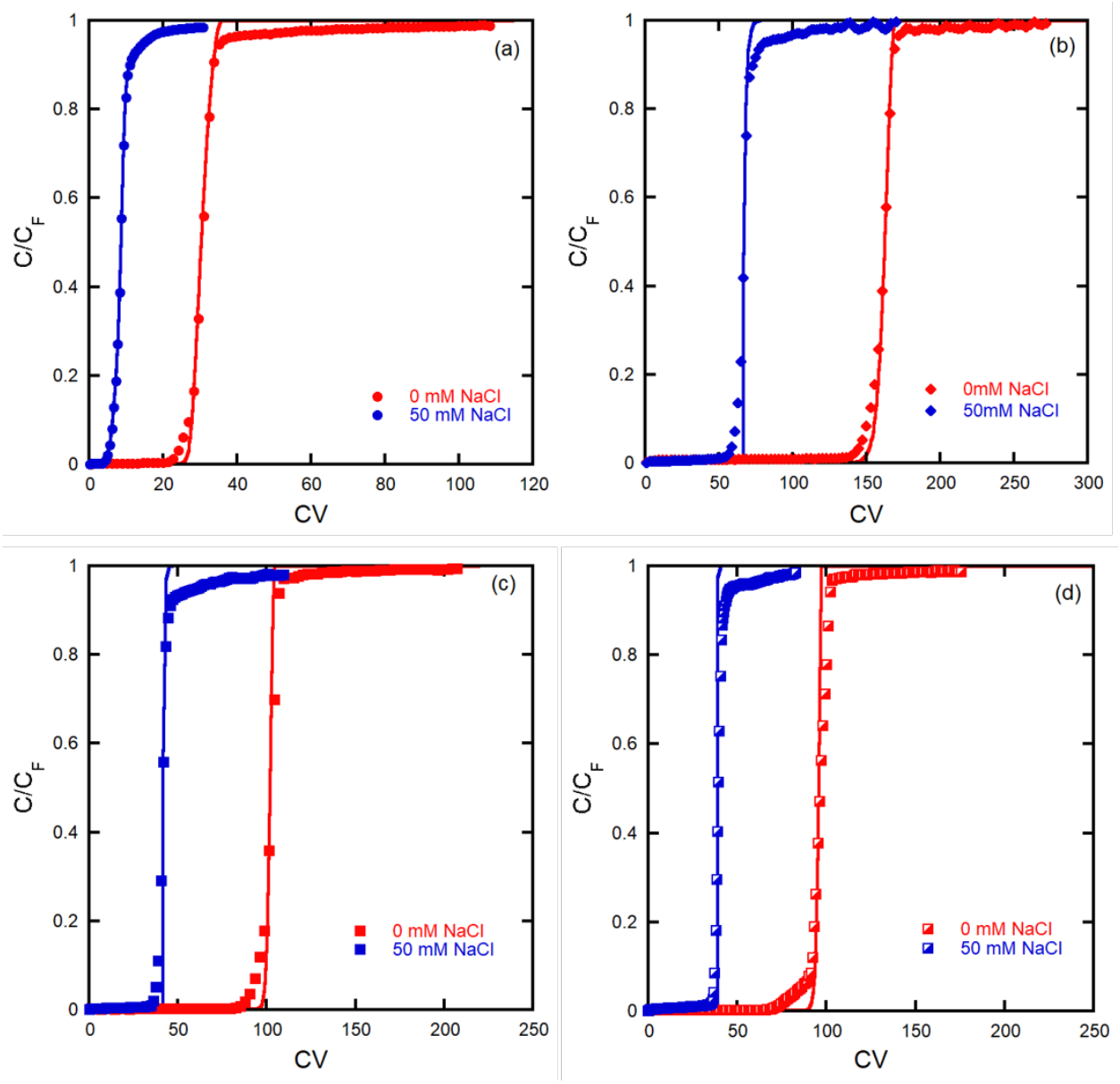

Figure 2.15: Breakthrough of BSA on (a) UNOsphere Diol Q, (b) Nuvia Q, (c) Nuvia HR Q, and (d) Nuvia HP Q. Residence time = 2 min. Buffer: 20 mM BTP-HCl at pH 7.0 with different NaCl concentrations. C_F = 1 mg/mL. Lines are based on the pore diffusion model in (a) and the solid diffusion model in (b),(c), and (d).

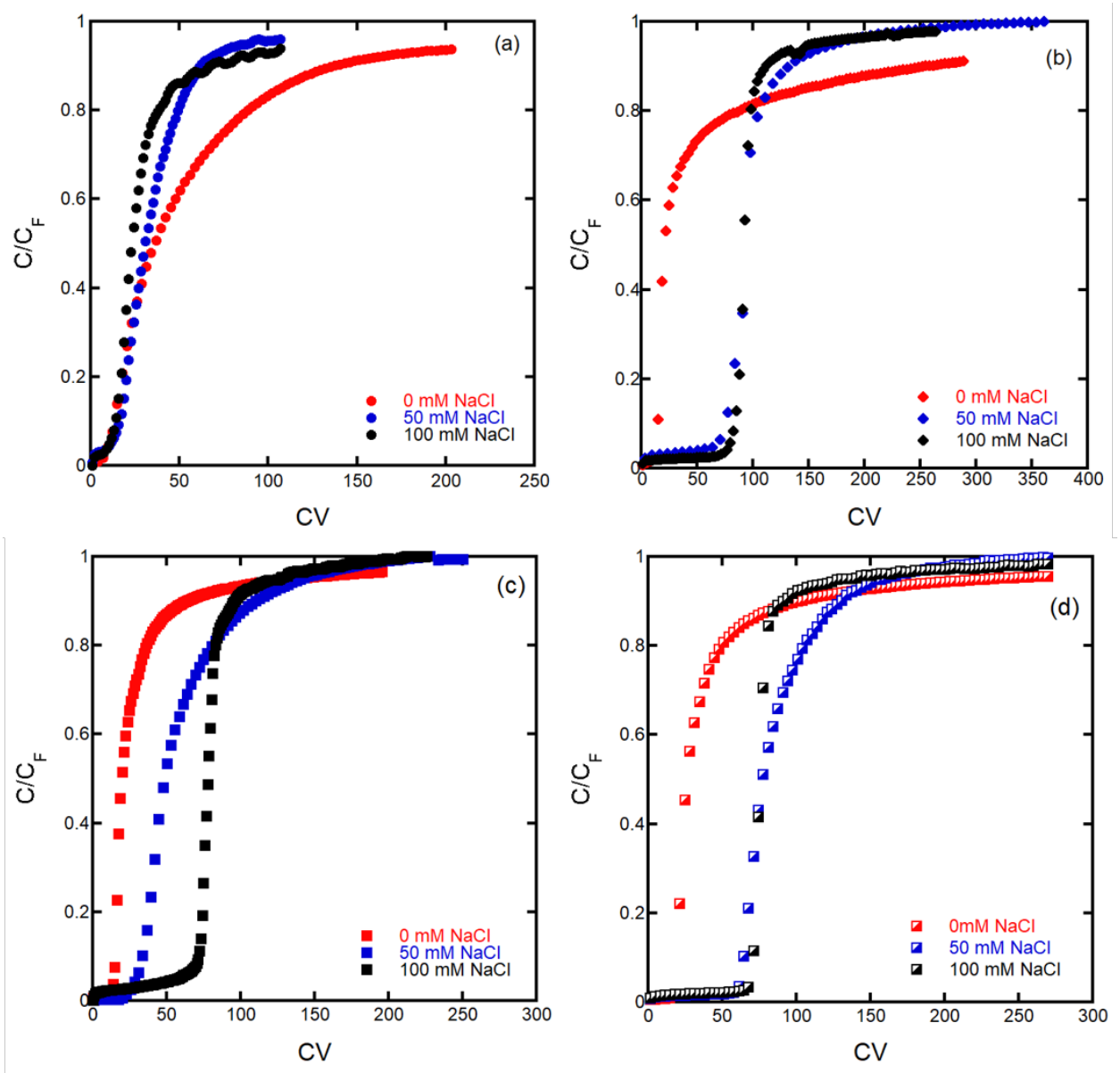

Figure 2.16: Breakthrough of Tg on (a) UNOsphere Diol Q, (b) Nuvia Q, (c) Nuvia HR Q, and (d) Nuvia HP Q. Residence time = 2 min. Buffer: 20 mM BTP-HCl at pH 7.0 with different NaCl concentrations. $C_F = 1$ mg/mL.

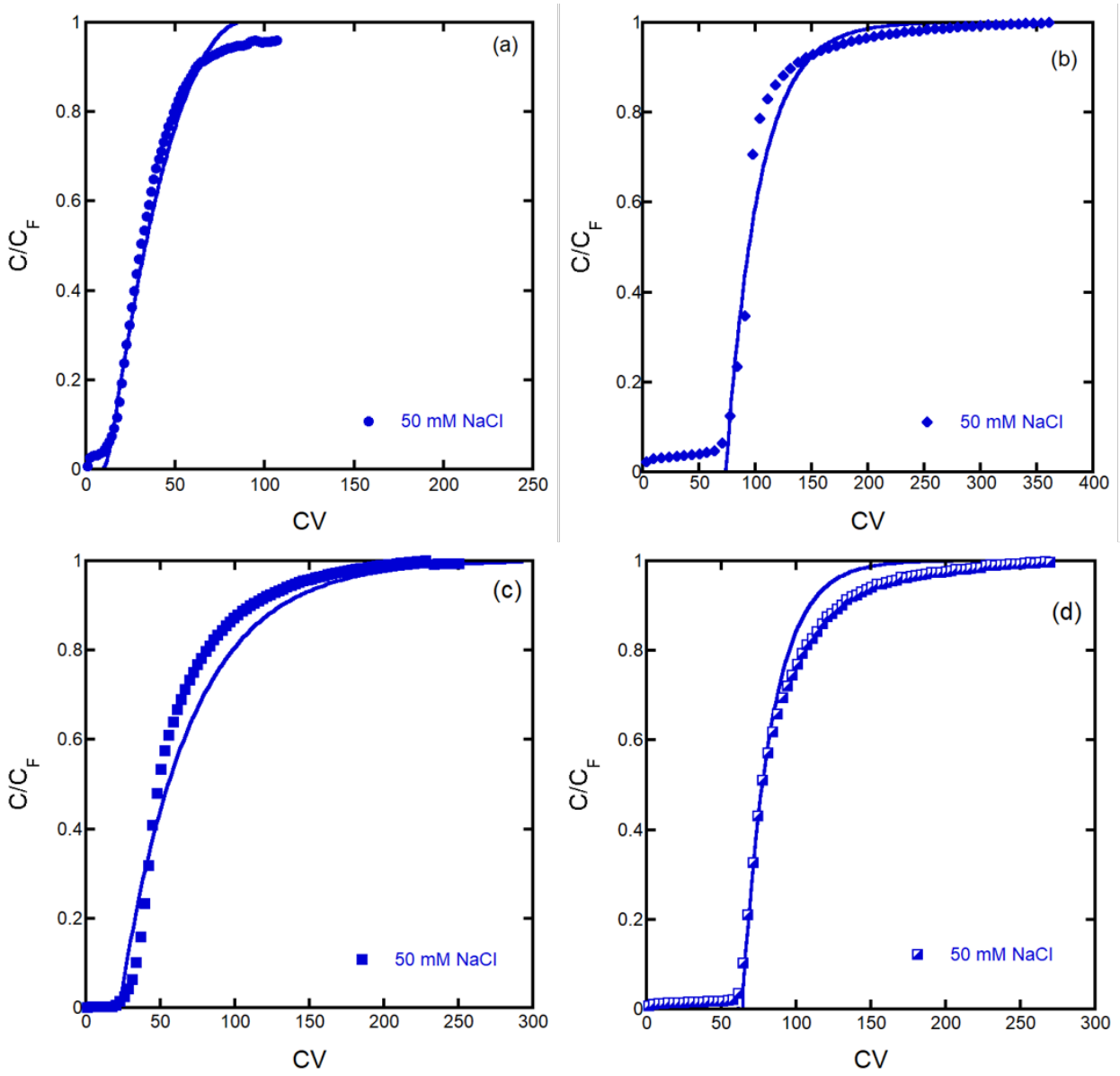

Figure 2.17: Breakthrough of Tg on (a) UNOsphere Diol Q, (b) Nuvia Q, (c) Nuvia HR Q, and (d) Nuvia HP Q. Residence time = 2 min. Buffer: 20 mM BTP-HCl at pH 7.0 with 50 mM NaCl. C_F = 1 mg/mL. Lines are based on the pore diffusion model in (a) and the solid diffusion model in (b),(c), and (d).

2.5.2 Two-component column dynamics

Figure 2.18 shows the two-component breakthrough curves for BSA-Tg mixtures in BTP buffer at pH 7 containing 50 mM NaCl. The results obtained for UNOSphere Diol Q show a substantial separation of the BSA and Tg curves indicating that Tg is largely preferred by the resin for these conditions. BSA overshoots the feed concentration indicating that it is displaced by Tg. Nuvia HP Q shows even better separation of the BSA and Tg curves with a more pronounced overshoot of BSA consistent with faster kinetics. Finally, Nuvia Q shows minimal separation of the BSA and Tg curve with almost no overshoot of BSA indicating that while binding capacity is high for this resin, as in indicated by the later breakthrough of BSA, the displacement kinetics of BSA by Tg is very slow.

Predictions of the column behavior require coupling of the relevant rate expressions, discussed in Sections 2.4.1 and 2.4.2, with differential material balances for the column. Assuming plug flow with negligible axial dispersion, the latter are given by:

$$u\frac{\partial C_i}{\partial x} + \epsilon\frac{\partial C_i}{\partial t} + (1-\epsilon)\frac{\langle \hat{q}_i \rangle}{\partial t} = 0 \tag{2.18a}$$

$$C_i(0,t) = C_{i,F} \tag{2.18b}$$

$$C_i(x,0) = C_i^0 \tag{2.18c}$$

Where ϵ is the extraparticle porosity, C_i is the fluid phase concentration, u is the superficial velocity, and $C_{i,F}$ is the feed concentration. The particle-average adsorbed phase concentration $\langle \hat{q}_i \rangle$ is related

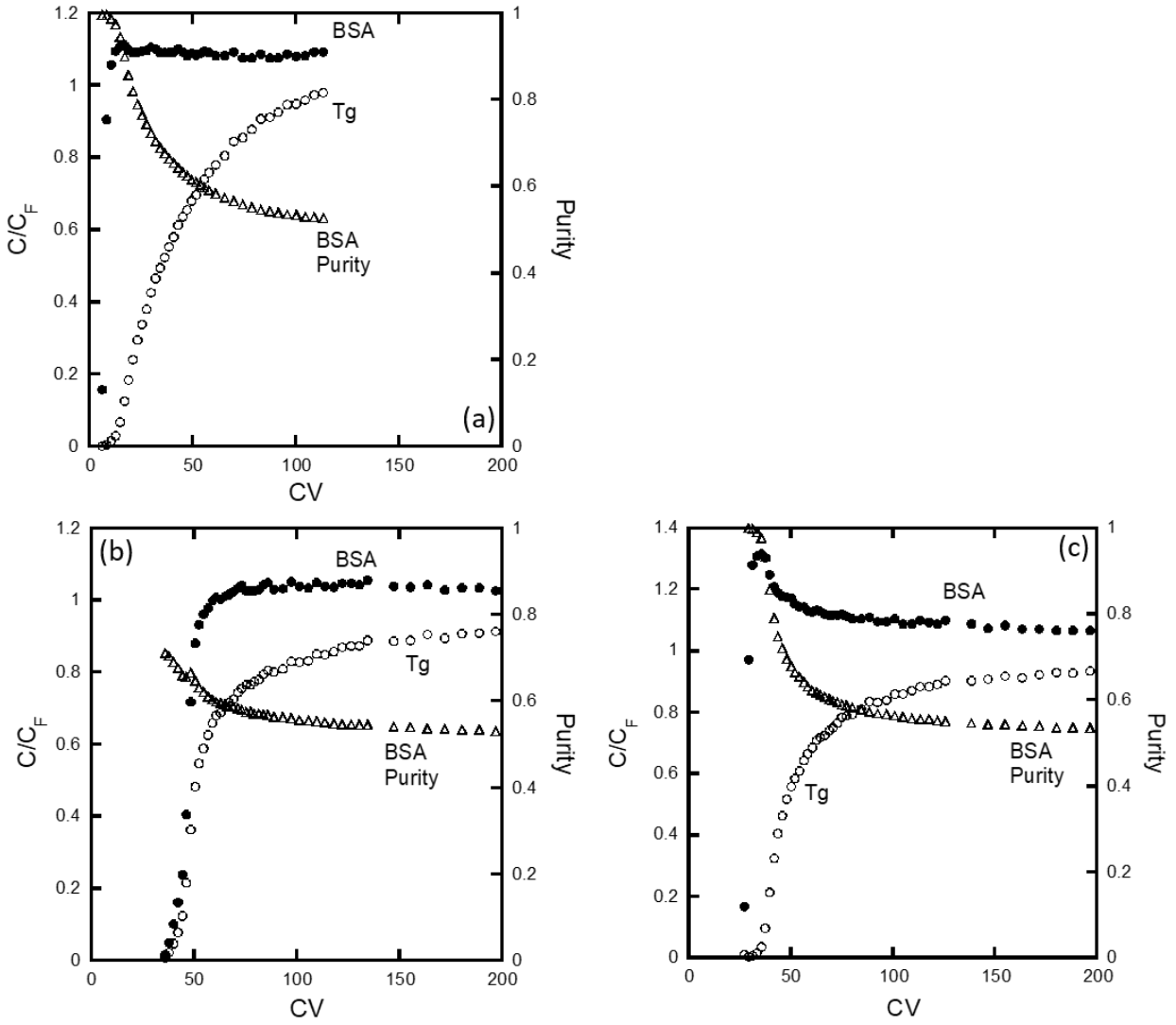

Figure 2.18: Two-component breakthrough curves for BSA/Tg mixtures containing 1 mg/mL of each protein in 20 mM BTP-HCl with 50 mM NaCl at pH 7 on (a) UNOSphere Diol Q, (b) Nuvia Q, and (c) Nuvia HP Q. Residence time = 2 min. Closed symbols = BSA, Open symbols = Tg. $\diamond$ = BSA purity.

to the flux at the particle surface, $J_i\Big|_{r=r_p}$ by:

$$\frac{\partial \langle \hat{q}_i \rangle}{\partial t} = -\frac{3}{r_p} J_i\Big|_{r=r_p} \tag{2.19}$$

As shown in Section 2.4.1, since transport occurs by pore diffusion in UNOSphere Diol Q and by the single file diffusion mechanism in Nuvia Q, different expressions for the flux are needed for each. For UNOSphere Diol Q we have:

$$\epsilon_p \frac{\partial c_{BSA}}{\partial t} + \frac{\partial q_{BSA}}{\partial t} = \frac{D_{e,BSA}}{r^2} \frac{\partial}{\partial r} \left(r^2 \frac{\partial c_{BSA}}{\partial r} \right) \tag{2.20a}$$

$$\epsilon_p \frac{\partial c_{Tg}}{\partial t} + \frac{\partial q_{Tg}}{\partial t} = \frac{D_{e,Tg}}{r^2} \frac{\partial}{\partial r} \left(r^2 \frac{\partial c_{Tg}}{\partial r} \right) \tag{2.20b}$$

$$\frac{\partial c_{BSA}}{\partial r}\Big|_{r=0} = 0, \quad \frac{\partial c_{Tg}}{\partial r}\Big|_{r=0} = 0 \tag{2.20c}$$

$$D_{e,BSA} \frac{\partial c_{BSA}}{\partial r}\Big|_{r=r_p} = k_{f,BSA} \left(C_{BSA} - c_{BSA}\Big|_{r=r_p} \right), \quad D_{e,Tg} \frac{\partial c_{Tg}}{\partial r}\Big|_{r=r_p} = k_{f,Tg} \left(C_{Tg} - c_{Tg}\Big|_{r=r_p} \right) \tag{2.20d}$$

For Nuvia Q, we have:

$$\frac{\partial q_{BSA}}{\partial t} = \frac{1}{r^2} \frac{\partial}{\partial r} \left(r^2 D_{s,BSA} \left[\left(1 - \zeta \frac{q_{Tg}}{q_{m,BSA}} \right) \nabla q_{BSA} + \zeta \frac{q_{BSA}}{q_{m,Tg}} \nabla q_{Tg} \right] \frac{\partial q_{BSA}}{\partial r} \right) \tag{2.21a}$$

$$\frac{\partial q_{Tg}}{\partial t} = \frac{1}{r^2} \frac{\partial}{\partial r} \left(r^2 D_{s,Tg} \left[\frac{q_{Tg}}{q_{m,BSA}} \nabla q_{BSA} + \left(1 - \frac{q_{BSA}}{q_{m,Tg}} \right) \nabla q_{Tg} \right] \frac{\partial q_{Tg}}{\partial r} \right) \tag{2.21b}$$

$$\frac{\partial q_{BSA}}{\partial r}\Big|_{r=0} = 0, \quad \frac{\partial q_{Tg}}{\partial r}\Big|_{r=0} = 0 \tag{2.21c}$$

$$q_{BSA}\Big|_{r=r_p} = q^*_{BSA} \left(C_{BSA}, C_{Tg} \right), \quad q_{Tg}\Big|_{r=r_p} = q^*_{Tg} \left(C_{BSA}, C_{Tg} \right) \tag{2.21d}$$

Exact modeling of Nuvia HP Q would require expressions accounting for parallel pore and solid

diffusion since the pores of this support matrix are only partially occupied by the dextran grafts. For simplicity, we neglected solid phase transport and assume that pore diffusion is dominant. Thus, in this case, the equations describing Nuvia HP Q are the same as those describing UNOSphere Diol Q.

Figure 2.19 shows model predictions for UNOSphere Diol Q, Nuvia Q, and Nuvia HP Q compared to experimental results. As seen in this figure, there is good agreement between the pore diffusion model and the UNOSphere Diol Q (Fig. 2.19a) data and between the Maxwell-Stefan single file diffusion model and the Nuvia Q (Fig. 2.19b) data. Agreement of the pore diffusion model with Nuvia HP Q (Fig. 2.19c) data is, however, only approximate since transport in this resin is a combination of pore and solid-phase diffusion mechanisms. In this case, pore diffusion captures the point of BSA and Tg breakthrough but fails with the breakthrough shape. Pore diffusion alone simply cannot describe the contribution to transport provided by the polymer-grafts. Pore diffusion predicts a better separation than observed. Since the isotherm (Fig. 2.9c-d) is rectangular pore diffusion predicts sharp adsorption profiles and fast displacement similar to that observed for UNOSphere Diol Q; however the diffusivities from batch uptake measurements (Fig. 2.6) incorporate enhanced transport from solid diffusion. Thus, using a lumped diffusivity results in simulated adsorption faster pore diffusion and better separation. Most likely, the contribution from a solid diffusion mechanism results in enhanced adsorption kinetics, but not instantaneous displacement of BSA by Tg.

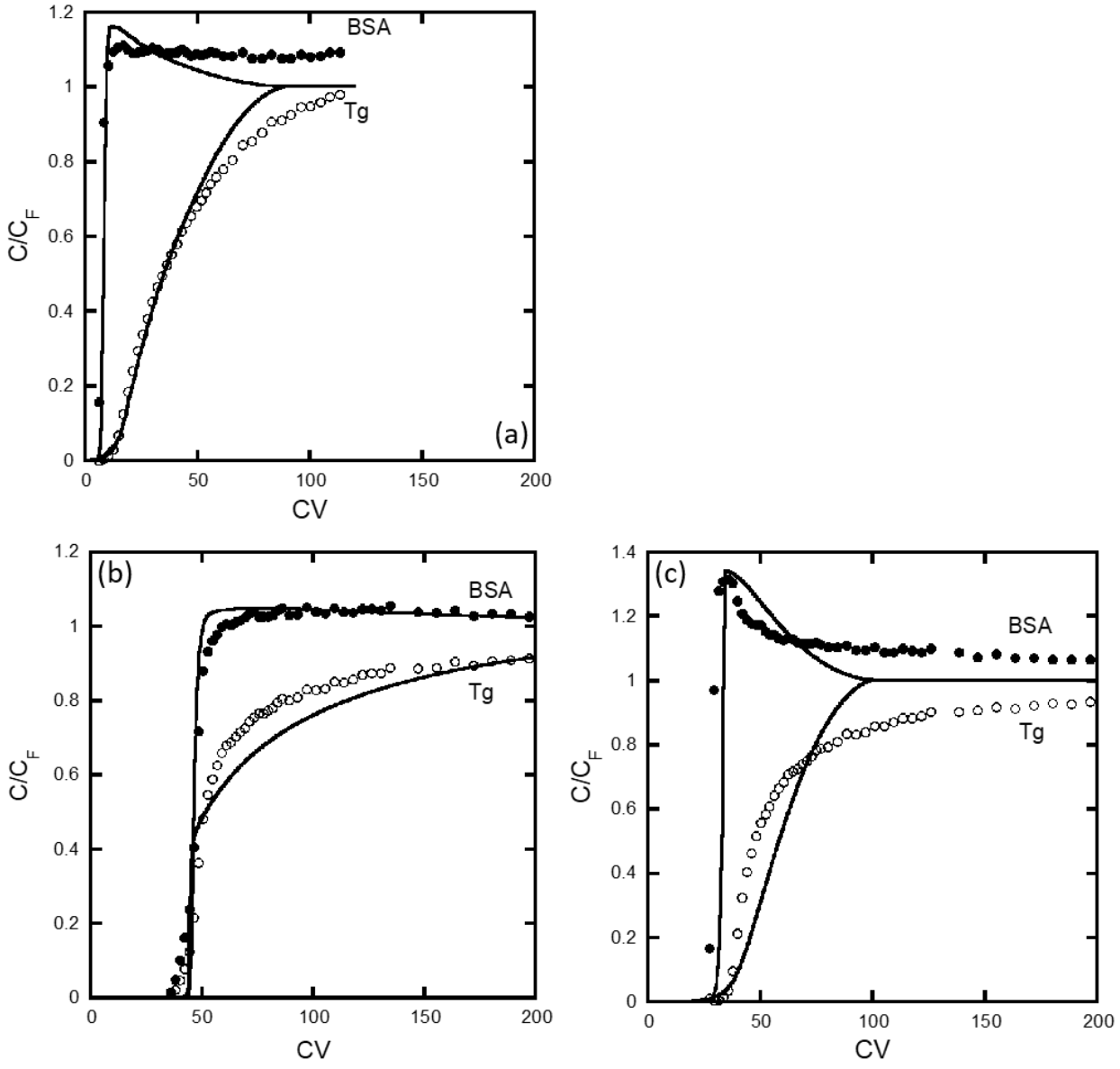

Figure 2.19: Comparison of model predictions and two-component experimental breakthrough curves for BSA/Tg mixtures. Breakthrough curves are the same as shown in Fig. 2.18. (a) pore diffusion (eq. 2.5) with equilibrium described by 2.12; (b) single file diffusion (eq. 2.17) with equilibrium described by eq. 2.10, (c) pore diffusion with equilibrium described by eq. 2.10. Closed symbols = BSA, Open symbols = Tg.

Chapter 3 Agarose-encapsulated adsorbents

3.1 Introduction

The objective of the work described in this chapter is to develop and characterize a composite chromatographic medium comprising CHT particles encapsulated in inert agarose beads. Agarose is a hydrophilic polysaccharide that forms gels with tunable pore size. It is often used as the base matrix for chromatography resins because of the ease with which it can be produced in bead form, crosslinked, and functionalized and because of its inert character that prevents non-specific binding. Various commercial resins including Sepharose and Capto from Cytiva (Marlborough, MA, USA) and Praesto from Purolite Life Sciences (King of Prussia, PA, USA) are based on agarose and are used extensively with a variety of ligands [23].

Agarose has also been used previously to entrap hydroxyapatite microcrystals and a commercial product based on this approach is currently available with trade name HA Ultrogel® [109]. In this material, hydroxyapatite microcrystals are dispersed throughout the agarose. The binding capacity of this material for bovine serum albumin (BSA) has been reported to be less than 7 mg/mL and the size exclusion limit has been reported to be greater than 5,000 kDa [109]. Thus, because of the large size exclusion limit, it is evident that this composite material was not designed for the exclusion of large molecules, but mainly to support and stabilize the entrapped hydroxyapatite microcrystals. Fargues et al. [110] have studied the adsorption of BSA and hemoglobin on this material. The BSA binding capacity was reported to be near zero at pH 7.5 increasing to about 10 mg per g of dry gel at pH 6.8 and to about 65 mg per g of dry gel at pH 5.7. Based on their reported value of the dry gel content of packed columns (0.16 ± 0.01 g dry gel/mL), these BSA capacity values correspond 1.6 and 10 mg/mL at pH 6.8 and 5.7, respectively. While the capacity reported increases at lower pH, hydroxyapatite is known to be unstable in solutions at pH below about 6.5 where it dissolves rapidly [111]. Thus, operation at pH 5.7 is likely to be impractical. A higher capacity around 17

mg/mL was reported for hemoglobin at pH 6.7, indicating that this material may be better suited for the adsorption of cationic proteins.

In our approach, instead of encapsulating hydroxyapatite crystals, we encapsulate whole CHT particles. As a result, we preserve the macroporous structure of the CHT particles while introducing the size exclusion properties of the inert agarose. CHT is a stationary phase consisting of hydroxyapatite nanocrystals and has demonstrated suitability for process scale protein chromatography applications [56]. Thus, understanding the adsorption characteristics of acidic proteins is required to properly evaluated our novel composite particles.

HAP has been extensively studied for a variety of applications including, the removal of aggregates in monoclonal antibody purification [112][113], the separation of antibody charge variants [114], and the purification of mAbs from cell culture supernatant [115]. Examples of separations involving non-antibody species include purification of RNA and DNA [116], isolation of plasmid DNA [117], and the purification of human papillomavirus virus-like particles [58]. CHT excels at binding host cell proteins and nucleic acids, such as RNA, that are of particular concern when non-secreted biotherapeutics are expressed in cells [118]. Figure 3.1 shows the adsorption of fluorescently labeled RNA and fluorescently labeled Human Papillomavirus-VLP (HPV-VLP) saturated CHT particles. After 4 hours, the HPV-VLPs are only bound to the surface of CHT, suggesting that the HPV-VLPs are too big to diffuse deeply into the CHT pores. Despite the presence of HPV-VLPs on the surface, RNA diffuses quickly into the particles and does not appear to displace HPV-VLPs at the particle surface. Wang [119] investigated the adsorption and desorption of HPV-VLPs on CHT and concluded that at significant sodium phosphate concentrations ($\leq$ 250 mM) HPV-VLPs were strongly bound. According to Cook et al. [58] CHT is used in the purification of Gardasil, a HPV-VLP based vaccine produced by Merck. Preventing the adsorption of large biomolecules to the surface of CHT can improve VLP recovery.

Despite extensive use of hydroxyapatite, few investigators have characterized protein adsorption equilibrium and kinetics with models that provide a mechanistic understanding for chromatographic applications. Giovannini and Freitag [116] correlated binding capacities for a variety of CHT types with chromatographic performance. Jungbauer et al. [120] reported IgG adsorption on "nanophased" HAP particles and showed that for small nanophased HAP particles could eliminate pore diffusion resistance.

The most comprehensive investigation of protein adsorption on CHT type-I and CHT type-II is given by Wang and Carta [61][62][63]. These authors investigated mAb monomer-dimer adsorption using batch measurements and CLSM [61]. It was shown that mAb monomer-dimer adsorption on CHT is accurately described by the Langmuir isotherm and that the adsorption kinetics is described by pore diffusion [62]. Together, these models excellently predicted monomer-dimer separations both by frontal chromatography and by gradient elution at high protein loads [63].

Much less is known about the adsorption behavior of acidic proteins on CHT particularly in mixtures. In this work we first characterize the adsorption of acidic proteins on CHT using BSA and Tg as model proteins both individually and in mixtures. Single component and two-component adsorption equilibrium and kinetics of BSA and Tg adsorption on CHT are investigated. The models presented by Wang and Carta [61][62][63] extended to BSA and Tg. Methodologies previously discussed in Chapter 2 are adapted to the single component and two-component adsorption of BSA and Tg on CHT with appropriate modification. We then develop a method to encapsulate CHT.

Encapsulation is obtained via an emulsification method wherein the CHT particles are first mixed in a heated agarose solution which is then emulsified in a hot organic solvent creating a droplet phase consisting of agarose and CHT. Upon cooling, the agarose droplets gels forming agarose-CHT composite beads, which are then crosslinked to improve stability and flow properties. This

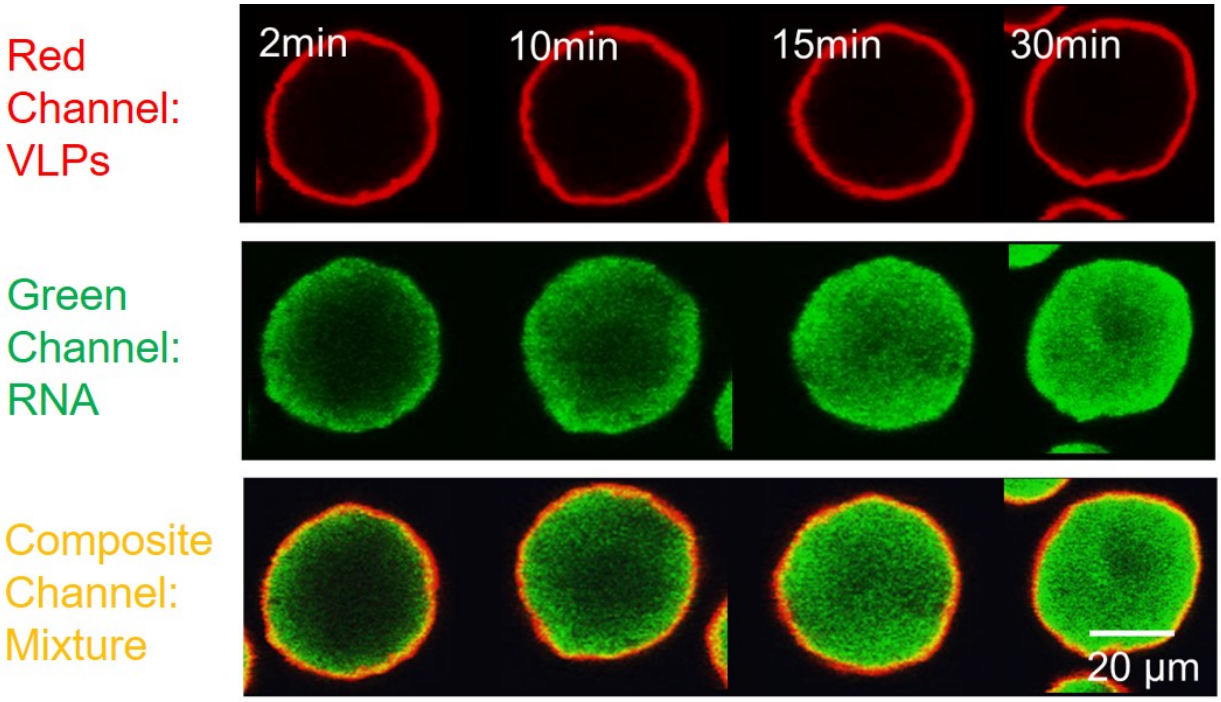

Figure 3.1: Sequential adsorption of RNA at 2 mg/mL on CHT pre-saturated with VLP at 0.2 mg/mL for 4 hours. Buffer: 5 mM Na_2PO_4 containing 250 mM NaCl at pH 7.0. CLSM images adapted from [119].

preparation method was chosen to allow for independent control over the agarose concentration and CHT type and content.

Encapsulating CHT particles inside agarose beads creates a composite material with complementary separation mechanisms: separation by molecular size and shape, resulting from the tunable agarose structure, and adsorption occurring within the encapsulated CHT particles. Combination of these mechanisms results in an adsorbent ideally suited for flow-through separations of large proteins and bioparticles such as viruses, virus-like particles, and large vaccine molecules. Importantly, the agarose prevents surface binding of these bioparticles that may otherwise occur on unencapsulated CHT particles.

The composite beads are prepared under a range of shearing rates, surfactant concentrations, CHT concentrations, and agarose concentrations to determine what conditions produce materials suitable for chromatographic applications. Light microscopy, inverse size exclusion chromatography, and density measurements are used to characterize their structure. Static and dynamic binding capacity measurements are used to determine their functional properties using RNA, BSA, Tg, IgM, and 30 and 50 nm silica nanoparticles as models for protein impurities and bioparticles. Confocal laser scanning microscopy was used to determine the location of bound species within the composite particles and the kinetics of binding of RNA and BSA.

3.2 Adsorption properties of unencapsulated CHT

3.2.1 Materials and methods

The proteins used in this work are purified BSA and stock bovine Tg obtained from MilliporeSigma (St. Louis, MO, USA). Disodium phosphate and monosodium phosphate were purchased from

MilliporeSigma. The CHT type-I material used in this work was provided by BioRad Laboratories (Hercules, CA, USA) and is the same as that used by Wang and Carta [61]. The relevant physical properties are summarized in Table 3.1.

The experimental procedures used were the same as those described in Chapter 2. CLSM was done in a similar fashion as described in Section 2.2.2. Rhodamine Red-X and Rhodamine Green-X fluorescent dyes were conjugated to Tg and BSA, respectively, by reaction with primary amine residues followed by removal of excess dye as described in Section 2.2.2. The final molar ratios of labeled to unlabeled protein were 0.16 and 0.29 for Tg and BSA, respectively. All CLSM experiments were performed by diluting the conjugated protein with unconjugated protein to obtain a final ratio of 1:40 labeled protein to unlabeled protein. The images were taken with a Zeiss LSM 510 microscope using a Plan Apochromat 63x/1.4 NA oil objective. Resin samples were placed in protein solutions in 15 mL falcon tubes rotated end-over-end and at various time-intervals small samples ($\leq$ 150 μL) were withdrawn and sieved in micro-centrifuge tubes using a Minispin bench-top centrifuge operated at 13,400 rpm for 30-45 sec. The particles recovered were resuspended in benzyl alcohol which matches the refractive index of CHT and then imaged [61].

Height equivalent theoretical plate (HETP) measurements for nonbinding conditions were made for BSA and Tg using an AKTA^{TM} Pure 25 system (Cytiva, Marlborough, MA, USA) with UV detection at 280 nm. For this purpose, CHT particles were packed into 1 cm inner diameter Tricorn 10/100 columns (obtained from Cytiva, Marlborough, MA, USA) to a bed height of 8.5 cm. The final bed volume was $V_c = 6.6 \pm 0.2$ mL the packing quality was determined from acetone pulse injections which gave asymmetry factor of 1.1 and a reduced HETP ($h = HETP/d_p$ of 3.9. For this proteins, the HETP was determined by injecting 100 μL pulse injections of 3 mg/mL BSA or 2 mg/mL Tg at flow rates ranging from 0.5 mL/min to 4 mL/min in a mobile phase containing 505 mM $NaHPO_4$ and 250 mM NaCl at pH 7. For those conditions, no binding of either protein

occurs. The effective pore diffusivity, D_e, of each protein was then determined from the slope of the reduced HETP curve according to the following equation [121]

$$\frac{D_e}{D_0} = \frac{1}{30}\frac{\epsilon}{1-\epsilon}\left(\frac{k'}{1+k'}\right)^2\left(\frac{dh}{dv'}\right)^{-1} \tag{3.1}$$

Where D_0 is the protein free solution diffusivity (See Table 2.1), $k' = (1-\epsilon)K_c/\epsilon$ is the protein retention factor, $h = HETP/d_p$, and $v' = vd_p/D_0$ is the reduced velocity with $v = u/\epsilon$ being the interstitial velocity.

Column breakthrough experiments were obtained for one-component feeds containing either BSA or Tg and for a two-component feed mixture of BSA and Tg with a 0.5 cm diameter Tricorn 5/5 column (Cytiva, Marlborough, MA, USA) packed to a bed height of 2.3 cm. These experiments were performed on the same system as the HETP measurements at a residence times of 2 min or 5 min, corresponding to flow rates of 0.1 and 0.23 mL/min, respectively. As described in section 2.2.2, in addition UV monitoring at 280 nm, fractions were taken every 1 CV and analyzed by UPLC-SEC to determine the different composition.

Table 3.1: Properties of the CHT type-I particles used in this work. Values from [61]

Property	Value
Mean bead diameter, d_p (µm)	41
Skeletal density (g/mL)	3.1
Hydrated bead density (g/mL)	1.6
Intraparticle porosity, ϵ_p	0.73
Pore radius, r_{pore} (nm)	30

3.2.2 Adsorption equilibrium and kinetics

As discussed by Gorbunoff et al. [55] [54] [122] proteins interact with CHT in different ways depending on their properties. Acidic proteins interact primarily with the calcium groups on the

CHT surface. In this case, displacing salts, such as phosphate, that also interact with the calcium groups can be used to modulate protein binding. Typically acidic proteins will bind at low phosphate concentrations and desorb at high phosphate concentrations. Since the CHT surface contains negatively charged phosphate groups added NaCl is often needed to promote binding by screening repulsive interactions. Figure 3.2 shows the one-component adsorption isotherms in this work for BSA and Tg at different NaCl and phosphate concentrations.

In the case of BSA, binding in 5 mM $NaHPO_4$ is relatively independent on NaCl concentration (Fig. 3.2a) with a slight maximum capacity at 250 mM NaCl ($q_m = 44.5$ mg/mL and $K_L = 5.5$ mL/mg). The effect of $NaHPO_4$ (Fig. 3.2c) is much more pronounced with almost no binding in 150 mM $NaHPO_4$. The trends for Tg (Fig. 3.2b, d) with regards to the effects of NaCl and $NaHPO_4$ concentrations are similar for those observed for BSA. However, the maximum binding capacity of Tg is about two times that of BSA ($q_m = 85.7$ mg/mL and $K_L = 8.5$ mL/mg). The trends observed for BSA and Tg are consistent with binding to the C-sites via a complexation mechanism.

Figure 3.3 shows two-component adsorption of BSA/Tg mixtures in 250 mM NaCl containing 5, 20, 25, and 50 mM $NaHPO_4$ at pH 7. Preferential binding of Tg relative to BSA at low phosphate concentrations (i.e., 5 mM) is evident by the larger relative drop off of q_{BSA} along the C_{Tg}-axis in Fig. 3.3a, compared to the shallower drop off of q_{Tg} along the C_{BSA}-axis in Fig. 3.3b. Each surface was generated by fitting the single and two-component equilibrium adsorption data to the discount factor adsorption (eq. 2.10) with the best fit parameters shown in Table 3.2. As seen in Fig. 3.3 The two-component results are in agreement with the isotherm model.

Figure 3.5 shows the representative CLSM images for the one-component adsorption of BSA and Tg in 5 mM $NaHPO_4$ with 250 mM NaCl, which corresponds to the maximum adsorption capacities for these two proteins. The evolution of the broad protein concentration profiles is qualitatively the

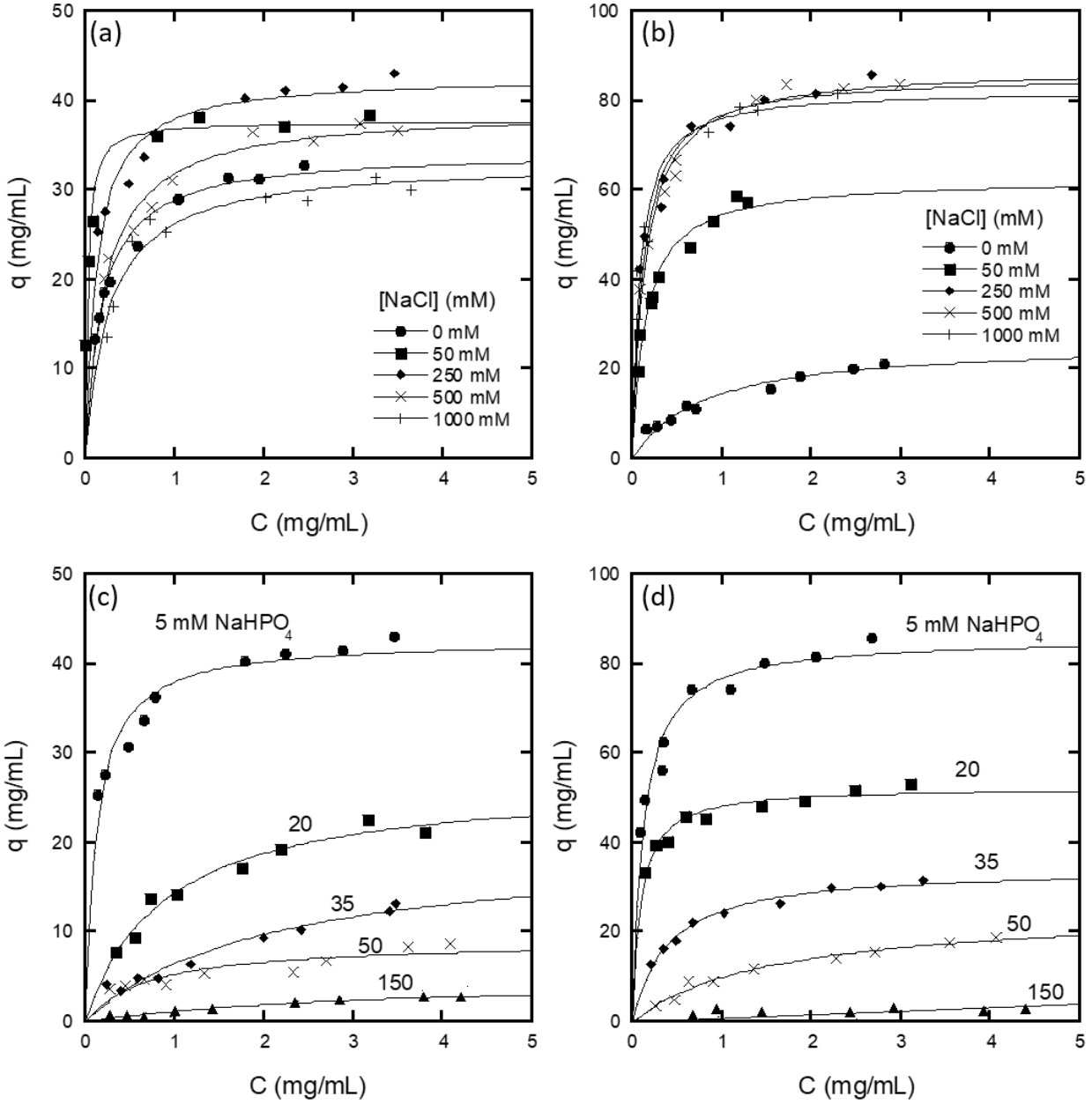

Figure 3.2: One-component adsorption isotherms for BSA (a,c) and for Tg (b,d) on CHT type-I at pH 7. (a) and (b) show the effects of NaCl in 5 mM $NaHPO_4$ (c) and (d) show the effect of $NaHPO_4$ with 250 mM NaCl.

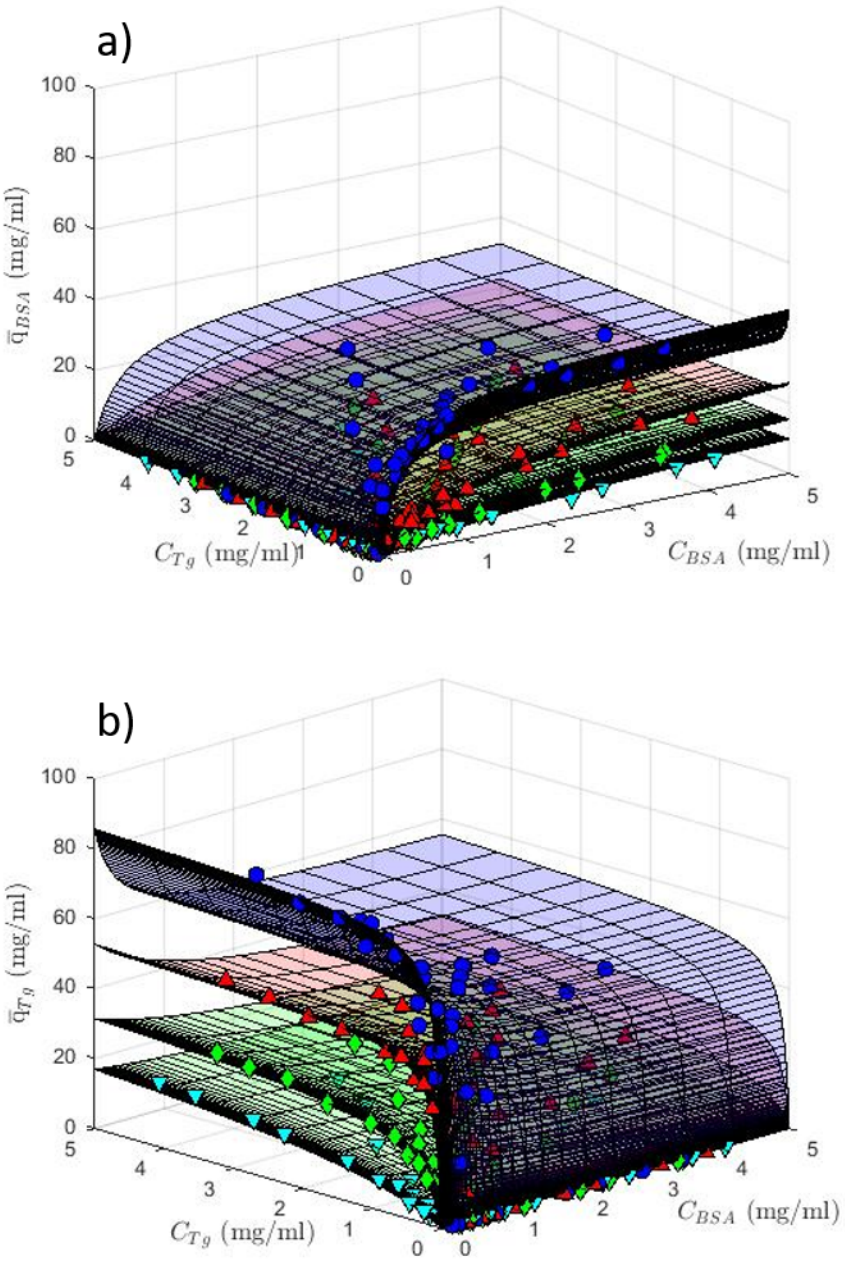

Figure 3.3: Two-component adsorption isotherms of BSA/Tg mixtures on CHT type-I in (●) 5 mM, (▲) 20 mM, (◆) 35 mM, and (▼) 50 mM $NaHPO_4$ each containing 250 mM NaCl at pH 7. Surfaces are generated from eq. 2.10 with the parameters shown in Table 3.2

Table 3.2: Best-fit parameters for the discount factor isotherm for the multicomponent equilibrium coadsorption of BSA and Tg on CHT type-I. Buffer is the $NaHPO_4$ concentration given in the table containing 250 mM NaCl at pH 7.0.

	5 mM		20 mM		35 mM		50 mM	
	q_m (mg/mL)	K (mL/mg)	q_m (mg/mL)	K (mL/mg)	q_m (mg/mL)	K (mL/mg)	q_m (mg/mL)	K (mL/mg)
BSA	47.5	4.1	31.4	0.7	22.3	0.4	13.7	0.4
Tg	85.1	14.4	52.2	10.3	32.3	2.5	21.3	0.5
ζ_{BSA}	0.281		0.149		0.022		0.181	

same for both proteins. In both cases, there is a sharp front that marks the interface between an advancing protein-saturated layer and a shrinking protein-free core which is consistent with a pore diffusion mechanism coupled with the favorable isotherms obtained for these conditions. There is, however, a substantially qualitative difference between the two proteins with BSA attaining concrete saturation of the particles in less than 5 min and Tg requires longer than 130 min. This difference is attributed to the much larger size and smaller diffusivities of Tg compared to BSA.

The effective diffusivities of BSA and Tg under non-binding conditions were determined from pulse-response experiments as described in Section 3.2.1 using data obtained at flow-rates between 0.5 and 4 mL/min. Figure 3.4 shows the corresponding van Deemter plot as reduced HETP, h, vs. reduced velocity, υ'. The slope is higher for Tg than for BSA indicating that diffusional hindrance is greater for Tg than for BSA. The nonbinding effective diffusivities are determined from eq. 3.1 and are shown in Table 3.3.

Figure 3.6 shows the batch uptake curves obtained for one-component adsorption of BSA and Tg in 5 mM $NaHPO_4$ with 250 mM NaCl at pH 7. As seen in this figure, the uptake curves are qualitatively the same for both proteins. However, consistently with the CLSM images, saturation is attained with BSA in less than 5 min while saturation of Tg requires longer than 130 min.

The effective pore diffusivities for these pore conditions were obtained by fitting the pore diffusion

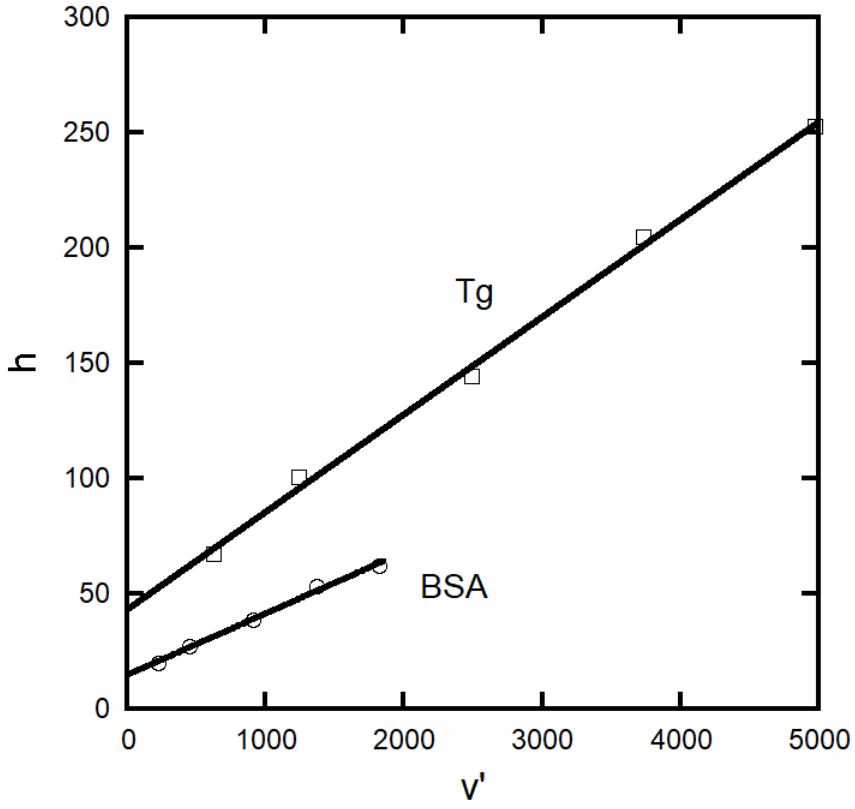

Figure 3.4: Reduced HETP vs. reduced velocity obtained for the BSA and Tg in a column packed with CHT type-I columns from pulse injections under non- binding conditions (505 mM $NaHPO_4$)

model to the batch uptake data. For Tg, the isotherm is sufficiently rectangular as to permit use of the analytical solution for a rectangular isotherm eq. 2.7. Conversely, for BSA for which the isotherm is only moderately favorable the numerical solution to the full (eqs. 2.5-2.6) was used. The effective diffusivities obtained in this manner are given in Table 3.3 along with the D_e values for non-binding conditions. As seen from this table, the D_e values of Tg are much smaller than those obtained for BSA both under non-binding and binding conditions. However, while the D_e values of BSA are the same whether binding occurs or not, for Tg the D_e value for binding conditions is much smaller than that observed without binding. This difference is attributed to the diffusional hindrance caused by the bound Tg molecules that restrict the space available for transport within the CHT pores.

Table 3.3: Summary of the effective diffusivities for BSA and Tg binding and non-binding conditions.

		non-binding conditions		binding conditions		
	D_0 (10^{-7} cm^2/s)	D_e (10^{-7} cm^2/s)	D_e/D_0	D_e (10^{-7} cm^2/s)	D_e/D_0	$\frac{D_{e,binding}}{D_{e,non-binding}}$
BSA	6	1.06	0.18	1.06	0.18	1
Tg	2.2	0.157	0.071	0.012	0.005	0.08

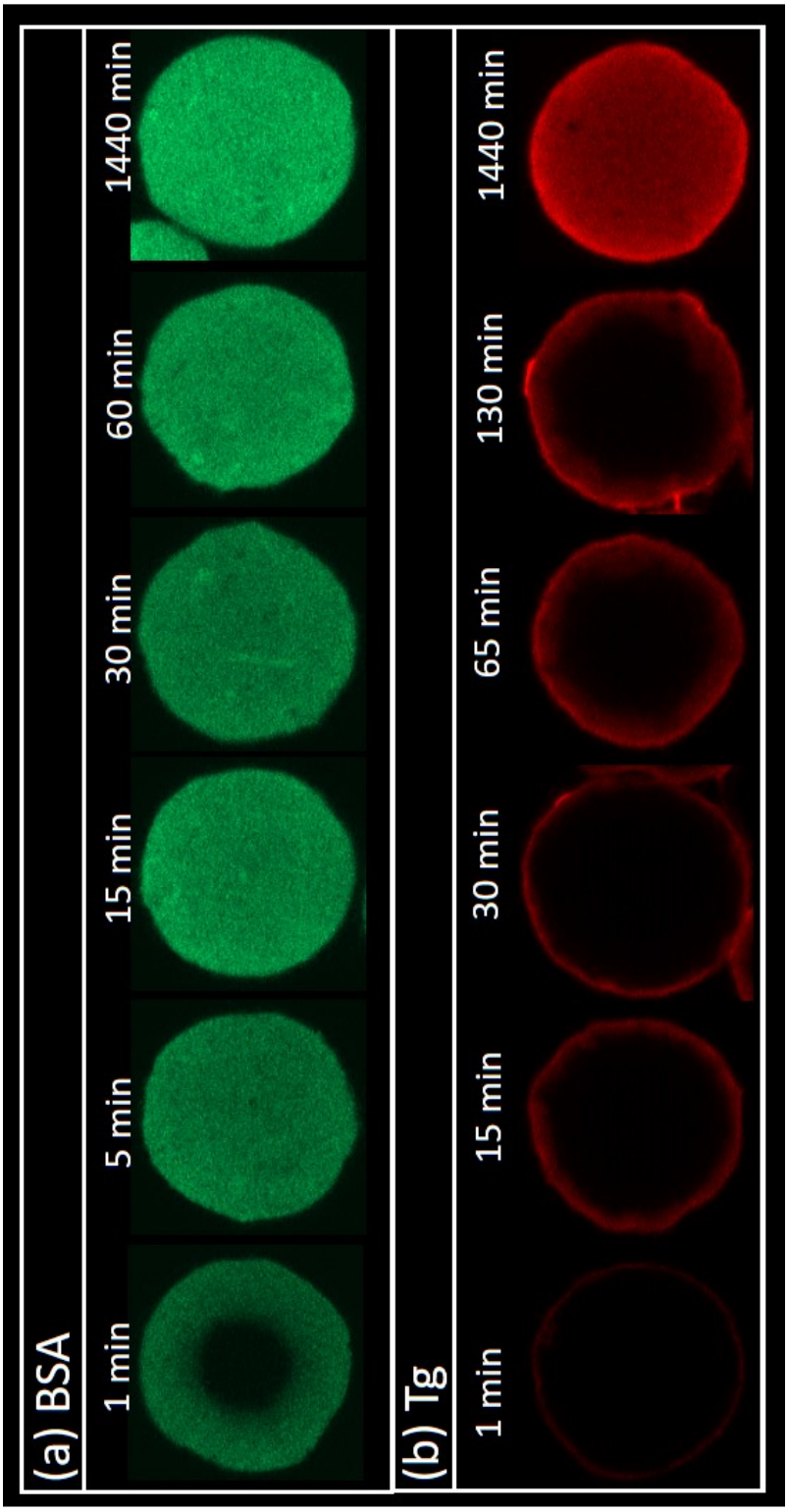

Figure 3.5: Representative CLSM images of the single component adsorption of (a) BSA and (b) Tg on CHT type-I. BSA and Tg concentrations were 1 mg/mL. Particles in the images shown have diameters $d_p = 40 \pm 2$ µm.

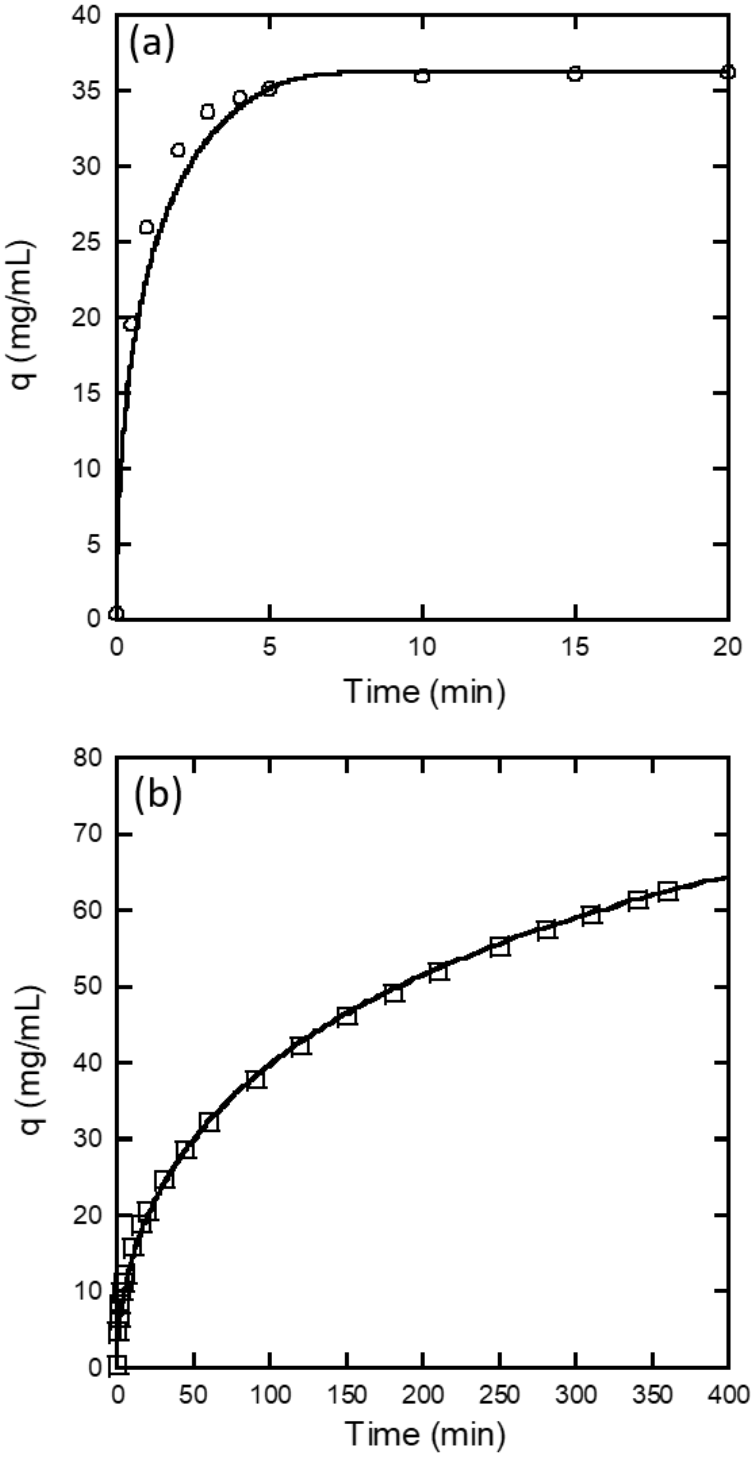

Figure 3.6: Batch uptake curves for the one-component adsorption of (a) BSA and (b) Tg on CHT type-I in 5 mM $NaHPO_4$ containing 250 mM NaCl at pH 7. $C_0 = 1$ mg/mL.

Figure 3.7 shows the one-component breakthrough curves obtained for 1 mg/mL BSA and 1 mg/mL Tg in 5 mM $NaHPO_4$ with 250 mM NaCl at pH 7 in packed CHT columns as described in Section 3.2.1. BSA demonstrates a sharp breakthrough curve characteristic of fast adsorption. Conversely, despite the longer residence time the Tg breakthrough curve is shallower than the BSA breakthrough curve consistent with a lower effective pore-diffusivity.

Given that BSA adsorption is rapid, breakthrough is likely to adhere to the constant pattern solution for column adsorption given by LeVan and Carta [92]. This analytical solution is appropriate when adsorption into the particles is fast and irreversible, in conjunction with sufficient time spent in the column such that a constant pattern protein front is formed. However, the isotherm is insufficiently rectangular to apply this analytical solution. Applying the same conservation equations to CHT column with mass transfer controlled by pore diffusion and assuming local equilibrium breakthrough can be simulated as previously discussed in Chapter 2. BSA breakthrough is well described by the numerical simulation with an effective diffusivity of 1.06×10^{-7} cm^2/s.

In the case of Tg, a constant pattern does not form since adsorption into the particles is slow despite the long residence time. Therefore, the general solution for non constant pattern is required [106]. The general non-constant pattern solution best fit the breakthrough curve with a D_e value of 7×10^{-10} cm^2/s. This is $\sim 60\%$ the effective diffusivity obtained from the batch kinetic measurement. Breakthrough predicted with D_e value of 1.2×10^{-9} cm^2/s results in a curve predicting later breakthrough than observed.

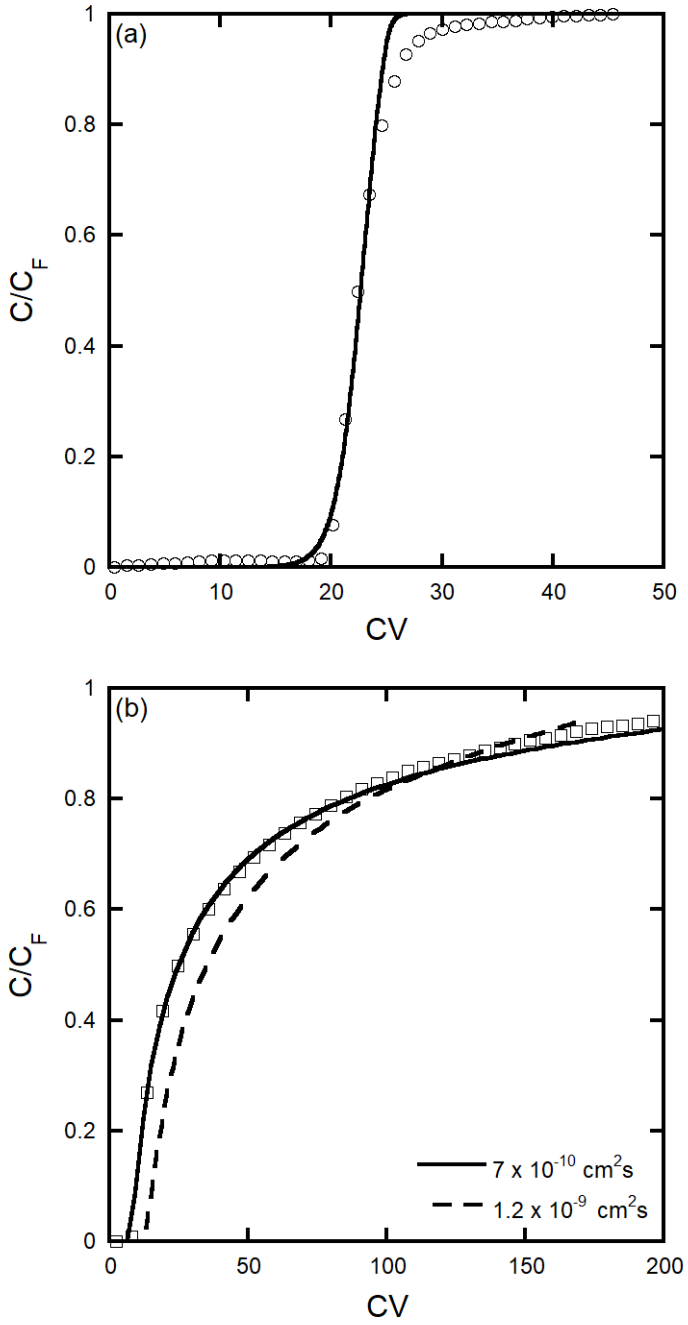

Figure 3.7: One-component breakthrough of 1 mg/mL of (a) BSA and (b) Tg in 5 mM $NaHPO_4$ with 250 mM NaCl at pH 7. Residence times are 2 min in (a) and 5 min in (b). Line shown in (a) is the numerical solution of the pore diffusion model (eqs. 2.5 and 2.18) with $D_e = 1.06 \times 10^{-7}$ cm^2/s. Lines shown in (b) are the analytical solution of the pore diffusion model with the effective diffusivities shown in the legend.

3.3 Preparation and characterization of agarose encapsulated CHT

This section focuses on examining the effects of the shearing rate, surfactant concentration, CHT concentration, and agarose concentration on the resulting agarose-encapsulated CHT particles. Once conditions for producing chromatographically suitable materials are found, these particles are evaluated for their applicability in the flow-through purification of large bio-particles. The agarose-encapsulated CHT particles must permit the adsorption of small proteins while preventing the adsorption of large proteins. This is tested with batch equilibrium adsorption and kinetic measurements, CLSM, and two-component breakthrough of mixtures containing small proteins and 30 nm nanoparticles.

3.3.1 Materials and methods

The CHT particles used in this work are the same as described in Section 3.2.1. High gel-strength and low electroendosmosis agarose (gel temperature 36 ^{o}C) was purchased from MilliporeSigma (St. Louis, MO, USA).

The proteins used in this work are BSA, Tg, and bovine IgM, purchased from MilliporeSigma (St. Louis, MO, USA). The pI and molecular mass of IgM are 5.5 - 6.7 (for human IgM) [123] and about 950 kDa, respectively. The hydrodynamic radii are 3.7 and 8.7 nm for BSA and Tg, respectively, [85], and 12.7 nm for IgM [124].

BSA sample was purified as described in section 2.2.1. Tg and IgM were used without purification. RNA from S. cerevisiae (product number R6750) was purchased as a lyophilized powder from MilliporeSigma (St. Louis, MO, USA). The absorbance of 1 mg/mL solution of this sample at pH

7 was 19.4 ± 0.7 at A260 with A260/A280 = 2.14 ± 0.03. These values suggest that the sample is of relatively high but not absolute nucleic acid purity [125][126]. As shown in Fig. 3.8, based UPLC-SEC analyses, this RNA sample contains a broad distribution of molecular masses ranging in hydrodynamic radius between 2 and 5 nm with the bulk being around 2.2 nm in radius. All RNA solutions were prepared with water treated with 0.1% diethyl pyrocarbonate (DEPC) to inactivate RNases and autoclaved.

DiagNano^{TM} carboxylate-modified silica-nanoparticles incorporating green (abs. max = 485/em. max = 510) and red (abs. max = 569/em. max = 586) fluorescent dyes with nominal diameters of 30 nm and 50 nm, respectively, and polydispersity index < 0.2 were purchased from Creative Diagnostics (Shirley, NY, USA). The actual radii of these particles were determined by dynamic light scattering (DLS) at 20 ^{o}C with a DynaPro Nanostar instrument (Wyatt Technology, Santa Barbara, CA, USA). Representative DLS data are shown in Fig. 3.8. Mean radii and standard deviations calculated from these data are 14.7 ± 5.2 nm and 26.3 ± 9.9 nm, for the 30 and 50 nm samples, respectively, corresponding to polydispersity index values $PDI = (\sigma/\bar{r})^2$ of 0.13 and 0.14, respectively, where σ^2 is the variance of the distribution and $\bar{r}$ is the mean radius.

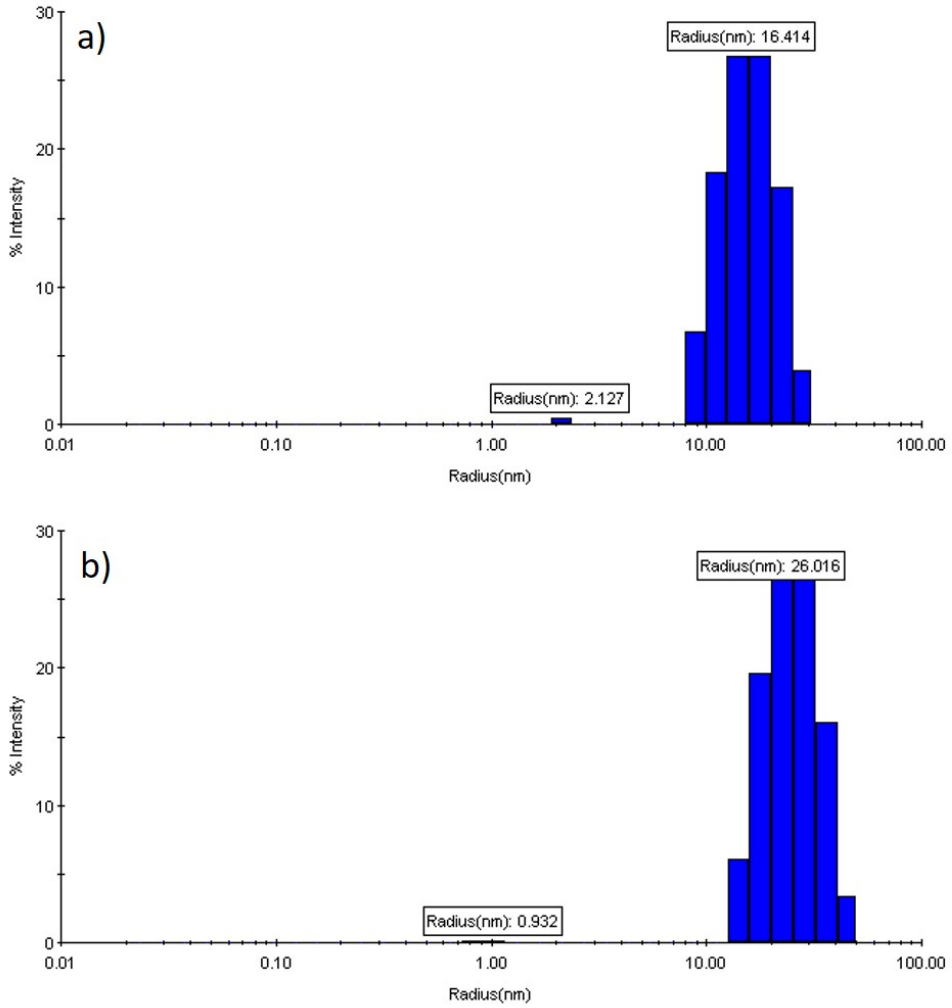

Figure 3.8: Particle size distribution based on DLS measurements of (a) 30 nm and (b) 50 nm silica nanoparticles samples. Mean radius, standard deviation, and polydispersity index values are given in the text.

3.3.2 Preparation of agarose-CHT composites

The method used to prepare agarose-CHT particle composites follows that described in [99] to produce plain agarose beads. The steps are illustrated in Fig. 3.9 along with a schematic of the equipment used. CHT particles are first washed with distilled deionized water to remove fines, oven dried for 4 h at 115 ^{o}C, and then placed in a 30 mL beaker containing a pre-weighed amount of dry agarose followed by the addition of 10 mL of degassed, deionized water. The beaker is then placed in a double boiler at 100 ^{o}C on a hot plate and the contents are mixed by pipetting the mixture in and out for 10 min to ensure an even distribution of the CHT particles throughout the agarose solution until reaching a temperature of 95 ^{o}C. No settling of the CHT particles was observed after mixing likely because of the high viscosity of the agarose solution. The hot suspension is then loaded into a syringe heated with heating tape with a voltage controller obtained from Allied Electronics and Automation (Fort Worth, TX, USA) for dropwise addition into a 100 mL baffled and stirred jacketed glass reaction vessel, obtained from Chemglass Life Sciences (Vineland, NJ, USA), containing 2% (v/v) Span 85 in cyclohexane kept at 60 ^{o}C by circulating water from a high-temperature bath through the vessel jacket. The final ratio of agarose-CHT suspension to cyclohexane was 1:40 (v/v).

Two different types of stirrers were tested. The first is an overhead stirrer obtained from Caframo Lab Solutions (Ontario, Canada), fitted with a 5-cm diameter impeller with two pitched blades and operated at 2,000 rpm. The second is a Model IKA T-18 rotor-stator homogenizer, obtained from IKA-Werke (Staufen im Breisgau, Germany), operated at different speeds between 5,000 and 22,000 rpm. After mixing for 10 min, the suspension is cooled in about 30 s by changing the direction of flow with the 3-way valves from the hot water bath to the 25 ^{o}C water bath followed by 5 min of additional stirring at 25 ^{o}C. The composite beads are then collected by opening the

vessel drain valve over a 20-μm mesh screen and washed with a 20% ethanol/water solution (v/v) at room temperature. The washed beads are then crosslinked according to procedure described in [111][61]. For this purpose, the beads are added to a tube containing 1.0 mL of 1 N NaOH, 0.45 mL of deionized water, and 0.23 mL of epichlorohydrin, each per mL of settled particles, gently rotated end-over-end for 3 h at room temperature (21 $\pm$ 1 ^{o}C). After crosslinking, the beads are washed with 20% ethanol, sieved between screens with apertures of 300 and 100 μm, and stored. The CHT content of the precursor suspension was varied between 0.04 and 0.25 g dry CHT per mL of agarose solution. Two different values of the agarose content were tested: 0.06 g agarose per mL of water (6%) and 0.10 g agarose per mL of water (10%). Agarose-only beads with 6% and 10% agarose content were also synthesized as described above using the homogenizer at a stirring speed of 5,000 rpm.

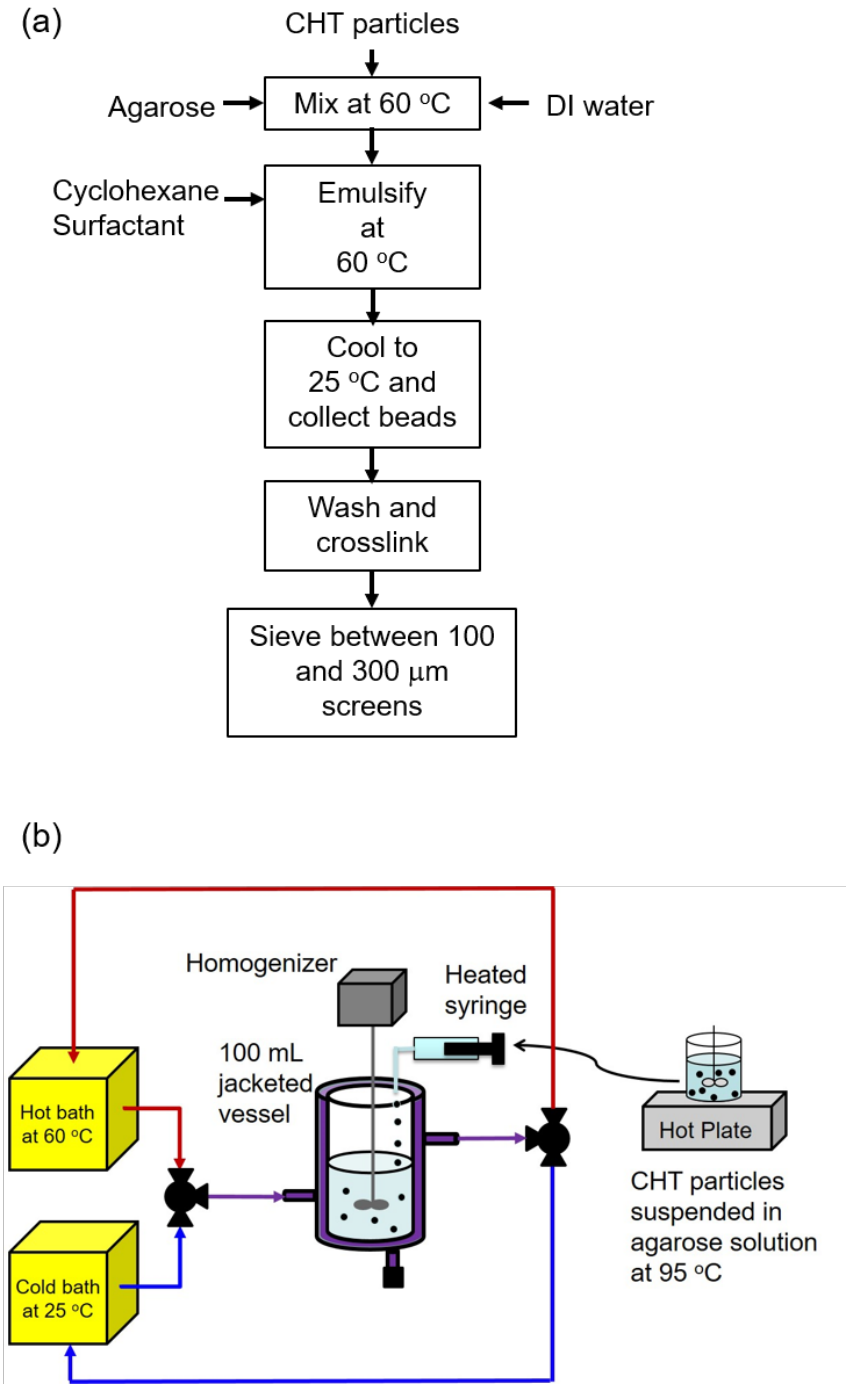

Figure 3.9: Steps used to prepare agarose-CHT composite beads (a) and schematic of experimental apparatus (b).

3.3.2.1 Physical property characterization

The overall morphology and bead size distribution of the composite beads were obtained from micrographs obtained using a Hirox RH-8800 Light Microscope (Tokyo, Japan) using ImageJ (NIH, Bethesda, MD, USA) for image analysis. Encapsulation efficiencies were calculated by recording the number of beads containing CHT particles relative to the total number of beads. The distribution of CHT particles within the composite beads was visualized by first dehydrating the beads in a water-ethanol gradient from 0 to 100% (v/v) anhydrous ethanol in 20% increments. Upon completion of the 100% ethanol wash, the beads were washed with 50% (v/v) LR White embedding resin (obtained from VWR, Radnor, PA, USA) dissolved in ethanol followed by a wash with pure LR White and finally allowed to set for 24 h at 45 °C. After setting, the LR White-embedded samples were microtomed into 1 μm thick slices, stained with toluidine blue, and imaged with the Hirox RH-8800 microscope.

The density of the hydrated composite particles, ρ_{AgCHT}, was determined using a pycnometer. Their CHT content on a mass fraction basis, χ_{CHT}, was determined gravimetrically by placing weighed samples of the hydrated AgCHT particles in a quartz tube furnace (Model GSL 1100X, MTI Corporation, Richmond, CA, USA) at 400 °C. for 2 h. Finally, the volume fraction of CHT particles in the hydrated composite beads, ϕ_{CHT} in mL of CHT particles per mL of bead, was calculated from the following equation:

$$\phi_{CHT} = \frac{\rho_{AgCHT} \times \chi_{CHT}}{\rho_{s,CHT}\left(1 - \epsilon_{p,CHT}\right)} \tag{3.2}$$

where $\rho_{s,CHT} = 3.1$ g/mL is the skeletal density of the CHT particles and $\epsilon_{p,CHT} = 0.73$ is their porosity.

The size-exclusion limit, porosity, and pore size of the composite beads were determined by iSEC using glucose and dextran standards ranging from 4 to 2,000 kDa as described in [36]. The iSEC experiments were performed by packing the AgCHT samples into 0.5 cm diameter Tricorn 10/100 columns (obtained from Cytiva, Marlborough, MA, USA) to bed heights between 9.1 and 14.8 cm and operated at flow rates giving a residence time of 10 min. Separate pulse injections (20 µL) of 5 mg/mL samples were made for each dextran using a Waters HPLC system monitored with a R401 refractive index detector (Waters Corporation, Milford, MA, USA). The mobile phase was 200 mM sodium phosphate containing 250 mM sodium chloride at pH 7. The distribution coefficient, K_c , was calculated for each standard from the following equation:

$$K_c = \frac{V_R/V_c - 1}{1 - \epsilon} \tag{3.3}$$

where V_R is the retention volume calculated from the peak first moment, V_c is the column volume, and ϵ is the extraparticle or external porosity. The latter was calculated from the retention volume of the 2,000 kDa dextran assuming that it is completely excluded. Based on the cylindrical pore model, K_c is theoretically related to the molecular radius by [36][127]:

$$K_c = \epsilon_p \left(1 - r_m/r_{pore}\right)^2 \tag{3.4}$$

3.3.2.2 Functional properties

All adsorption experiments were done at room temperature (21 $\pm$ 1 ^{o}C) in buffers containing 5 mM $NaHPO_4$ and 250 mM NaCl adjusted to pH 7 by the addition of phosphoric acid. Adsorption isotherms were obtained by mixing known quantities of hydrated beads in tubes containing 1.5 mL solutions of BSA or RNA at initial concentrations ranging from 0.3 to 4.5 mg/mL gently rotated end-over-end for 24 h. The initial and final supernatant concentrations were measured with a Nanodrop

2000c spectrophotometer (ThermoFisher Scientific, Waltham, MA, USA) and the amount of BSA or RNA bound was calculated by mass balance. Adsorption capacities were expressed as the bound mass divided by the bead volume as well as the bound mass divided by the volume of CHT particles within the beads.

Confocal laser scanning microscopy (CLSM) was used to visualize the distribution of bound RNA, BSA, Tg, IgM, and silica nanoparticles in the beads. For this purpose, the protein samples were conjugated to either Rhodamine Green-X or Rhodamine Red-X amine-reactive dyes, obtained from Life Technologies (Waltham, MA, USA), following the method described in [31]. The degree of labeling after conjugation was 28%, 19%, and 55% for BSA, Tg, and IgM, respectively. RNA was labeled using a UlysisTM Alexa Fluor^{TM} 647 labeling kit, obtained from ThermoFisher Scientific (Waltham, MA, USA), by first dissolving 25 mg/mL of RNA into the supplied labeling buffer and then denaturing the RNA to facilitate labeling by holding the solution for 5 min at 95 ^{o}C followed by snap cooling on ice. A 20 μL aliquot of the labeling complex was then added to the denatured RNA solution and heated to 90 ^{o}C for 10 min followed again by snap cooling on ice. Finally, unreacted dye was removed using a centrifugal Bio-Rad P-30 buffer exchange column (Bio-Rad Laboratories, Hercules, CA, USA) at 1,000g for 4 min. In each case, the labeled samples were spiked into the corresponding unconjugated sample to obtain a final 1:40 ratio.

Batch CLSM measurements were done by mixing small resin samples, dosed in amounts estimated to yield less than a 10% drop in supernatant concentration, with 10 mL of solution in 15 mL tubes gently rotated end-over-end. At various times, small samples of the suspension were pipetted out and centrifuged at 13,200 rpm for 30 s in nylon Spin-X microfiltration tubes (Corning Incorporated, Corning, NY, USA) to remove the supernatant. The filtered beads were then resuspended in benzyl alcohol, which matches, approximately, the refractive index of CHT and imaged as described in [61]. Unfortunately, benzyl alcohol causes the encapsulating agarose gel to shrink dramatically

which distorts the original shape of the beads. This step is, however, necessary to visualize binding within the CHT particles that are otherwise opaque in aqueous buffer.

Breakthrough curves were obtained for one-component feeds containing either BSA, RNA, or Tg and for mixtures of the 30 nm nanoparticles with either BSA or RNA. These experiments were done with an AKTA^{TM} Prime 25 system (Cytiva, Marlborough, MA, USA) at a residence time of 5 min, corresponding to flow rates between 0.3 and 0.4 mL/min with the same columns used for the iSEC experiments. For BSA and Tg, detection was at 280 nm, while for RNA detection was at 305 nm. A wavelength at the more typical 260 nm could not be used for RNA since the corresponding absorbance was too high to be monitored by the AKTA system. A linear relationship between A305 and RNA concentration was verified by serial dilution. For the two-component feeds, detection was at 280 and 485 nm for BSA/nanoparticle mixtures and at 305 and 485 nm for RNA/nanoparticle mixtures. Given that, in both cases, only the nanoparticles absorb significantly at 485 nm, breakthrough of each component was determined by deconvoluting the 280/485 nm signals for the BSA/nanoparticle mixtures and the 305/485 nm signals for the RNA/nanoparticle mixtures. After each run, the column was eluted with a 10 CV gradient from 5 to 505 mM $NaHPO_4$ at pH 7 followed by a 2 CV wash at the final phosphate concentration.

3.3.3 Effect of bead preparation parameters

Several parameters were varied initially to determine conditions suitable for the preparation of agarose-CHT composites with size and CHT content appropriate for flow-through purifications. We quantified the fraction of beads recovered between 300 and 100 μm screens along with the fraction of beads in this size range that contained CHT particles obtained for different preparation condition. Table 3.4 shows the results obtained by varying the mixer type and rpm and the CHT content of the precursor agarose-CHT suspension. As seen in this table, using the impeller mixer at

2,000 rpm (which maximum speed of the stirrer used) resulted in a relatively low fraction (0.25) of beads in 100-300 μm size range. A much higher fraction (0.70) was obtained with the homogenizer at higher speeds up to 18,000 rpm. Even higher speeds were also tested but were found to disrupt the particles. Table 3.4 also shows that the encapsulation efficiency increased with the CHT content of the precursor agarose solution attaining values close to 100% at a CHT content of 0.14 g/mL or higher in the precursor suspension.

Table 3.4: Fraction of beads produced from 6% agarose composites sieved between 100 and 300 μm and encapsulation efficiency defined as the fraction of beads containing CHT particles.

Mixer type	rpm	CHT content in precursor suspension, g dry CHT/mL solution	Fraction of beads sieved between 100 and 300 μm	Encapsulation efficiency for beads sieved between 100 and 300 μm
Impeller	2,000	0.02	0.25	0.77
		0.11	0.25	0.93
		0.14	0.25	0.99
		0.25	0.25	0.99
Homogenizer	4,000	0.25	0.10	0.99
	8,000	0.25	0.20	0.99
	14,000	0.25	0.24	0.99
	18,000	0.25	0.70	0.99

Figure 3.10 shows some representative images of composite beads in 6% agarose prepared with precursor CHT concentrations of 0.02, 0.10, and 0.25 g dry CHT per mL of agarose solution. As seen from this figure, the composite beads contain multiple CHT particles and appear to be quite full at a CHT content in the precursor suspension of 0.25 g/mL. We also tested the effect of varying the Span 85 concentration in cyclohexane in the 2-8% (v/v) range with the impeller mixer at 2,000 rpm but no significant effect was observed.

Based on the observations in Fig. 3.10, a precursor suspension containing 0.25 g dry CHT/mL with 6 and 10% agarose content, homogenizer mixing at 18,000 rpm, and 2% Span 85 in cyclohexane

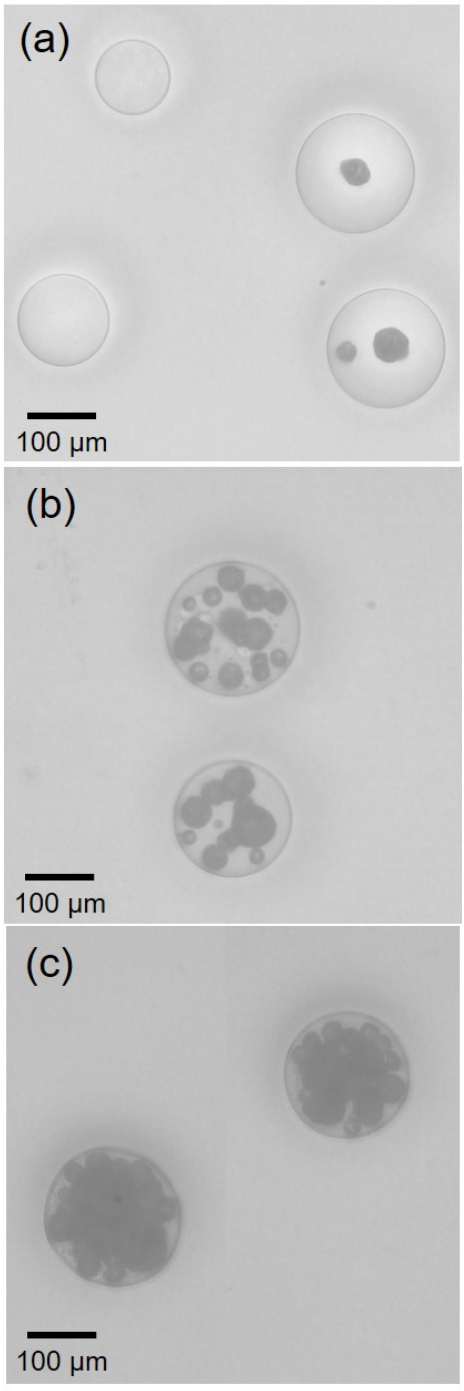

Figure 3.10: Representative optical micrographs of agarose-CHT composite beads prepared with precursor suspensions with (a) 0.02, (b) 0.10, and (c) 0.25 g dry CHT per mL agarose solution. The beads were prepared with 6% agarose using the impeller mixer at 2,000 rpm. The image in (c) was spliced to show, in the same frame, two different particles taken from the same micrograph.

were chosen to prepare materials for further characterization and functional testing. Hereinafter, we refer to these materials as 6%AgCHT and 10%AgCHT.

3.3.4 Physical properties of 6%AgCHT and 10%AgCHT

Table 3.5 provides a summary of the physical properties of 6%AgCHT and 10%AgCHT prepared as described in Section 3.3.2.2.

Table 3.5: Physical properties of 6%AgCHT and 10%AgCHT.

Property	6%AgCHT	10%AgCHT
Mean bead diameter and standard deviation (μm)	105 ± 22	207 ± 30
Hydrated bead density, ρ_{AgCHT} (g/mL bead)	1.28 ± 0.01	1.22 ± 0.01
CHT mass fraction, χ_{CHT} (g CHT/g bead)	0.25 ± 0.01	0.18 ± 0.02
CHT volume fraction, χ_{CHT} (mL CHT/mL bead)	0.36 ± 0.01	0.25 ± 0.02
Intraparticle porosity, ϵ_p	0.85 ± 0.02	0.91 ± 0.04
Pore radius, r_{pore} (nm)	15.1 ± 0.6	8.8 ± 0.5
Extraparticle porosity of the packed column, ϵ	0.42	0.40

Figure 3.11 shows the bead size distribution for the two materials. Both distributions are essentially symmetrical, but the 10%AgCHT is shifted toward higher diameters. The corresponding mean bead diameters and standard deviations are 105 ± 22 μm for 6%AgCHT and 207 ± 30 μm for 10%AgCHT. Since the two materials were prepared with the same mixer at the same rpm, the larger size of the 10%AgCHT beads is likely a result of the increased viscosity of the 10% agarose precursor suspension.

Figure 3.12 shows the distribution of the CHT particles encapsulated within the 6% and 10%AgCHT beads. In these images, obtained by embedding and physically sectioning the samples as described in Section 3.3.2.1, the encapsulated CHT particles appear somewhat darker than the surrounding agarose since they are much denser. Comparing these images with those in Fig. 2 for the non-embedded beads, it is evident that embedding and physical sectioning cause significant deformation

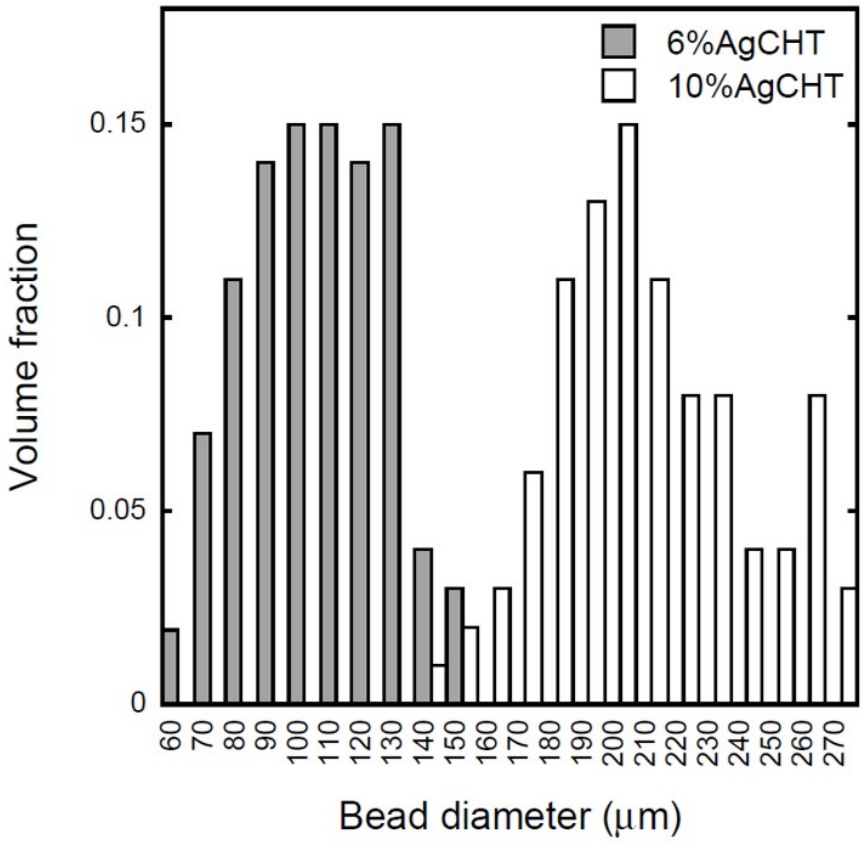

Figure 3.11: Bead diameter distribution for 6%AgCHT and 10%AgCHT samples. Volume average diameters and standard deviations are given in Table 3.5

of the beads and, likely, some shrinkage of the agarose. Moreover, since the beads are randomly located in the embedded sample, the sections shown do not necessarily correspond to the equator of each bead. Despite these limitations, we can conclude that the CHT particles are randomly distributed within the encapsulating agarose and that there are virtually no un-encapsulated CHT particles. As seen in Table 3.5, the CHT particle content of the composite beads is 36% (v/v) for 6%AgCHT and 25% (v/v) for 10%AgCHT. Using the skeletal density and porosity of the CHT particles listed in Table 3.1, we can calculate that the CHT particle content in the precursor suspension was 28% (v/v). Thus, the values obtained for the composite beads are similar to the CHT content of the precursor suspension once the fraction of beads without CHT is accounted for. An important question is whether it may be possible to obtain higher volume fractions. Huang and Yu [128] have analyzed the problem of how many spheres can be physically packed in a larger sphere. Their results show that this number depends on the ratio of the radii of the smaller spheres and of the larger one that contains them. For the 6%AgCHT beads, which have a mean diameter of 105 μm, this ratio is $41/105 = 0.390$, which, according to Huang and Yu, corresponds to a maximum between 6 and 7 spheres packed within the larger one. The corresponding volume fraction is then predicted to be between $6x0.390^3$ and $7x0.390^3$ or between 0.357 and 0.417. Our experimental result of 0.36 is in this range, suggesting that it would be difficult to obtain a higher CHT content. The same calculation for the 10%AgCHT beads, which are larger, yields a ratio of radii of 0.20 and a predicted maximum volume fraction of 0.528. This value is considerably larger than our experimentally determined one, indicating that, for 10%AgCHT, the CHT volume fraction is limited by the CHT content of the precursor suspension. In turn, this suggests that, theoretically, a higher CHT content might be obtained starting with a denser CHT suspension. On the other, we found that it was difficult to obtain a uniform dispersion of the CHT particles at higher suspension densities in large part because of the high viscosity of the agarose solution. Thus, although, in theory, higher inner particle densities

may be achieved, these higher values may be difficult to obtain in practice.

Figure 3.13 shows the iSEC results for both 6%AgCHT and 10%AgCHT along with the corresponding values obtained for 6 and 10% agarose beads without CHT. As seen from Fig. 3.13, there is only a small difference in size exclusion properties between the AgCHT beads and the agarose-only beads with the same agarose content, suggesting that the size exclusion properties are determined largely by the agarose phase. Conversely, as expected, the agarose content has a large effect resulting in a size exclusion limit that decreases from about 15 nm radius to about 9 nm radius as the agarose content is increased from 6 to 10%. Figure 3.13 also shows lines based on eq. 3.4 fitted to the data. The regressed parameter values for 6%AgCHT and 10%AgCHT are given in Table 3.5. The corresponding values for the agarose-only beads are $\epsilon_p = 0.98 \pm 0.02$ and $r_{pore} = 15.1 \pm 0.5$ nm for 6% agarose and $\epsilon_p = 0.97 \pm 0.04$ and $r_{pore} = 8.6 \pm 0.5$ nm for 10% agarose. As seen from these results, encapsulating CHT reduces the porosity significantly but does not affect the effective pore radius. Conversely, increasing the agarose content from 6 to 10% reduces the effective pore size nearly two-fold with both agarose contents.

3.3.5 Functional properties of 6%AgCHT and 10%AgCHT

Figure 3.14 shows the adsorption isotherms for BSA and RNA for the AgCHT samples and for CHT alone both on a bead-volume basis, q, and on a CHT-volume basis, $q' = q/\phi_{CHT}$, plotted vs. the supernatant solution concentration, C. Isotherms for Tg, IgM, and for the nanoparticles were not obtained since these species are substantially excluded from the AgCHT beads. When compared on a bead volume basis, the binding capacities of the composite AgCHT beads for BSA and RNA are much smaller than the corresponding capacities obtained for CHT alone. On the other hand, when these capacities are compared based on the volume of CHT particles, whether alone or agarose-encapsulated, the results are in much closer agreement with each other for both

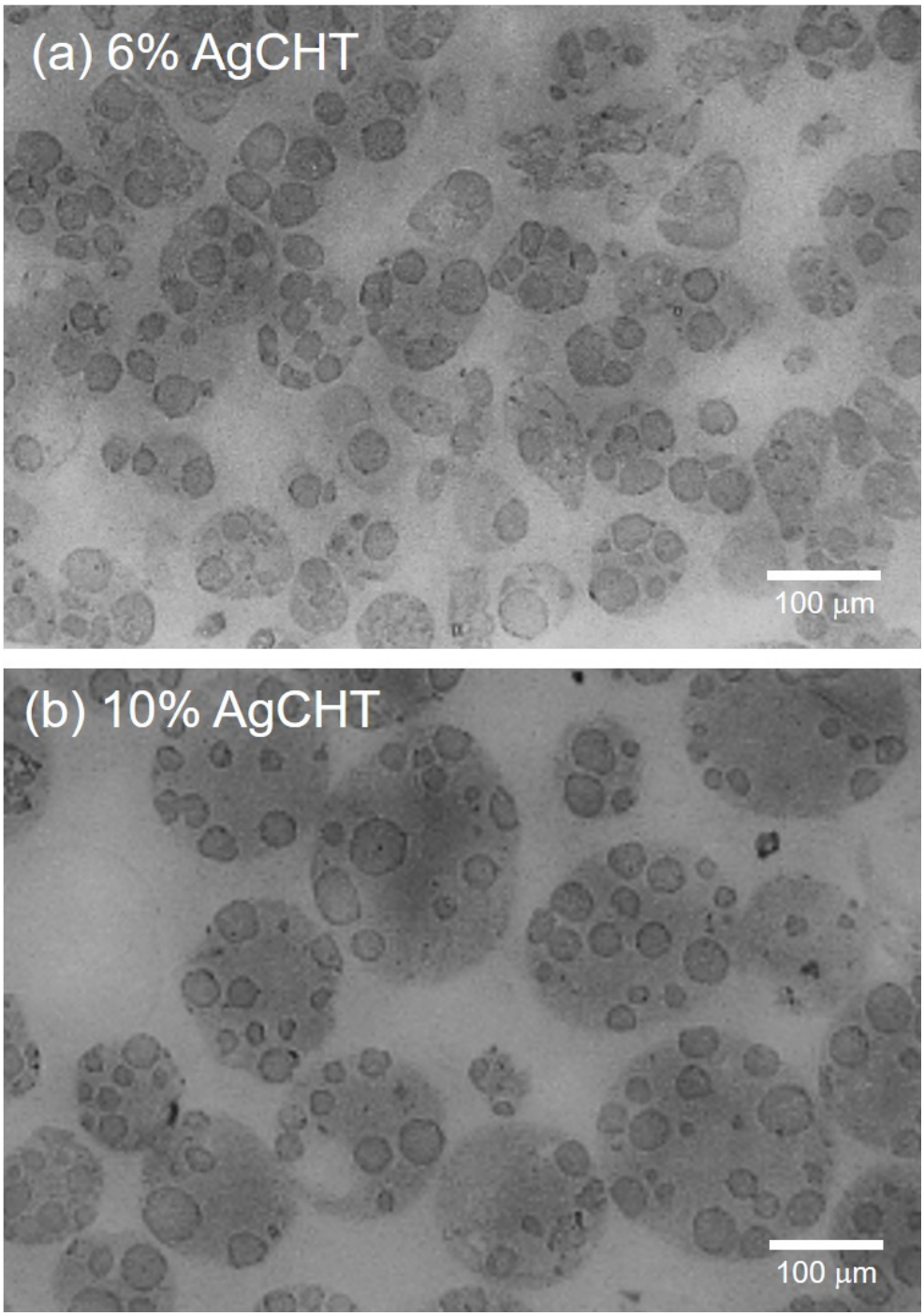

Figure 3.12: Optical micrographs of 1 µm-thick sections of (a) 6%AgCHT and (b) 10%AgCHT beads that have been dehydrated, embedded in LR White, microtomed, and stained with toluidine blue.

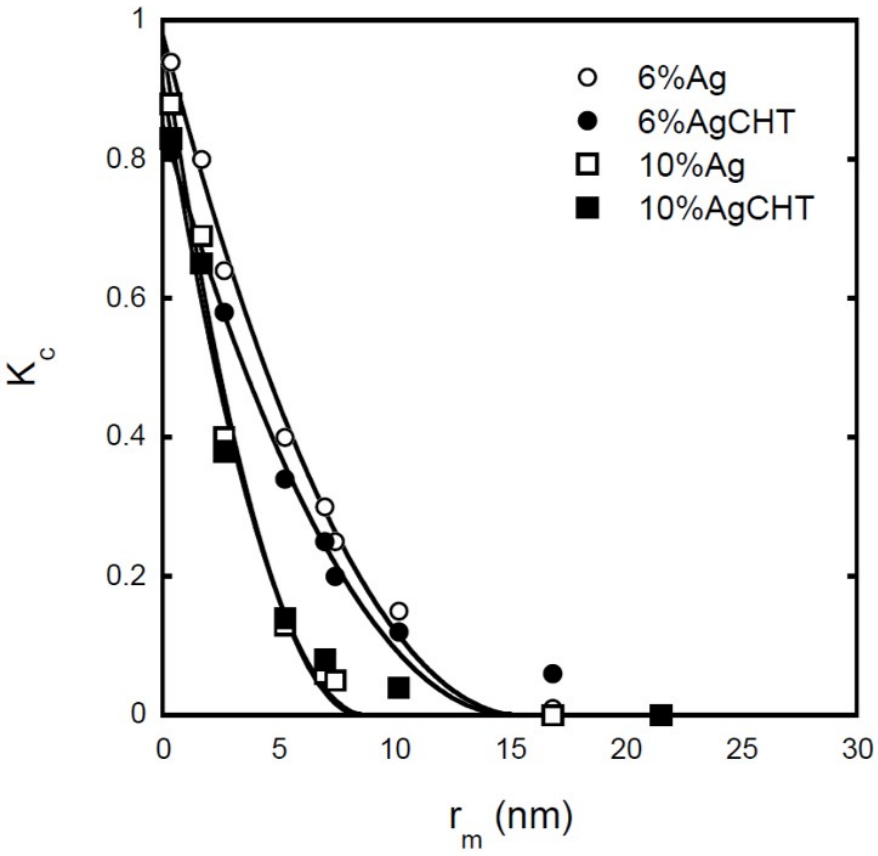

Figure 3.13: iSEC results for 6%AgCHT, 10%AgCHT, and for 6% and 10% agarose without CHT. Lines are calculated from eq. 3.4 with parameters values given in the text.

BSA and RNA. This result suggests that the agarose does not affect the binding capacity of the encapsulated CHT particles in a major way. The hydrodynamic radii of both BSA and of the RNA used are considerably smaller than the size exclusion limit of both 6%AgCHT and 10%AgCHT so that relatively rapid adsorption is expected. For BSA, the 6%AgCHT data and those for CHT alone are essentially coincident, while the 10%AgCHT values are about 20% smaller indicating that some of the CHT binding sites may become inaccessible in 10% agarose. This trend is reversed for RNA, with 6%AgCHT and 10%AgCHT showing close agreement with each other and the CHT-only capacity being, on average, about 25% smaller. The bulk of the RNA used in these experiments is much smaller than BSA (2.2 vs. 3.7 nm radius). Thus, we expect that RNA will be less affected by the presence of agarose. On the other hand, the RNA sample also contains a fraction of larger size that may be more significantly affected at the higher agarose content.

Figure 3.15 shows CLSM images of CHT, 6%AgCHT, and 10%AgCHT exposed, individually, to RNA, BSA, Tg, and IgM, and to the 30 and 50 nm silica nanoparticles over long times (30 to 120 min). Each CLSM image represents, approximately, the bead equatorial section. Optical microscopy images are also shown digitally superimposed to the CLSM images. As noted in Section 3.3.2.2, the composite beads are deformed when they are placed in benzyl alcohol and no longer appear spherical as they did in their hydrated state. Placing the benzyl alcohol saturated beads in an aqueous buffer was observed to restore the original spherical bead shape by re-swelling the agarose. Thus, benzyl alcohol only shrinks the agarose but does not appear to disrupt it. As a result, we conclude that the encapsulated CHT particles are retained within each bead during the process used to image them. As seen in Fig. 3.15, RNA binds to unencapsulated CHT as well as to the AgCHT beads saturating all the encapsulated CHT particles. This also occurs for BSA in CHT only and in 6%AgCHT. However, in 10%AgCHT, even after 60 min, saturation of the encapsulated CHT particles is obviously incomplete. In the case of Tg and IgM, binding on unencapsulated CHT

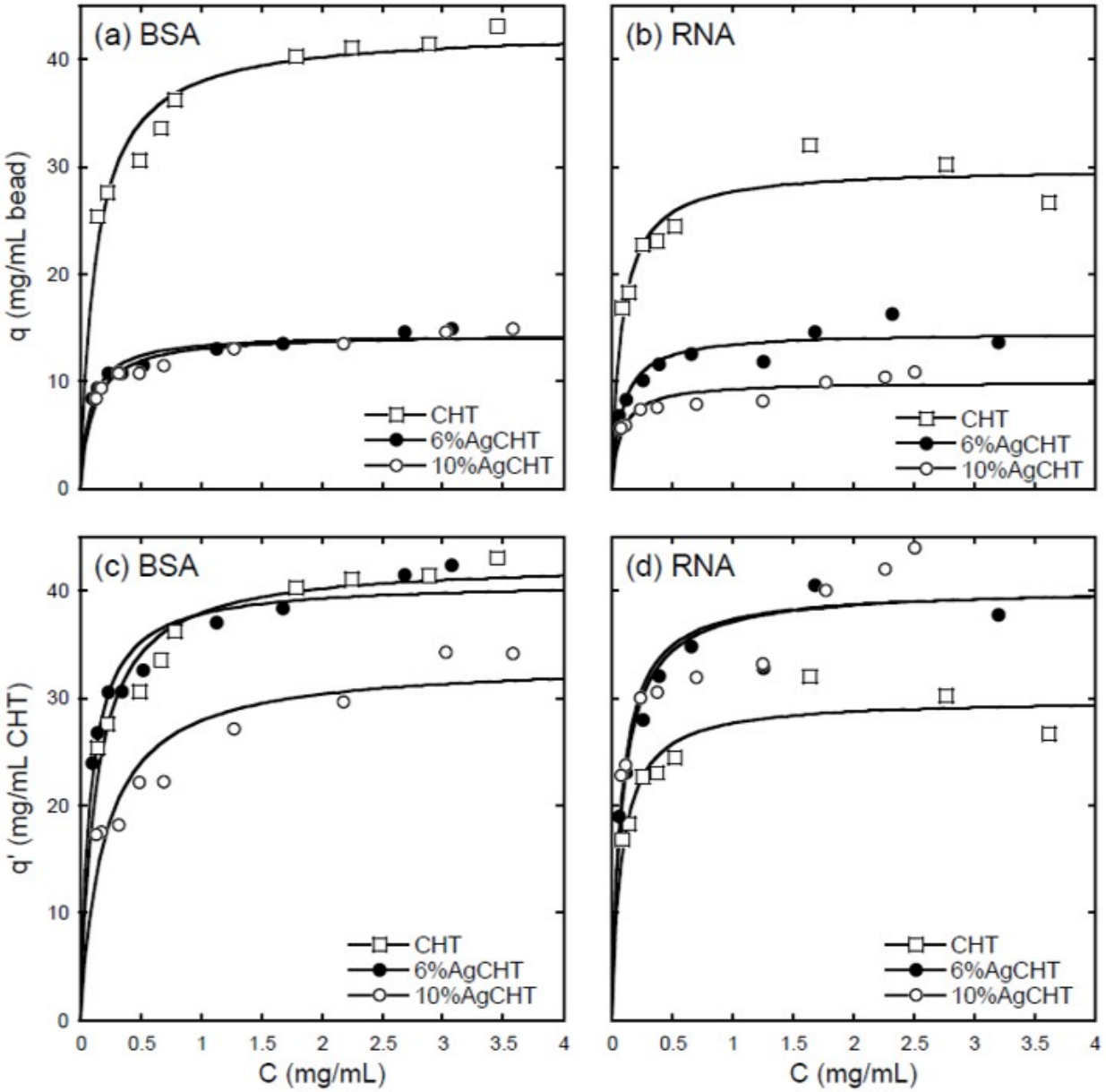

Figure 3.14: Adsorption isotherms of BSA (a and c) and RNA (b and d) on CHT, 6%AgCHT, and 10%AgCHT. The q-values in (a) and (b) are mg bound per mL of bead while q'-values in (c) and (d) are in mg bound per mL of CHT particles. Lines are fitted to the Langmuir isotherm, $q = (q_m KC)/(1 + KC)$, to guide the eye.

occurs primarily in a relatively thin shell at the particle surface. In contrast, there is essentially no binding of either Tg or IgM in any of the encapsulated CHT particles. Some Tg and IgM does appear to be present at the bead surface. However, this bound layer is very thin and not uniformly distributed over the bead surface. Results like those obtained for Tg and IgM are also observed for the 30 and 50 nm silica nanoparticles. In both cases, the nanoparticles diffuse and bind to a limited but significant extent in unencapsulated CHT. However, there is essentially no binding of either nanoparticle in any of the encapsulated CHT particles. In this case too, however, there appears to be some nanoparticle binding at the outer bead surface. It is possible that this binding results, at least in part, from the shrinking that occurs when the AgCHT beads are placed in benzyl alcohol to prepare them for CLSM.

Figure 3.16 shows the time course of adsorption of RNA and BSA in 6%AgCHT and in 10%AgCHT. Only the CLSM images, taken in benzyl alcohol, are shown in this case. As seen from this figure, RNA binds relatively quickly to the CHT particles in both 6%AgCHT and 10%AgCHT. BSA also binds relatively quickly to the CHT particles in 6%AgCHT. However, binding in 10%AgCHT appears to be slow.

The results shown in Figs. 3.15 and 3.16 are generally consistent with the size exclusion properties determined by iSEC and with the size of these test proteins and nanoparticles. As shown, for example, in [28], diffusion is expected to be highly hindered when the ratio of molecule and pore radii exceeds about 0.2. As shown in Table 3.5, the effective pore size of 6%AgCHT is 15.1 nm. As a result, RNA ($r_m/r_{pore} \sim 0.15$ based on the predominant radius of 2.2 nm) and BSA ($r_m/r_{pore} \sim 0.25$) can diffuse in rapidly. Conversely, diffusion of Tg ($r_m/r_{pore} \sim 0.58$) and IgM ($r_m/r_{pore} \sim 0.84$) is expected to be extremely slow. This effect is exacerbated in 10%AgCHT, whose pore radius is 8.8 nm. In this case, diffusion of BSA ($r_m/r_{pore} \sim 0.42$) is also expected to become very slow while both Tg and IgM are expected to be essentially completely excluded. In both 6% and 10%AgCHT,

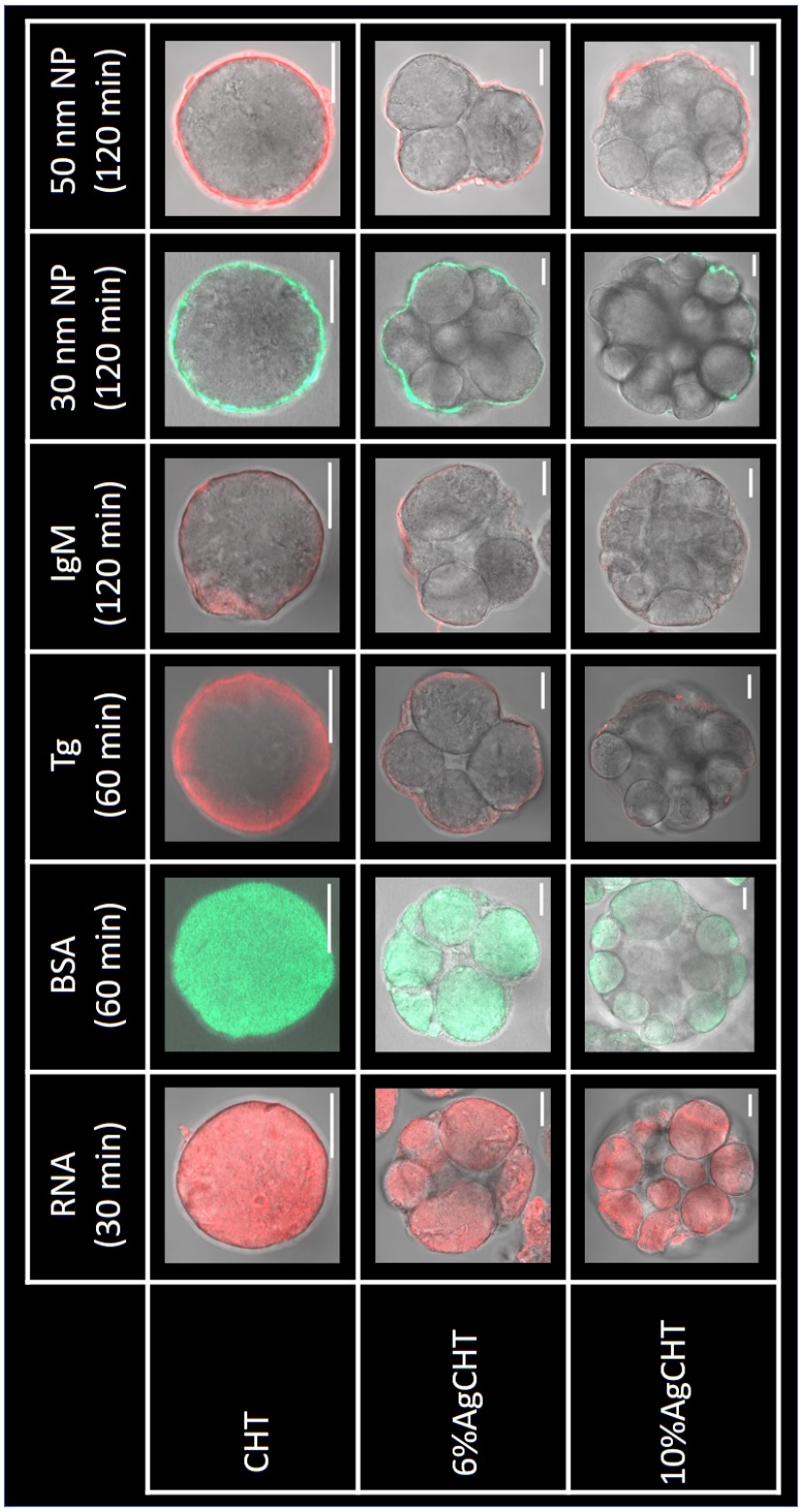

Figure 3.15: Digitally superimposed CLSM and optical microscopy images showing binding at long times for beads incubated with one-component solutions of RNA (1.8 mg/mL), BSA (2 mg/mL), Tg (2 mg/mL), IgM (0.78 mg/mL), 30 nm nanoparticles (2 mg/mL), and 50 nm nanoparticles (2 mg/mL). Images are taken in benzyl alcohol. The scale bar in each image is 25 µm.

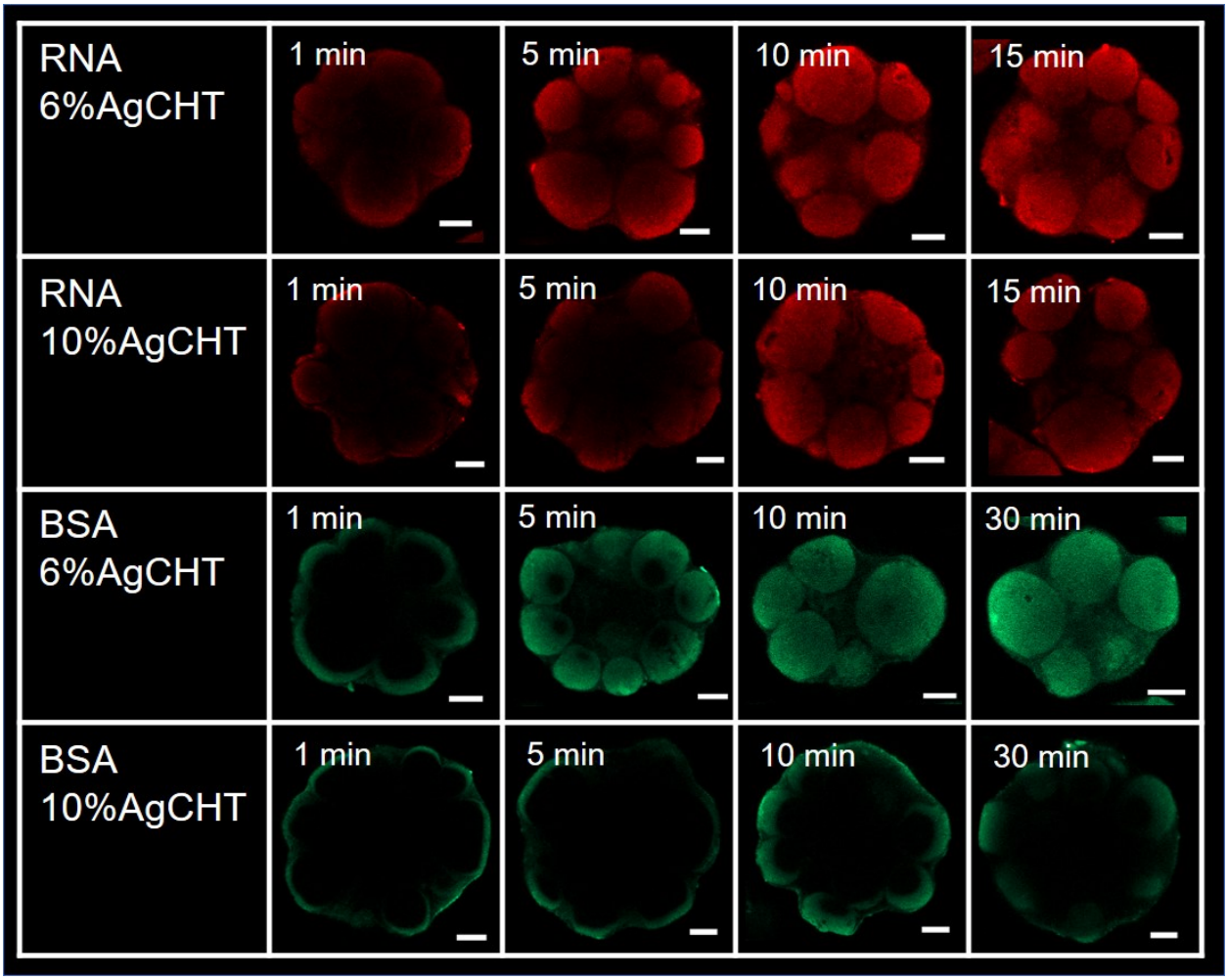

Figure 3.16: CLSM images showing the time course of adsorption of 1.8 mg/mL RNA (top two rows) and 2 mg/mL BSA (bottom two rows) on 6%AgCHT and 10%AgCHT beads. Images are taken in benzyl alcohol. The scale bar in each image is 25 μm.

both nanoparticles are also expected to be essentially completely excluded since their sizes are close to or exceed the effective pore size.

Figure 3.17 shows the breakthrough curves obtained for one component feeds containing 1 mg/mL BSA or 1 mg/mL Tg plotted vs. the ratio of load volume and column volume, V/V_c, in (a) and (c) and vs. the ratio of load volume and volume of CHT particles, V/V_{CHT}, in (b) and (d). The CHT volume was calculated as $V_{CHT} = (1-\epsilon)\phi_{CHT} \times V_c$. As seen in Fig. 3.17a, the BSA binding capacity per unit column volume is much larger for the unencapsulated CHT column than for the 6%AgCHT column as indicated by the horizontal shift of the breakthrough profile. However, as seen in Fig. 3.17b, the two curves come to a much closer agreement when plotted vs. V/V_{CHT}, suggesting that the BSA binding capacity per mL of CHT particles is essentially the same whether the CHT particles are encapsulated or not. Even so, the 6%AgCHT breakthrough curve on the V/V_{CHT} basis is considerably shallower than the CHT-only column. This result stems in large part from the fact that the 6%AgCHT beads are much larger in diameter compared to the CHT particles (105 vs. 40 μm), which, in turn, results in a greater mass transfer resistance and, thus, a shallower breakthrough curve. For the 10%AgCHT column, breakthrough of BSA occurs almost immediately at this residence time, which is consistent with the even larger bead size of this material and with the slower binding kinetics shown in Fig. 3.17b resulting from the smaller effective pore size.

The Tg breakthrough curves (Figs. 3.17c and 3.17d) show that substantial binding occurs on the CHT-only column. However, the binding kinetics is slow (cf. Fig. 3.15) so that the CHT-only breakthrough does not have the characteristic S-shape seen in cases where mass transfer is relatively fast. Conversely, only minimal Tg binding occurs in the 6%AgCHT column and no binding at all appears to occur in the 10%AgCHT column. Both of 6% and 10%AgCHT exclude Tg almost completely so that breakthrough occurs in the column void volume. This result suggests that the AgCHT columns can be used to remove small protein impurities (e.g., BSA with 6%AgCHT or

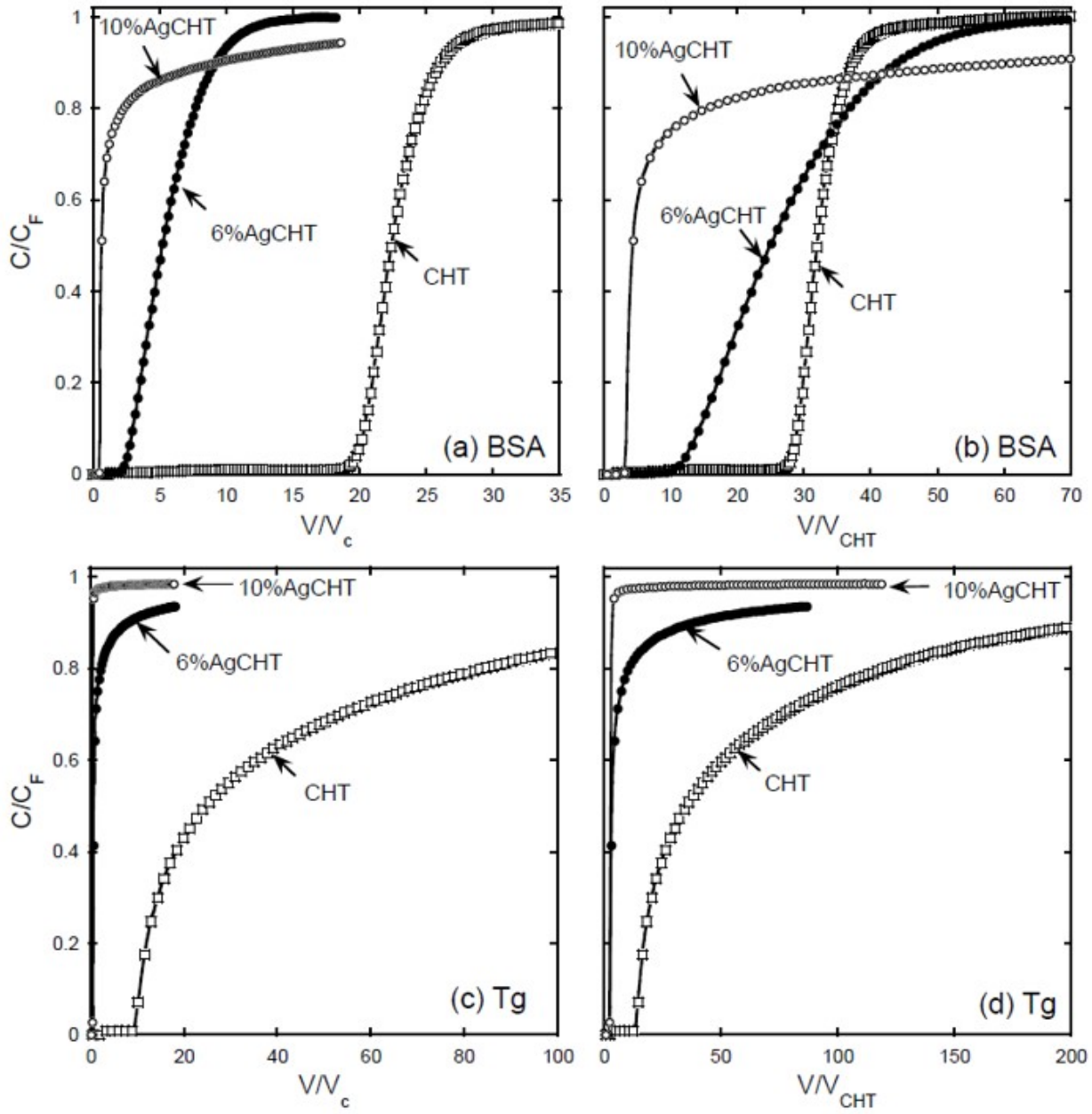

Figure 3.17: One-component breakthrough curves of 1 mg/mL BSA (a and b) and 1 mg/mL Tg (c and d) on CHT, 6%AgCHT, and 10%AgCHT columns at a residence time of 5 min. The curves are plotted in (a) and (c) vs. the ratio of load volume and column volume and in (b) and (d) vs. the ratio of load volume and CHT volume.

smaller proteins with 10%AgCHT) from a Tg feed in a flow-through mode with virtually no loss of Tg.

Figure 3.18 shows the two-component breakthrough curves for mixtures of 30 nm silica nanoparticles with BSA (a) and with RNA (b) for the 6%AgCHT column at a residence time of 5 min compared to the corresponding one-component BSA and RNA breakthrough curves. The mixture experiments are meant to exemplify a hypothetical flow-through purification of a large bioparticle from smaller contaminating proteins or nucleic acids. In both cases, the nanoparticles break through almost immediately mostly at the column void volume, which is marked by the vertical dashed line. Some retention of nanoparticles is evident, however, from the breakthrough curves shown. This is likely due to the relatively broad distribution of nanoparticle radii in the sample used, which spans the range 8-26 nm (Fig. 3.8). Based on the average pore radius of 15.1 nm determined for 6%AgCHT (Table 3.5), some retention of the smaller nanoparticles in the sample can, in fact, be expected. For both the BSA/NP mixture and for the RNA/NP mixture the BSA and RNA breakthrough curves are essentially the same as those observed with the corresponding one-component BSA and RNA feeds. Table 3.6 shows the corresponding equilibrium binding capacity (EBC) and dynamic binding capacity (DBC) values obtained by integrating the areas above the BSA and RNA curves. The EBC values are given both per mL of column and per mL of beads. For the RNA/NP mixture, the amount of feed loaded was insufficient to attain saturation. Thus, the calculated EBC is a lower-bound estimate. As seen in Table 3.6, there is substantial agreement between capacity values obtained for each one-component and two-component feeds indicating that the presence of the nanoparticles does not affect BSA and RNA binding. The EBC values expressed in terms of mL of beads are also in close agreement with the isotherm values shown in Figs. 3.14a and 3.14b.

The results in Fig. 3.18 show that an early breakthrough occurs for RNA (Fig. 3.18b) whether alone or with the RNA/NP mixture, but not for BSA (Fig. 3.18a). To understand the underlying reasons

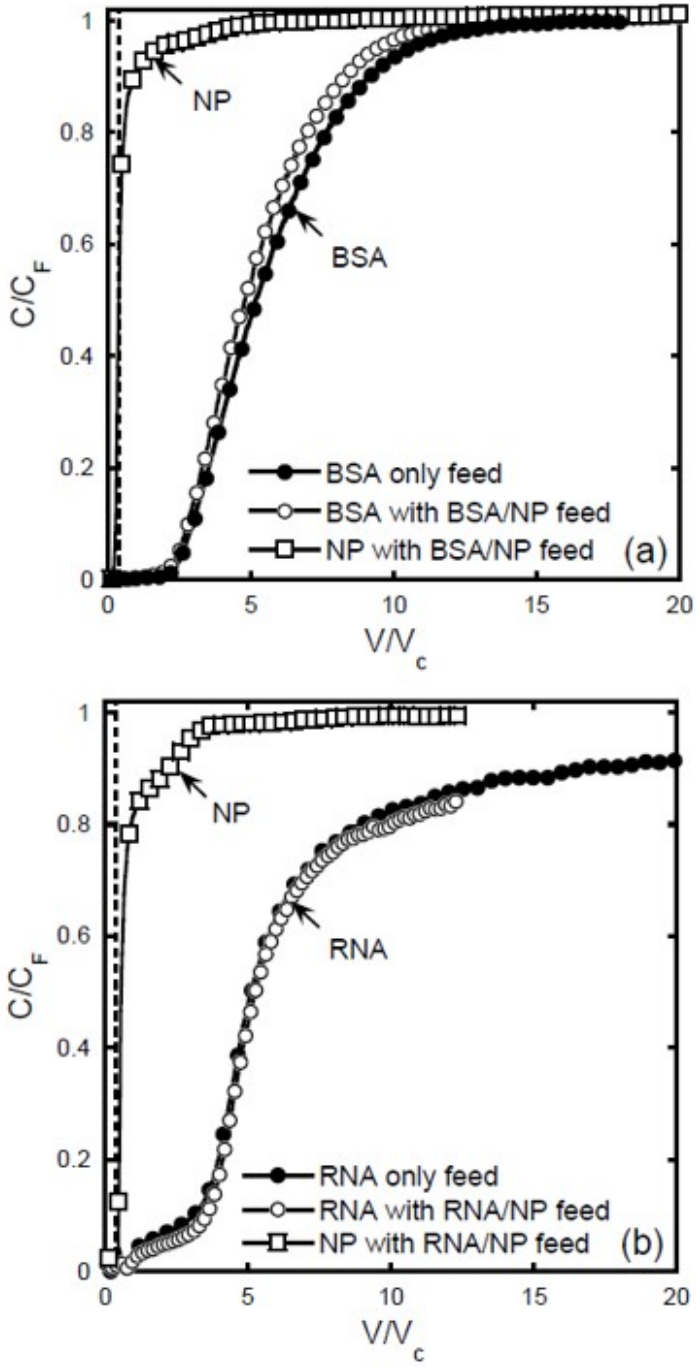

Figure 3.18: Comparison of one-component BSA and RNA breakthrough curves with two-component breakthrough curves obtained with feed mixtures containing 30 nm nanoparticles for the 6%AgCHT column at a residence time of 5 min. (a) BSA and BSA/NP feed mixture; (b) RNA and RNA/NP feed mixture. All feed concentrations were 1 mg/mL for each component The dashed line marks the column extraparticle void volume, $\epsilon = 0.42$.

Table 3.6: Equilibrium binding capacity (EBC) and dynamic binding capacity (DBC) at 10% breakthrough of BSA and RNA obtained for one-component BSA and RNA feeds and for feed mixtures of BSA and RNA with 30 nm nanoparticles for the 6%AgCHT column at a 5 min residence time. The concentration of each feed component was 1 mg/mL.

Feed	EBC (mg/mL column)	EBC (mg/mL beads)	DBC (mg/mL column)
BSA	5.7	9.8	DBC
BSA/NP mixture	5.3	9.0	2.9
RNA	7.5	13	3.1
RNA/NP mixture	>7	>12	3.5

for the early RNA breakthrough, we collected 0.2 CV fractions along the breakthrough curve and analyzed each fraction to determine the A260/A280 ratio as well as the size distribution by UPLC SEC as described in Section 3.3.1. We also analyzed the eluate from the column obtained with the phosphate gradient described in Section 3.3.2.2 The results of these analyses, given in Table 3.7 and Fig. 3.19, show that fractions collected between 0 and 3 CV (Fig. 3.18b) had A260/A280 substantially higher than the feed value. Moreover, they contained species with molecular size much smaller than the feed. Taken together, these results indicate that the early breakthrough behavior is caused by the presence of unbound or weakly-bound species present in the RNA sample. Fractions collected between 5 and 20 CV as well had the eluted RNA had A260/A280 values and molecular size consistent with the bulk of the RNA feed.

A final consideration regards the recovery of the bound proteins upon eluting the saturated columns with the phosphate gradient described in Section 3.3.2.2. Recoveries were calculated from the elution peak for the runs with one-component BSA and Tg feeds and with the BSA/30 nm nanoparticles feed. The results, shown in Table 3.8, show that BSA and Tg recoveries were nearly quantitative even after multiple runs loading BSA, Tg, and RNA to complete saturation and eluting indicating that the elution procedure used was effective and did not impact the column performance in subsequent runs. The similarity between the results for the CHT-only columns and those obtained with the AgCHT columns also indicates that the agarose encapsulation does not impact recovery.

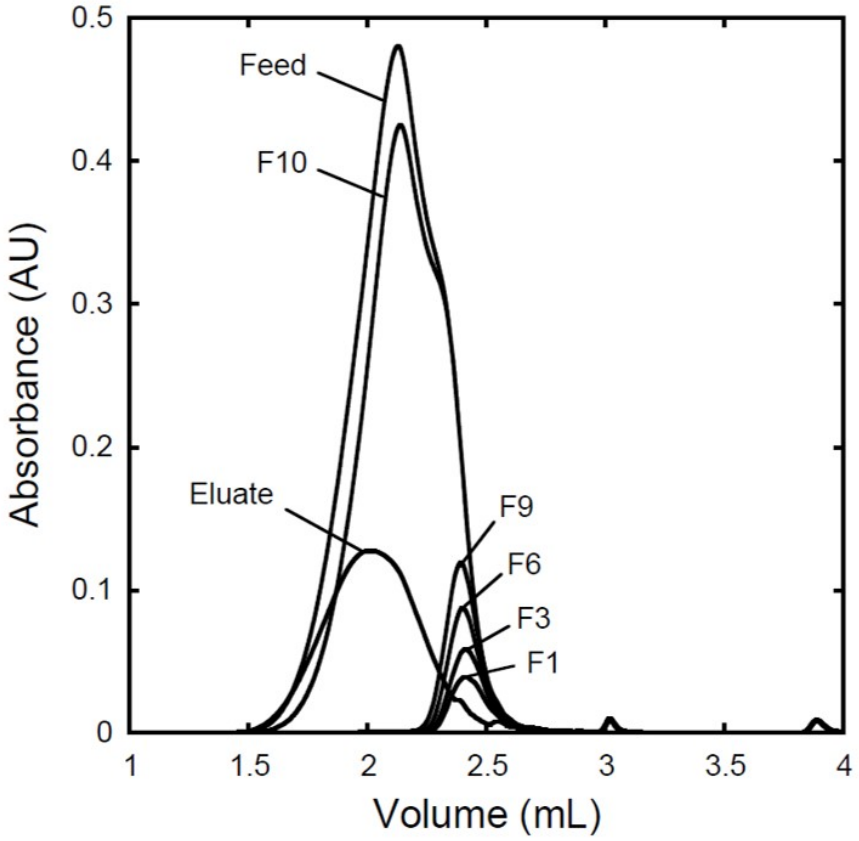

Figure 3.19: UPLC-SEC of the RNA feed, eluate, and fractions shown in Table 3.7. Analysis conditions are the same as in Fig. 3.8.

Table 3.7: Spectrophotometric analyses of fractions collected from the one-component RNA breakthrough run in Fig. 3.18b.

Fraction (CV)	A260	A280	Relative RNA concentration based on A260, C/C_F
Feed	20.1	2.17	1.00
1 (1.3)	0.86	2.29	0.043
2 (1.5)	1.00	2.29	0.050
3 (1.7)	1.15	2.27	0.057
4 (1.9)	1.25	2.27	0.062
5 (2.1)	1.38	2.27	0.069
6 (2.3)	1.52	2.25	0.076
7 (2.5)	1.70	2.26	0.084
8 (2.7)	1.87	2.25	0.093
9 (2.9)	2.12	2.25	0.11
10 (3.1 to 20)	17.1	2.17	0.85
Eluate	5.93	2.12	0.29

Table 3.8: Percentage recoveries of BSA and Tg for columns saturated with pure BSA, pure Tg, and a BSA/30 nm nanoparticles mixture obtained by elution with a 500 mM phosphate gradient.

	Column		
Feed	CHT only	6%AgCHT	10%AgCHT
Pure BSA (1 mg/mL)	98%	96%	92%
Pure Tg (1 mg/mL)	96%	98%	98%
BSA/30 nm nanoparticles mixture (1 mg/mL each)	NA	92%	NA

Chapter 4 Conclusions and Recommendations

4.1 Polymer-grafted anion exchange adsorbents

Three anion exchange resins functionalized with a range of grafted polymeric surface extender were investigated. The interplay between resin characteristics, such as pore size, polymer-graft length, and protein size was examined. Nuvia HR Q and Nuvia HP Q both contain a moderate degree of polymer content that do not fill the entire pore volume. The base matrix of Nuvia HP Q has pores larger than that of Nuvia HR Q. Nuvia Q contains longer polymer-grafts than Nuvia HR Q and Nuvia HP Q that occupy most of its pore volume. Conversely, UNOSphere Diol Q is a macroporous adsorbent comprised only of the relatively rigid base-matrix formed by acrylamide and vinyl copolymers.

The equilibrium adsorption and kinetics of BSA and Tg were significantly enhanced on the polymer-grafted adsorbents compared to UNOSphere Diol Q. BSA exhibited high binding capacity and fast kinetics for the polymer-grafted resins. Tg demonstrated strong binding affinities at low NaCl concentrations which hindered transport into Nuvia HR Q, Nuvia HP Q, and Nuvia Q. Elevated ionic strengths weakened these interactions resulting in enhanced kinetics and a higher apparent binding capacity than without NaCl. Overall, the polymer-grafted adsorbents demonstrated higher binding capacity and adsorption kinetics than UNOSphere Diol Q.

BSA breakthrough curves obtained for the polymer-grafted resins demonstrated high dynamic binding capacities at low NaCl concentrations that decreased with increasing NaCl concentration. Breakthrough became sharper at elevated NaCl concentrations indicative of rapid adsorption, however the decrease in equilibrium binding capacity heavily outweighed this rapid uptake, resulting in low dynamic binding capacities. On the other hand, for Tg breakthrough, the DBC increased at elevated NaCl concentrations resulting from enhanced adsorption kinetics. These enhanced kinetics are consistent with the CLSM images that demonstrated fast particle saturation at elevated NaCl concentrations.

Consequently, with elevated ionic strengths higher column utilization can be achieved.

The industrial relevant aspect of these resins involves their ability to perform efficient separations, therefore, two-component breakthrough of mixtures containing BSA and Tg is of significant interest. For UNOSphere Diol Q, the breakthrough curve followed displacement effects seen on other macroporous adsorbents. Nuvia Q was unable to separate BSA and Tg from a BSA/Tg mixture, thus with its high binding capacity it is more suitable for impurity clearance when the product of interest does not require high selectivity. Nuvia HP Q demonstrated a high BSA overshoot (1.4 $\times$ feed value) suggesting that breakthrough separations of small and large proteins is feasible. At higher NaCl concentrations where Tg undergoes rapid adsorption may provide greater separations.

Transport through the polymer-grafted phase is more complex than pore diffusion. For Nuvia Q Maxwell-Stefan diffusion was found to appropriately describe adsorption into the particle. The counter diffusion of BSA in the polymer-grafts resulted in additional resistances to transport. Since Nuvia HP Q and to a lesser extent Nuvia HR Q contain polymer-grafts within large open pores, a parallel pore and solid diffusion model is most likely required. Since pore diffusion at relevant concentrations is unhindered by counter diffusion, a single file diffusion model for the polymer-grafted phase is unsuitable. Polymer-grafted adsorbents possess enhanced adsorption kinetics and binding capacities compared to their macroporous analogues. As a result of these enhanced adsorption kinetics, careful consideration of the polymer-graft length, pore size, and buffer composition is necessary to optimize separations contingent on the size of the desired product.

Future work should include further characterization of protein transport into polymer-grafted adsorbents. Breakthrough experiments of BSA/Tg mixtures at 0 and 100 mM NaCl can help further understand how protein size and binding strength affect breakthrough separations. Binding strength increases at low NaCl concentrations which may severely hinder Tg adsorption resulting in early breakthrough

while BSA undergoes rapid adsorption. This effect would most likely be pronounced for Nuvia HR Q and Nuvia Q which have relatively low and almost no free pore volume, respectively. Conversely, binding strength weakens at high NaCl concentrations, therefore Tg adsorption is rapid and displacement of BSA can occur rapidly. Further understanding the interplay of protein size, pore size and binding strength, and therefore NaCl concentration, in two-component separations is necessary to optimize separations.

Finally, work should include further characterization of the transport mechanism in the partially polymer-grafted adsorbents, Nuvia HR Q and Nuvia HP Q. Additional batch uptake experiments over a range of both high and load protein concentrations are necessary to determine effective pore and solid diffusivities. Once these values are estimated, a parallel pore and surface diffusion model may describe one- and two-component breakthrough.

4.2 Agarose encapsulated ceramic hydroxyapatite

This work has demonstrated that encapsulating whole CHT particles in agarose beads results in materials that are suitable for the removal of smaller proteins and nucleic acid impurities from large proteins or nanoparticles. The agarose prevents adsorption of the larger species to the encapsulated CHT without impacting the ability of smaller species to diffuse and bind.

BSA and Tg were examined to ascertain the ability of CHT to adsorb small acidic proteins to ensure viability of agarose-encapsulated CHT particles for flow-through separations. The adsorption of Tg and BSA on CHT is consistent with a complexation mechanism. Importantly, binding is modulated by displacing salts such as sodium phosphate. The use of sodium chloride alone is insufficient to inhibit these interactions, contrary to normal ion exchange interaction. Sodium chloride was shown to increase equilibrium binding capacities for concentrations up to 250 mM and 500 mM for BSA

and Tg respectively. This can be attributed to sodium chloride shielding both BSA and Tg from the repulsive electrostatic interactions of phosphate groups. High equilibrium binding capacities were observed even at 1000 mM NaCl concentrations. BSA demonstrated fast adsorption kinetics for one- and two-component adsorption. Consequently, CHT is suitable for the capture of negatively charged impurities at high ionic strengths in the absence of displacing ions (e.g, Ca^{2+}). Equilibrium adsorption of two-component mixtures of Tg and BSA demonstrated some competitive adsorption between the two species with both retaining high adsorption capacities.

The agarose largely eliminated binding to the external bead surface. An advantage of the method used to prepare the composite beads is that the size exclusion properties can be adjusted by selecting the agarose content. 6%AgCHT is ideal for the flow-through based removal of impurities up to 5 nm whereas the 10%AgCHT is suitable only for smaller impurities. The BSA and RNA binding capacities obtained for our composite materials are comparable to those observed for CHT-only when based on the volume of CHT particles. On the other hand, because of the limited volume fraction of CHT particles within the beads, the binding capacities become relatively small when based on the total bead volume. Nevertheless, for BSA, the capacity per mL of column is better than that reported for a CHT-agarose composite based on the encapsulation of hydroxyapatite microcrystals and comparable to that reported for Capto Core 700. Capacity improvements can be obtained by increasing the CHT content of the composite beads by reducing the CHT particle size. The emulsion method allows the preparation of composites encapsulating different types of adsorbent particles such as other CHT types and ion exchange adsorbents.

Future work should investigate the ability to encapsulate high capacity adsorbents such as polymer-grafted adsorbents in order to substantially increase the adsorption capacity of the resins on a bead volume basis. Similarly, microcrystalline CHT can be encapsulated to synthesize smaller more homogeneous beads; smaller more homogeneous beads have numerous advantages. The first is a

decrease in mass transfer resistances. Secondly, diffusion models, such as pore diffusion, can be applied to predict separations. Predicting an average diffusivity for heterogeneous stationary phases can be difficult. For core-shell particles such as Capto core 700, the mass transfer resistances are in series and can be analytically expressed. Encapsulated materials, such as those produced in this work, require a lumped effective diffusion coefficient accounting for diffusion through both the agarose bead and the encapsulated CHT. Further investigations should include applying heterogeneous diffusion models to allow for better predictions of small molecule and protein adsorption onto the materials. On the other hand, alternative synthesis approaches can be investigated to produce core-shell particles similar to "lid" beads. Microfluidic-based or membrane-based emulsification methods are a promising avenue for manufacturing encapsulated particles in a thin layer of agarose. Consequently, these agarose-coated CHT composite-particles would be analogous to Capto Core 400 and 700.

Appendix A

The thermodynamic factors for a binary system where Maxwell-Stefan diffusion is dominant can be written as:

$$\Gamma = \begin{bmatrix} \left(\frac{q_A}{RT}\frac{\partial \mu_A}{\partial q_a}\right) & \left(\frac{q_A}{RT}\frac{\partial \mu_A}{\partial q_b}\right) \\ \left(\frac{q_b}{RT}\frac{\partial \mu_b}{\partial q_a}\right) & \left(\frac{q_b}{RT}\frac{\partial \mu_b}{\partial q_b}\right) \end{bmatrix} \tag{4.1}$$

where μis the chemical potential with the subscripts A and B represent the two species in the mixture. For an ideal solution, the chemical potential can be related to fluid phase concentration by:

$$\mu_i = \mu_i^0 + RT \ln C_i \tag{4.2}$$

Accordingly, thermodynamic factors can be related to the slope of the adsorption isotherm by the following [101]:

$$\frac{q_i}{RT}\frac{\partial \mu_i}{\partial q_j} = \frac{q_{i,sat}}{q_{j,sat}}\frac{q_i}{C_i}\frac{\partial C_i}{\partial q_j} \tag{4.3}$$

The resulting matrix of thermodynamic factors is thus:

$$\Gamma = \begin{bmatrix} \left(\frac{q_A}{C_A}\frac{\partial C_A}{\partial q_A}\right) & \left(\frac{q_{B,sat}}{q_{A,sat}}\frac{q_A}{C_A}\frac{\partial C_A}{\partial q_B}\right) \\ \left(\frac{q_{A,sat}}{q_{B,sat}}\frac{q_B}{C_B}\frac{\partial C_b}{\partial q_A}\right) & \left(\frac{q_B}{C_B}\frac{\partial C_B}{\partial q_B}\right) \end{bmatrix} \tag{4.4}$$

where from the fluid phase concentration is related to adsorbed phase concentration by the discount factor isotherm [96]:

$$C_A = \frac{q_A}{K_A\left(q_{m,A} - q_A - \zeta q_B\right)} \tag{4.5a}$$

$$C_B = \frac{q_B}{K_B\left(q_{m,B} - q_A - q_B\right)} \tag{4.5b}$$

with the resulting partial derivatives being:

$$\frac{\partial C_A}{\partial q_A} = \frac{q_{m,A} - \zeta q_B}{K_A\left(q_{m,A} - q_A - \zeta q_B\right)^2} \tag{4.6a}$$

$$\frac{\partial C_A}{\partial q_B} = \frac{\zeta q_A}{K_A\left(q_{m,A} - q_A - \zeta q_B\right)^2} \tag{4.6b}$$

$$\frac{\partial C_B}{\partial q_A} = \frac{q_{m,B}}{K_B\left(q_{m,B} - q_A - q_B\right)^2} \tag{4.6c}$$

$$\frac{\partial C_B}{\partial q_B} = \frac{q_B}{K_B\left(q_{m,B} - q_A - q_B\right)^2} \tag{4.6d}$$

The resulting thermodynamic factors are:

$$\Gamma_{AA} = \frac{q_{m,A} - \zeta q_B}{q_{m,A} - q_A - \zeta q_B} \tag{4.7a}$$

$$\Gamma_{AB} = \frac{q_{B,sat}}{q_{A,sat}} \frac{\zeta q_a}{q_{m,A} - q_A - \zeta q_B} \tag{4.7b}$$

$$\Gamma_{BA} = \frac{q_{A,sat}}{q_{B,sat}} \frac{q_{m,B}}{q_{m,B} - q_A - q_B} \tag{4.7c}$$

$$\Gamma_{BB} = \frac{q_b}{q_{m,B} - q_A - q_B} \tag{4.7d}$$

The Maxwell-Stefan diffusivities for a binary system have previously been derived by Kapteijn [101]:

$$B = \begin{bmatrix} \left(\frac{1}{q_{A,sat} D_A(q_A, q_B)} + \frac{q_B}{q_{A,sat} q_{B,sat} D_{AB}}\right) & \left(-\frac{q_A}{q_{A,sat} q_{B,sat} D_A(q_A, q_B)}\right) \\ \left(-\frac{q_B}{q_{A,sat} q_{B,sat} D_A(q_A, q_B)}\right) & \left(\frac{1}{q_{B,sat} D_A(q_A, q_B)} + \frac{\theta_A}{q_{A,sat} q_{B,sat} D_{AB}}\right) \end{bmatrix} \tag{4.8}$$

where, D_{AB} is the cross-diffusivity term that represents counter exchange and interactions between the proteins that hinder diffusion, and θ is protein surface coverage. It should be noted that for molecules of different sizes or for protein-protein interactions that the cross diffusivity term, DAB, cannot be neglected and can be related to the zero loading diffusivities, $D_{s,i} = D_i(0)$ by the expression [101]:

$$D_{AB}(q_A, q_B) = D_A(0)^{\left(\frac{\theta_A}{\theta_A + \theta_B}\right)} \times D_B(0)^{\left(\frac{\theta_B}{\theta_A + \theta_B}\right)} \tag{4.9}$$

These resulting expressions can then be plugged into eq. 13 and simulated in MATLAB using ode15s with 50 radial discretization points.

References

[1] O. Leavy. Therapeutic antibodies: Past, present and future. Nat. Rev. Immunol. 10 (2010) 297.

[2] D. M. Ecker, S. D. Jones, H. L. Levine. The therapeutic monoclonal antibody market. mAbs 7 (2015) 9–14.

[3] G. Walsh. Biopharmaceutical benchmarks 2018. Nat. Biotechnol 36 (2018) 1136–1145.

[4] K. E. Jones, N. G. Patel, M. A. Levy, A. Storeygard, D. Balk, J. L. Gittleman, P. Daszak. Global trends in emerging infectious diseases. Nat. 451 (2008) 990–993.

[5] K. F. Smith, M. Goldberg, S. Rosenthal, L. Carlson, J. Chen, C. Chen, S. Ramachandran. Global rise in human infectious disease outbreaks. J. R. Soc. Interface 11 (2014) 1–6.

[6] A. Philippidis. *Top 8 best-selling COVID-19 vaccines and drugs of Q1 2021*. 2021. URL: https://www.genengnews.com/a-lists/top-8-best-selling-covid-19-vaccines-and-drugs-of-q1-2021/.

[7] E. Langer, R. Rader. Biopharmaceutical Manufacturing: historical and future trends in titers, yields, and efficiency in commercial-scale bioprocessing. Bioprocess. J. 13 (2015) 47–54.

[8] R. Rader, E. Langer. Biopharmaceutical Manufacturing: current titers and yields in commercial-scale microbial bioprocessing. Bioprocess. J. 14 (2015) 51–55.

[9] W. C. Yang, D. F. Minkler, R. Kshirsagar, T. Ryll, Y.-M. Huang. Concentrated fed-batch cell culture increases manufacturing capacity without additional volumetric capacity. J. Biotechnol. 217 (2016) 1–11.

[10] P. Gronemeyer, R. Ditz, J. Strube. Trends in upstream and downstream process development for antibody manufacturing. Bioeng. 1 (2014) 188–212.

[11] D. Low, R. O'Leary, N. S. Pujar. Future of antibody purification. J. Chromatogr. B 848 (2007) 48–63.

[12] B. Kelley. Very large scale monoclonal antibody purification: the case for conventional unit operations. Biotechnol. Progr. 23 (2007) 995–1008.

[13] A. A. Shukla, J. Thömmes. Recent advances in large-scale production of monoclonal antibodies and related proteins. Trends Biotechnol. 28 (2010) 253–261.

[14] S. Hober, K. Nord, M. Linhult. Protein A chromatography for antibody purification. J. Chromatogr. B 848 (2007) 40–47.

[15] P. A. Marichal-Gallardo, M. M. Álvarez. State-of-the-art in downstream processing of monoclonal antibodies: Process trends in design and validation. Biotechnol. Progr. 28 (2012) 899–916.

[16] A. A. Shukla, B. Hubbard, T. Tressel, S. Guhan, D. Low. Downstream processing of monoclonal antibodies-Application of platform approaches. J. Chromatogr. B 848 (2007) 28–39.

[17] C. L. Effio, J. Hubbuch. Next generation vaccines and vectors: Designing downstream processes for recombinant protein-based virus-like particles. Biotechnol. J. 10 (2015) 715–27.

[18] L. H. Lua, N. K. Connors, F. Sainsbury, Y. P. Chuan, N. Wibowo, A. P. Middelberg. *Bioengineering virus-like particles as vaccines*. 2014.

[19] R. Martins, J. A. Queiroz, F. Sousa. Ribonucleic acid purification. J. Chromatogr. A 1355 (2014) 1–14.

[20] J. Louten. *Virus Structure and Classification*. Academic Press, 2016 19–29.

[21] P. Gagnon. Technology trends in antibody purification. J. Chromatogr. A 1221 (2012) 57–70.

[22] E. X. P. Almodóvar, Y. Tao, G. Carta. Protein adsorption and transport in cation exchangers with a rigid backbone matrix with and without polymeric surface extenders. Biotechnol. Progr. 27 (2011) 1264–1272.

[23] A. Jungbauer. Chromatographic media for bioseparation. J. Chromatogr. A 1065 (2005) 3–12.

[24] L. L. Yu, S. P. Tao, X. Y. Dong, Y. Sun. Protein adsorption to poly(ethylenimine)-modified Sepharose FF: I. A critical ionic capacity for drastically enhanced capacity and uptake kinetics. J. Chromatogr. A 1305 (2013) 76–84.

[25] P. E. Gustavsson, R. Lemmens, T. Nyhammar, P. Busson, P.-O. Larsson. Purification of plasmid DNA with a new type of anion-exchange beads having a non-charged surface. J. Chromatogr. A 1038 (2004) 131–140.

[26] M. Degerman, N. Jakobsson, B. Nilsson. Constrained optimization of a preparative ion-exchange step for antibody purification. J. Chromatogr. A 1113 (2006) 92–100.

[27] J. M. Reck, T. M. Pabst, A. K. Hunter, X. Wang, G. Carta. Adsorption equilibrium and kinetics of monomer-dimer monoclonal antibody mixtures on a cation exchange resin. J. Chromatogr. A 1402 (2015) 46–59.

[28] G. Carta, A. Jungbauer. *Protein chromatography: process development and scale-up*. John Wiley & Sons, 2010 5–8.

[29] Y. Tao, E. X. P. Almodovar, G. Carta, G. Ferreira, D. Robbins. Adsorption kinetics of deamidated antibody variants on macroporous and dextran-grafted cation exchangers. III. Microscopic studies. J. Chromatogr. A 1218 (2011) 8027–8035.

[30] L. K. Kimerer, T. M. Pabst, A. K. Hunter, G. Carta. Chromatographic behavior of bivalent bispecific antibodies on cation exchange columns. I. Experimental observations and phenomenological model. J. Chromatogr. A 1601 (2019) 121–132.

[31] M. Zhu, G. Carta. Adsorption of polyethylene-glycolated bovine serum albumin on macroporous and polymer-grafted anion exchangers. J. Chromatogr. A 1326 (2014) 29–38.

[32] C. Wang, L. Wang, X. Geng. Renaturation with simultaneous purification of rhG-CSF from Escherichia coli by ion exchange chromatography. Biomed. Chromatogr. 21 (2007) 1291–1296.

[33] A. M. Lenhoff. Protein adsorption and transport in polymer-functionalized ion-exchangers. J. Chromatogr. A 1218 (2011) 8748–8759.

[34] H. O. Johansson, J. M. Van Alstine. Modeling of protein interactions with surface-grafted charged polymers. Correlations between statistical molecular modeling and a mean field approach. Langmuir 22 (2006) 8920–8930.

[35] W. Müller. New ion exchangers for the chromatography of biopolymers. J. Chromatogr. A 510 (1990) 133–140.

[36] M. C. Stone, G. Carta. Protein adsorption and transport in agarose and dextran-grafted agarose media for ion exchange chromatography. J. Chromatogr. A 1216 (2007) 4465–4474.

[37] L.-L. Yu, S.-P. Tao, X.-Y. Dong, Y. Sun. Protein adsorption to poly(ethylenimine)-modified Sepharose FF: I. a critical ionic capacity for drastically enhanced capacity and uptake kinetics. J. Chromatogr. A 1305 (2013) 76–84.

[38] L. Yu, L. Gong, S. Bai, Y. Sun. Surface DEAE groups facilitate protein transport on polymer chains in DEAE-modified-and-DEAE-dextran-grafted resins. AlChE J. 62 (2016) 3812–3819.

[39] L. L. Yu, Q. H. Shi, Y. Sun. Effect of dextran layer on protein uptake to dextran-grafted adsorbents for ion-exchange and mixed-mode chromatography. J. Sep. Sci. 34 (2011) 2950–2959.

[40] J. E. Basconi, G. Carta, M. R. Shirts. Multiscale modeling of protein adsorption and transport in macroporous and polymer-grafted ion exchangers. AlChE J. 60 (2014) 3888–3901.

[41] J. E. Basconi, G. Carta, M. R. Shirts. Effects of polymer graft properties on protein adsorption and transport in ion exchange chromatography: A multiscale modeling study. Langmuir 31 (2015) 4176–4187.

[42] J. E. Basconi, G. Carta, M. R. Shirts. Effects of protein properties on adsorption and transport in polymer-grafted ion exchangers: A multiscale modeling study. AlChE J. 63 (2017) 4564–4575.

[43] S. Gautam, K. C. Loh. Immunoglobulin-M purification - challenges and perspectives. Biotechnol. Adv. 29 (2011) 840–849.

[44] C. Acquah, C. K. Moy, M. K. Danquah, C. M. Ongkudon. Development and characteristics of polymer monoliths for advanced LC bioscreening applications: A review. J. Chromatogr. B 1015-1016 (2016) 121–134.

[45] A. Š. Podgornik, S. Yamamoto, M. Ž. Peterka, N. L. Krajnc. Fast separation of large biomolecules using short monolithic columns. J. Chromatogr. B 927 (2013) 80–89.

[46] Y. Wu, J. Simons, S. Hooson, D. Abraham, G. Carta. Protein and virus-like particle adsorption on perfusion chromatography media. J. Chromatogr. A 1297 (2013) 96–105.

[47] R. M. Montesinos-Cisneros, A. Lucero-Acuña, J. Ortega, R. Guzmán, A. Tejeda-Mansir. Breakthrough performance of large proteins on ion-exchange membrane columns. Biotechnol. Appl. Biochem. 48 (2007) 117.

[48] R. Ghosh. Protein separation using membrane chromatography : opportunities and challenges. J. Chromatogr. A 952 (2002) 13–27.

[49] A. Zöchling, R. Hahn, K. Ahrer, J. Urthaler, A. Jungbauer. Mass transfer characteristics of plasmids in monoliths. Sep. Purif. Technol. 27 (2004) 819–27.

[50] R. K. Lewus, G. Carta. Binary protein adsorption on gel-composite ion-exchange media. AlChE J. 45 (1999) 512–522.

[51] E. X. Perez-Almodovar, Y. Wu, G. Carta. Multicomponent adsorption of monoclonal antibodies on macroporous and polymer grafted cation exchangers. J. Chromatogr. A 1264 (2012) 48–56.

[52] Y. Tao, N. Chen, G. Carta, G. Ferreira, D. Robbins. Modeling multicomponent adsorption of monoclonal antibody charge variants in cation exchange columns. AlChE J. 58 (2012) 2503–2511.

[53] A. Tiselius, S. Hjertén, Ö. Levin. Protein chromatography on calcium phosphate columns. Arch. Biochem. Biophys. 65 (1956) 132–155.

[54] M. J. Gorbunoff. The interaction of proteins with hydroxyapatite: II. Role of acidic and basic groups. Anal. Biochem. 136 (1984) 433–439.

[55] M. J. Gorbunoff. The interaction of proteins with hydroxyapatite: I. Role of protein charge and structure. Anal. Biochem. 136 (1984) 425–432.

[56] L. J. Cummings, M. A. Snyder, K. Brisack. Chapter 24 Protein Chromatography on Hydroxyapatite Columns. Methods Enzymol. 463 (2009) 387–404.

[57] M. Saito, Y. Kurosawa, T. Okuyama. Purification of anti-japanese encephalitis virus monoclonal antibody by ceramic hydroxyapatite chromatography without proteins a and g. Hybridoma 31 (2012) 68–71.

[58] J. C. Cook. *Process for purifying papillomavirus virus-like particles*. 2003.

[59] W. Qu, M. Wang, Y. Wu, Y. Lv, Q. Wang, R. Xu. Calcium-ion-modulated ceramic hydroxyapatite resin for the scalable purification of recombinant Adeno-Associated Virus serotype 9. J. Chromatogr. B 990 (2015) 15–22.

[60] E. Schmoeger, C. Paril, R. Tscheliessnig, A. Jungbauer. Adsorption of plasmid DNA on ceramic hydroxyapatite chromatographic materials. J. Sep. Sci. 33 (2010) 3125–3136.

[61] Y. Wang, G. Carta. Competitive binding of monoclonal antibody monomer-dimer mixtures on ceramic hydroxyapatite. J. Chromatogr. A 1587 (2018) 136–145.

[62] Y. Wang, G. Carta. Separation of monoclonal antibody monomer-dimer mixtures by gradient elution with ceramic hydroxyapatite. J. Chromatogr. A 1629 (2020) 461465.

[63] Y. Wang, G. Carta. Dynamics of competitive binding and separation of monoclonal antibody monomer-dimer mixtures in ceramic hydroxyapatite columns. J. Chromatogr. A 1609 (2019) 460504.

[64] M. F. X. Lee, E. S. Chan, B. T. Tey. Negative chromatography: Progress, applications and future perspectives. Process Biochem. 49 (2014) 1005–1011.

[65] G. H. L. Sciences. *Capto Core 700 multimodal chromatography resin*. 2020.

[66] S. T. Mundle, M. Kishko, R. Groppo, J. DiNapoli, J. Hamberger, B. McNeil, H. Kleanthous, M. Parrington, L. Zhang, S. F. Anderson. Core bead chromatography for preparation of highly pure, infectious respiratory syncytial virus in the negative purification mode. Vaccine 34 (2016) 3690–3696.

[67] M. Zaveckas, K. Goda, D. Ziogiene, A. Gedvilaite. Purification of recombinant trichodysplasia spinulosa–associated polyomavirus VP1-derived virus-like particles using chromatographic techniques. J. Chromatogr. B 1090 (2018) 7–13.

[68] K. Reiter, P. P. Aguilar, V. Wetter, P. Steppert, A. Tover, A. Jungbauer. Separation of virus-like particles and extracellular vesicles by flow-through and heparin affinity chromatography. J. Chromatogr. A 1588 (2019) 77–84.

[69] C. Sánchez-Trasviña, P. Fuks, C. Mushagasha, L. Kimerer, K. Mayolo-Deloisa, M. Rito-Palomares, G. Carta. Structure and functional properties of Capto™ Core 700 core-shell particles. J. Chromatogr. A 1621 (2020).

[70] X. Mi, P. Fuks, S. c. Wang, M. A. Winters, G. Carta. Protein adsoprotein adsorption on core-shell particles: Comparison of Capto™ Core 400 and 700 resins. J. Chromatogr. A 1651 (2021) 462314.

[71] M. A. Fernandez, G. Carta. Characterization of protein adsorption by composite silica-polyacrylamide gel anion exchangers. I. Equilibrium and mass transfer in agitated contactors. J. Chromatogr. A 746 (1996) 169–183.

[72] M. A. Fernandez, W. S. Laughinghouse, G. Carta. Characterization of protein adsorption by composite silica-polyacrylamide gel anion exchangers. II. Mass transfer in packed columns and predictability of breakthrough behavior. J. Chromatogr. A 746 (1996) 185–198.

[73] L. E. Weaver, G. Carta. Protein adsorption on cation exchangers: Comparison of macroporous and gel-composite media. Biotechnol. Progr. 12 (1996) 342–355.

[74] R. K. Lewus, F. H. Altan, G. Carta. Protein adsorption and desorption on gel-filled rigid particles for ion exchange. Ind. Eng. Chem. Res. 37 (1998) 1079–1087.

[75] M. C. Stone, G. Carta. Patterns of protein adsorption in chromatographic particles visualized by optical microscopy. J. Chromatogr. A 1160 (2007) 206–214.

[76] B. D. Bowes, A. M. Lenhoff. Protein adsorption and transport in dextran-modified ion-exchange media. III. Effects of resin charge density and dextran content on adsorption and intraparticle uptake. J. Chromatogr. A 1218 (2011) 7180–7188.

[77] E. X. Perez Almodovar, B. Glatz, G. Carta. Counterion effects on protein adsorption equilibrium and kinetics in polymer-grafted cation exchangers. J. Chromatogr. A 1253 (2012) 83–93.

[78] Y. Tao, G. Carta, G. Ferreira, D. Robbins. Adsorption of deamidated antibody variants on macroporous and dextran-grafted cation exchangers: I. Adsorption equilibrium. J. Chromatogr. A 1218 (2011) 1519–1529.

[79] Y. Tao, G. Carta, G. Ferreira, D. Robbins. Adsorption of deamidated antibody variants on macroporous and dextran-grafted cation exchangers: II. Adsorption kinetics. J. Chromatogr. A 1218 (2011) 1530–1537.

[80] X. Li, Y. Liu, Y. Sun. Alginate-grafted Sepharose FF : A novel polymeric ligand-based cation exchanger for high-capacity protein chromatography. Biochem. Eng. J. 126 (2017) 50–57.

[81] Q. Wang, L. Yu, Y. Sun. Grafting glycidyl methacrylate to Sepharose gel for fabricating high-capacity protein anion exchangers. J. Chromatogr. A 1443 (2016) 118–125.

[82] L. Van Den Broeke, R. Krishna. Experimental verification of the Maxwell-Stefan theory for micropore diffusion. Chem. Eng. Sci. 50 (1995).

[83] Y. Sun, K. Yang. Analysis of mass transport models based on Maxwell-Stefan theory and Fick's law for protein uptake to porous anion exchanger. Sep. Purif. Technol. 60 (2008) 180–189.

[84] K. Yang. Dynamic binary protein adsorption in ion-exchange media depicted with a parallel diffusion model derived from Maxwell-Stefan theory. Chem. Eng. Sci. 139 (2016) 163–172.

[85] M. Zhu, P. Fuks, G. Carta. Protein adsorption in anion exchange resins – effects of polymer grafting, support structure porosity, and protein size. J. Chem. Technol. Biotechnol. 93 (2018) 1948–1958.

[86] R. D. Seader J.D. Henley E.J. *Separation process principles*. 2011.

[87] A. R. Ubiera, G. Carta. Radiotracer measurements of protein mass transfer: kinetics in ion exchange media. Biotechnol. J. 1 (2006) 665–74.

[88] C. a. Brooks, S. M. Cramer. Steric mass-action ion exchange: Displacement profiles and induced salt gradients. AlChE J. 38 (1992) 1969–1978.

[89] W. Kopaciewicz, M. Rounds, J. Fausnaugh, F. Regnier. Retention model for high-performance ion-exchange chromatography. J. Chromatogr. A 266 (1983) 3–21.

[90] D. M. Ruthven. *Principles of Adsorption and Adsorption Processes*. John Wiley & Sons, 1984 433.

[91] G. Carta, A. Ubiera. Particle-size distribution effects in batch adsorption. AlChE J. 49 (2003) 3066–3073.

[92] M. D. Levan, D. Ph, C. Engineering, C. M. Yon, D. Associate, D. Plaines. *Perry's chemical engineers' handbook*. Vol. 45. 2013 45–4393.

[93] E. Müller. Comparison between mass transfer properties of weak-anion-exchange resins with graft-functionalized polymer layers and traditional ungrafted resins. J. Chromatogr. A 1006 (2003) 229–240.

[94] K. Yang, Y. Sun. Structured parallel diffusion model for intraparticle mass transport of proteins to porous adsorbent. Biochem. Eng. J. 37 (2007) 298–310.

[95] C. Martin, G. Iberer, A. Ubiera, G. Carta. Two-component protein adsorption kinetics in porous ion exchange media. J. Chromatogr. A 1079 (2005) 105–115.

[96] T. Gu, G. ? Tsai, G. T. Tsao. Multicomponent adsorption and chromatography with uneven saturation capacities. AlChE J. 37 (1991) 1333–1340.

[97] A. Creasy, J. Reck, T. Pabst, A. Hunter, G. Barker, G. Carta. Systematic interpolation method predicts antibody monomer-dimer separation by gradient elution chromatography at high protein loads. Biotechnol. J. (2018) 1–9.

[98] P. M. Mathias, R. Kumar, J. D. Moyer, J. M. Schork, S. R. Srinivasan, S. R. Auvil, O. Talu. Correlation of multicomponent gas adsorption by the dual-site Langmuir model. Application to nitrogen/oxygen adsorption on 5A-zeolite. Ind. Eng. Chem. Res. 35 (1996) 2477–2483.

[99] E. Schirmer, G. Carta. Protein adsorption kinetics in charged agarose gels: effect of agarose content and modeling. AlChE J. 7 (2009) 405–410.

[100] K. Kaczmarski, D. Antos, H. Sajonz, P. Sajonz, G. Guiochon. Comparative modeling of breakthrough curves of bovine serum albumin in anion-exchange chromatography. J. Chromatogr. A 925 (2001) 1–17.

[101] F. Kapteijn, J. A. Moulijn, R. Krishna. The generalized Maxwell-Stefan model for diffusion in zeolites: Sorbate molecules with different saturation loadings. Chem. Eng. Sci. 55 (2000) 2923–2930.

[102] L. J. P. van den Broeke. Simulation of diffusion in zeolitic structures. AlChE J. 41 (1995) 2399–2414.

[103] Z. Ma, R. D. Whitley, N.-H. L. Wang. Pore and surface diffusion in multicomponent adsorption and liquid chromatography systems. AlChE J. 42 (1996) 1244–1262.

[104] A. M. Lenhoff. Multiscale modeling of protein uptake patterns in chromatographic particles. Langmuir 24 (2008) 5991–5995.

[105] E. J. Wilson, C. J. Geankoplis. Liquid mass transfer at very low reynolds numbers in packed beds. Ind. Eng. Chem. Fundam. 5 (1966) 9–14.

[106] T. W. Weber, R. K. Chakravorti. Pore and solid diffusion models for fixed-bed adsorbers. AlChE J. 20 (1974) 228–238.

[107] H. Yoshida, T. Kataoka, D. M. Ruthven. Analytical solution of the breakthrough curve for rectangular isotherm systems. Chem. Eng. Sci. 39 (1984) 1489–1497.

[108] J. A. Roberts, G. Carta. Relationship between HETP measurements and breakthrough curves in short chromatography columns. Biotechnol. Progr. 37 (2021) 1–10.

[109] *HA Ultrogel® - Hydroxyapatite Chromatography Resin*. 2021. URL: https://www.sartorius.com/shop/ww/en/usd/products-process-chromatography-ha-ultrogel%C2%AE---hydroxyapatite-chromatography-resin/c/M_HA_Ultrogel.

[110] C. Fargues, M. Bailly, G. Grevillot. Adsorption of BSA and hemoglobin on hydroxyapatite support: Equilibria and multicomponent dynamic adsorption. Adsorption 4 (1998) 5–16.

[111] T. E. Bankston, L. Dattolo, G. Carta. pH Transients in hydroxyapatite chromatography columns—Experimental evidence and phenomenological modeling. J. Chromatogr. A 1217 (2010) 2123–2131.

[112] P. Gagnon. Improved antibody aggregate removal by hydroxyapatite chromatography in the presence of polyethylene glycol. J. Immunol. Methods 336 (2008) 222–228.

[113] M. Vázquez-Rey, D. A. Lang. Aggregates in monoclonal antibody manufacturing processes. Biotechnol. Bioeng. 108 (2011) 1494–1508.

[114] M. Saito, T. Yoshitake, T. Okuyama. Separation and analysis of charged isomers of monoclonal immunoglobulin G by ceramic hydroxyapatite chromatography. Prep. Biochem. Biotechnol. 46 (2016) 215–221.

[115] A. Jungbauer, C. Tauer, M. Reiter, M. Purtscher, E. Wenisch, F. Steindl, A. Buchacher, H. Katinger. Comparison of protein A, protein G and copolymerized hydroxyapatite for the purification of human monoclonal antibodies. J. Chromatogr. A 476 (1989) 257–268.

[116] R. Giovannini, R. Freitag. Comparison of different types of ceramic hydroxyapatite for the chromatographic separation of plasmid DNA and a recombinant anti-Rhesus D antibody. Bioseparation 9 (2000) 359–368.

[117] E. Schmoeger, C. Paril, R. Tscheliessnig, A. Jungbauer. Adsorption of plasmid DNA on ceramic hydroxyapatite chromatographic materials. J. Sep. Sci. 33 (2010) 3125–3136.

[118] Y. Wang, G. Carta. Rapid and Sensitive Detection of the Interaction of Human Papillomavirus Virus-Like Particles with Yeast Whole Cell RNA Using Biolayer Interferometry. Biotechnol. J. 14 (2019) 1–6.

[119] Y. Wang. "Understanding the chromatographic processing of recombinant human papilomavirus vaccine using ceramic hydroxyapatite". PhD thesis. University of Virginia.

[120] A. Jungbauer, R. Hahn, K. Deinhofer, P. Luo. Performance and characterization of a nanophased porous hydroxyapatite for protein chromatography. Biotechnol. Bioeng. 87 (2004) 364–375.

[121] G. Carta, A. R. Ubiera, T. M. Pabst. Protein mass transfer kinetics in ion exchange media: Measurements and interpretations. Chem. Eng. Technol. 28 (2005) 1252–1264.

[122] M. J. Gorbunoff, S. N. Timasheff. The interaction of proteins with hydroxyapatite: III. Mechanism. Anal. Biochem. 136 (1984) 440–445.

[123] C. Prin, M. C. Bene, B. Gobert, P. Montagne, G. C. Faure. Isoelectric restriction of human immunoglobulin isotypes. Biochim. Biophys. Acta 243 (1995) 287–290.

[124] J. K. Armstrong, R. B. Wenby, H. J. Meiselman, T. C. Fisher. The hydrodynamic radii of macromolecules and their effect on red blood cell aggregation. Biophys. J. 87 (2004) 4259–4270.

[125] J. A. Glasel. Validity of nucleic acid purities monitored by A260/A280 absorbance ratios. BioTechniques 18 (1995) 62–63.

[126] W. W. Wilfinger, K. Mackey, P. Chomczynski. Effect of pH and ionic strength on the spectrophotometric assessment of nucleic acid purity. BioTechniques 22 (1997) 474–481.

[127] L. Hagel, M. Ostberg, T. Andersson. Apparent pore size distributions of chromatography media. J. Chromatogr. A 743 (1996) 33–42.

[128] W. Q. Huang, L. Yu. A quasi physical method for the equal sphere packing problem. Proceedings of the 11th International Joint Conference of IEEE TrustCom/IEEE ICESS-11/FCST-11 430074 (2011) 1684–1690.